Accepted, Earth & Planetary Science Letters, Dec. 2023

Numerous Tibetan lower-crustal and upper-mantle earthquakes, detected by *Sn/Lg* ratios, suggest crustal delamination or drip tectonics

Xiaohan Song, Simon L. Klemperer

Department of Geophysics, Stanford University, Stanford, CA 94305, USA

Highlights:

- Our single-station *Sn/Lg* method distinguishes above-Moho from below-Moho earthquakes
- In 20 years, two areas in Tibet/Himalaya have >100 m_b ≥3.2 below-Moho earthquakes
- These two areas likely also have >100 m_b ≥3.2 earthquakes between 30 km and the Moho
- Both the above- and below-Moho earthquakes could all be in crustal rocks (eclogite)
- We infer drip tectonics beneath the Himalaya, & delamination tectonics below NW Tibet

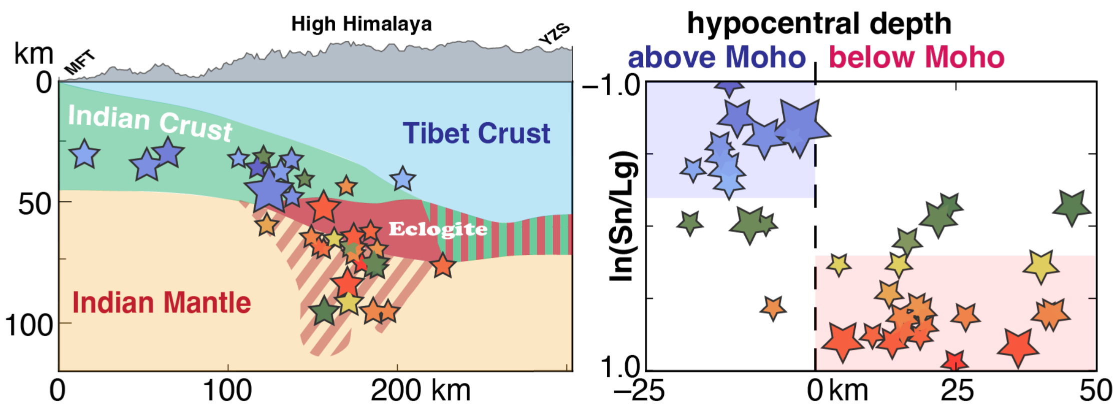

Numerous Tibetan lower-crustal and upper-mantle earthquakes, detected by *Sn/Lg* ratios, suggest crustal delamination or drip tectonics

Xiaohan Song, Simon L. Klemperer

Department of Geophysics, Stanford University, Stanford, CA 94305, USA

A B S T R A C T

Whether intermediate-depth earthquakes beneath Tibet and the Himalaya are in the lower crust or upper mantle should provide insight into rheology, hence composition and temperature, of continental lower crust and upper mantle. Based on the waveguide theory that earthquakes respectively above or below the Moho will excite higher *Lg* or *Sn* energy, we develop an *Sn/Lg* amplitude-ratio analysis using a single permanent station to investigate earthquake depths with respect to the Moho. First, we use synthetics to show the ubiquitous sharp increase of the *Sn/Lg* ratio for hypocenters beneath the crust. A deep-crustal high-v_s layer appropriate for eclogitized Indian lower crust causes a more gradual increase of *Sn/Lg* ratios for hypocenters within or below the eclogite layer. We measured *Sn/Lg* ratios of 595 Tibetan earthquakes from 1998 to 2022 with nominal (catalog) hypocentral depths >30 km and magnitudes >3.2 in five regions (west Tibet, southwest Tibet, south Tibet, southeast Tibet, and Qiangtang). As predicted by our normal-mode synthetics, earthquakes in west and south Tibet show *Sn/Lg* ratios that increase sharply as catalog depths approach the independently determined receiver-function Moho. Numerous earthquakes with high *Sn/Lg* ratios and nominal depths around the reported Moho are identified between the Karakoram fault and Altyn-Tagh fault (ATF) in west Tibet, which we attribute to an eclogitized Indian lower crust extending north to the ATF. Impingement of this underthrust Indian slab against the Tarim craton and consequent eclogite delamination or dripping may cause the observed below-Moho seismicity which occupies a region 100 km across and 200 km along orogenic strike and extends 30–50 km below published Moho depths. Similarly dense seismicity spans the Moho and occupies a similar volume below the Moho beneath the High Himalaya in south Tibet. The south Tibet *Sn/Lg* patterns may indicate an eclogitized Indian layer beginning to delaminate or drip south of the Yarlung-Zangpo suture. Our southeast Tibet and southwest Tibet *Sn/Lg* observations are less clear cut, perhaps due to less appropriate epicentral distances from the available observing stations. The Qiangtang region of Tibet likely has sparse mid-to-lower-crustal earthquakes, but no definitive below-Moho earthquakes. Our work expands the catalog of continental intraplate earthquakes below the Moho by >100 events with m_b>3.2, as well as identifying tens of m_b>3.2 lower-crustal events, so that Tibet fits neither an ideal crême-brulée nor an ideal jelly-sandwich crustal-strength paradigm. Two clusters of earthquakes that each span the Moho may be best explained by the delamination or dripping of a strong eclogitized lower crust into the upper mantle.

---

1. Introduction

The Tibetan plateau is the surface manifestation of the convergence between the Indian plate and the Eurasian plate, and ongoing complex deep-crustal and subcrustal tectonic processes (Klemperer et al., 2022; Tapponnier et al., 2001) may hold the key to Tibet's elevation and evolution. A path to understanding these lower-lithosphere processes is opened up by numerous intermediate-depth earthquakes (Chen and Molnar, 1983; Chen and Yang, 2004; Liang et al., 2008; Monsalve et al., 2006; Zhu and Helmberger, 1996), as shown in Fig. 1, whose hypocentral location (whether mantle or lower crust) is still under debate. The widely used "jelly-sandwich" continental-lithosphere rheology (Bürgmann and Dresen, 2008) with a weak lower crust and a brittle upper mantle was first envisioned in the belief that these intermediate-depth earthquakes occurred within the mantle lithosphere (Chen and Molnar, 1983; Chen and Yang, 2004); such a model is supported by the observation of south Tibet earthquakes as being in the upper crust and in the upper mantle (Liang et al., 2008; Monsalve et al., 2006). The opposed “crème brûlée” model (Bürgmann and Dresen, 2008) in which the lower crust is stronger than the upper mantle gains support from those who believe the Himalayan and Tibetan seismicity maybe exclusively lower-crustal (Jackson, 2002; Maggi et al., 2000). However, more and more Tibetan earthquakes have been discovered to have seismic phases clearly requiring sub-Moho sources (Jiang et al., 2009; Wang and Klemperer, 2021; Zhu and Helmberger, 1996). Different suggestions to explain Tibet’s intermediate-depth earthquakes (here defined as ≥ 60 km) include underthrusting of cold brittle Indian lower crust together with its mantle lithosphere (Craig et al., 2012, 2020; Priestley et al., 2008), flexural stresses (Monsalve et al., 2009), eclogitization (Alvizuri and Hetényi, 2019; Schulte-Pelkum et al., 2019; Shi et al., 2018, 2020), and the extension of crustal faults into the upper mantle (Diehl et al., 2017; Michailos et al., 2021).

The debate on the cause of Tibetan intermediate-depth earthquakes is further complicated by the seismicity beneath Tibet’s south and northwest margins (Fig. 1A), a localization at odds with the believed regional extent of Indian underthrusting, flexural stress, eclogitization, and shallow faulting at specific places (Craig et al., 2012; Shi et al., 2020; Wittlinger et al., 2004b; Zhang et al., 2014). Previous assessments of the causes of Tibet’s near-Moho earthquakes have therefore either been restricted to the small areas in which such earthquakes have been found (Alvizuri and Hetényi, 2019; Monsalve et al., 2006; Schulte-Pelkum et al., 2005) or are ad hoc (e.g., that a locally anhydrous, hence strong Indian crust would explain the absence of intermediate-depth seismicity in central-west Tibet (Craig et al., 2012; Fig 1). These puzzles motivated us to create and interpret a more complete catalog of the intermediate-depth earthquakes across the entirety of Tibet.

Attempts to compare source depth and Moho depth, the simplest method of detecting below-Moho earthquakes, have not clarified this debate, as double errors are introduced by the independent earthquake relocation and Moho determination (Priestley et al., 2008). Significant uncertainties exist in today’s Tibet Moho models (Xia et al., 2023; Zhao et al., 2020), and small earthquakes ($m_b < 4.5$) typically lack the well-recorded “depth phases” (pP, sP, etc.) at teleseismic distances that are often key to precise depth location (Craig et al., 2012). Direct comparison between S-minus-P travel times of P and Ps phases from larger teleseisms that have piercing points very close to locally-recorded small earthquakes and S-minus-P times of these same small earthquakes relies on unusually fortuitous recording geometries and has thus far only documented six below-Moho events, $m_L < 2.9$, in a single area of the central Himalaya (Schulte-Pelkum et al., 2019). Our mew methodology aims to directly determine the layer in which an earthquake nucleates (above or below the Moho) based on waveform characteristics instead of on arrival times. We rely on the principle that earthquakes have their radiated energy mostly trapped by the waveguide in which their hypocenter is located (Fig. 2). The Lg and Sn wavetrains dominantly propagate in the crustal and upper-mantle waveguides respectively (Knopoff et al., 1973; Mousavi et al., 2014; Stephens and Isacks, 1977) so that mantle earthquakes have higher Sn/Lg amplitude ratios than crustal earthquakes (Wang and Klemperer, 2021). Our use of *Sn/Lg* ratios offers a way to distinguish below-Moho from above-Moho earthquakes independent of uncertainty in Moho depth or lithospheric wavespeed.

We use this Sn/Lg method to study 870 earthquakes from 1998 to 2021 across the entirety of Tibet (Fig. 1B). The lack of permanent Tibet stations prevents us from using a multiple-station analysis (Wang and Klemperer, 2021), so we develop a new single-station Sn/Lg method, using the statistics of these 870 earthquakes to overcome inherent uncertainties.

We first establish the theoretical and numerical basis for our Sn/Lg analysis, then describe our data, and apply our single-station method to five separate regions of Tibet: west Tibet (WT), south Tibet (ST), southeast Tibet (SET), southwest Tibet (SWT), and Qiangtang (QT) (Fig. 1B). We present Sn/Lg results and analysis for WT in section 3, and along the Himalaya arc (ST, SET, SWT) in section 4. Analysis of the Sn/Lg results for QT is provided in Supplementary Material. Limitations caused by model heterogeneity, catalog uncertainty, and regional attenuation are discussed in section 5. Finally, we interpret Tibet’s rich near-Moho earthquake catalog as associated with the loss of lower-crustal mafic eclogites from the crust into the mantle.

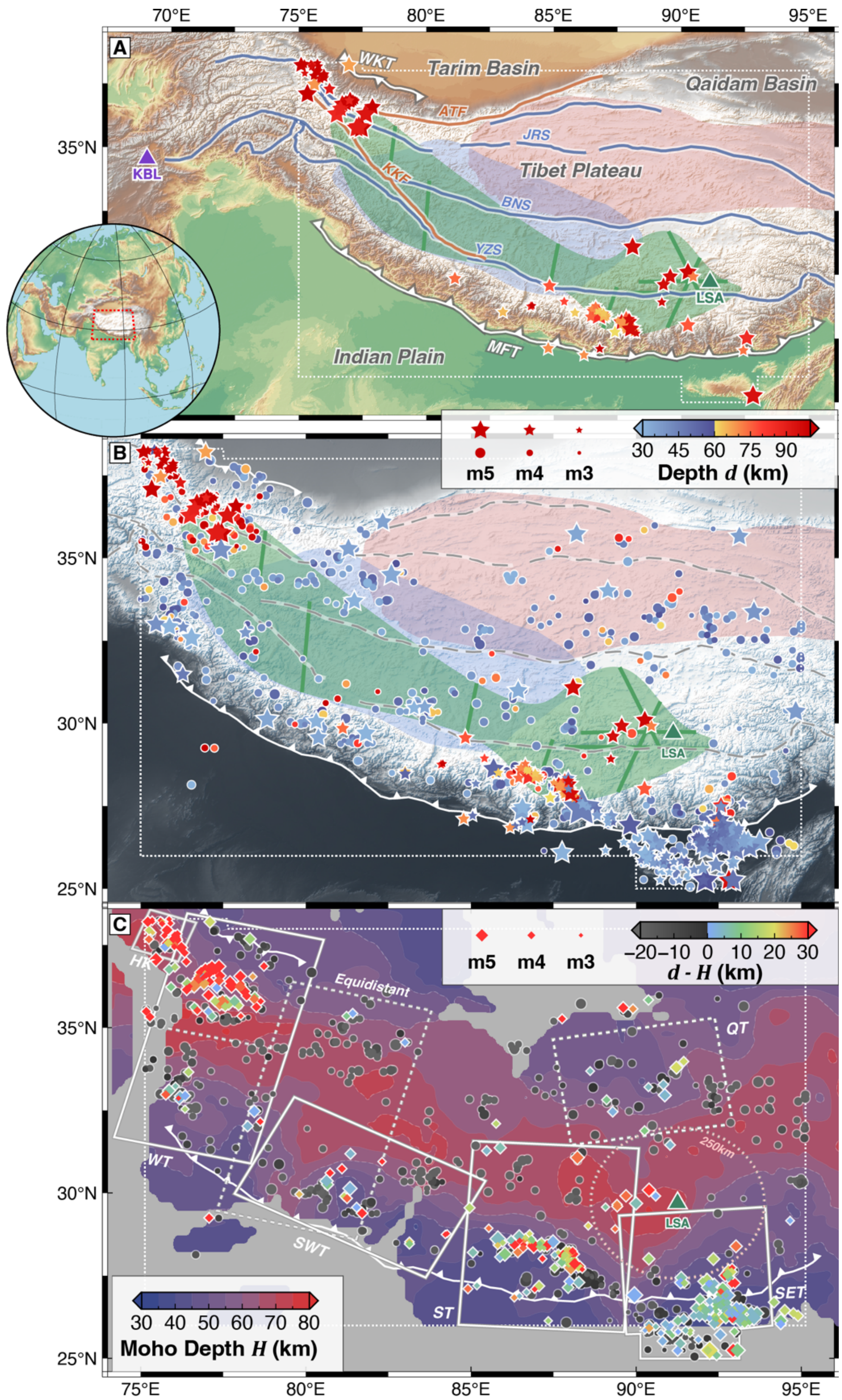

Fig. 1. (**A) Tibet topography and tectonic boundaries.** White dotted box corresponds to red dash box (global map). Stars are earthquakes between 1998–2022 below 60 km located by the Global CMT project, ISC-GEM project, or relocated by specific studies (see section 3.1), colored by hypocentral depth and sized by magnitude. Two triangles are the two permanent stations (IC.LSA and IU.KBL) used in this study. Pink transparent overlay is the high *Sn* attenuation zone in northern Tibet (McNamara et al., 1995). Blue transparent overlay is the Tibet deep aseismic zone (Craig et al., 2012). Green overlay encompasses seismic profiles (solid green lines) along which eclogite has been proposed (Shi et al., 2020; Wittlinger et al., 2004a, 2004b, 2009). Sutures, thrusts,

and faults from Taylor and Yin (2009): MFT: Main Frontal thrust; WKT: West Kunlun thrust; YZS: Yarlung-Zangpo, BNS: Bangong-Nujiang, and JRS: Jinsha River sutures; KKF: Karakoram and ATF: Altyn-Tagh faults. **(B) Tibet earthquakes with catalog depth > 30 km, 1998-2022.** Stars are from same catalog sources as in A; circles are from the USGS-PDE catalog. **(C) Tibet Moho depths from receiver functions (Xia et al., 2023).** Grey regions were not mapped by Xia et al. (2023). Colored diamonds and grey dots are earthquakes from part B with nominal depths below and above the receiver function Moho, respectively (we use an interpolated Moho depth outside the mapped area). White lines bound the regions individually analyzed in this study, solid lines WT and HK West Tibet and Hindu Kush, SWT Southwest Tibet, ST South Tibet and SET Southeast Tibet in the main text, and dashed lines QT Qiangtang and Equidistant from IC.LSA and IU.KBL in Supplementary Materials. Circular dotted pink line marks 250-km radius around IC.LSA, approximate minimum offset for reliable Sn/Lg measurements.

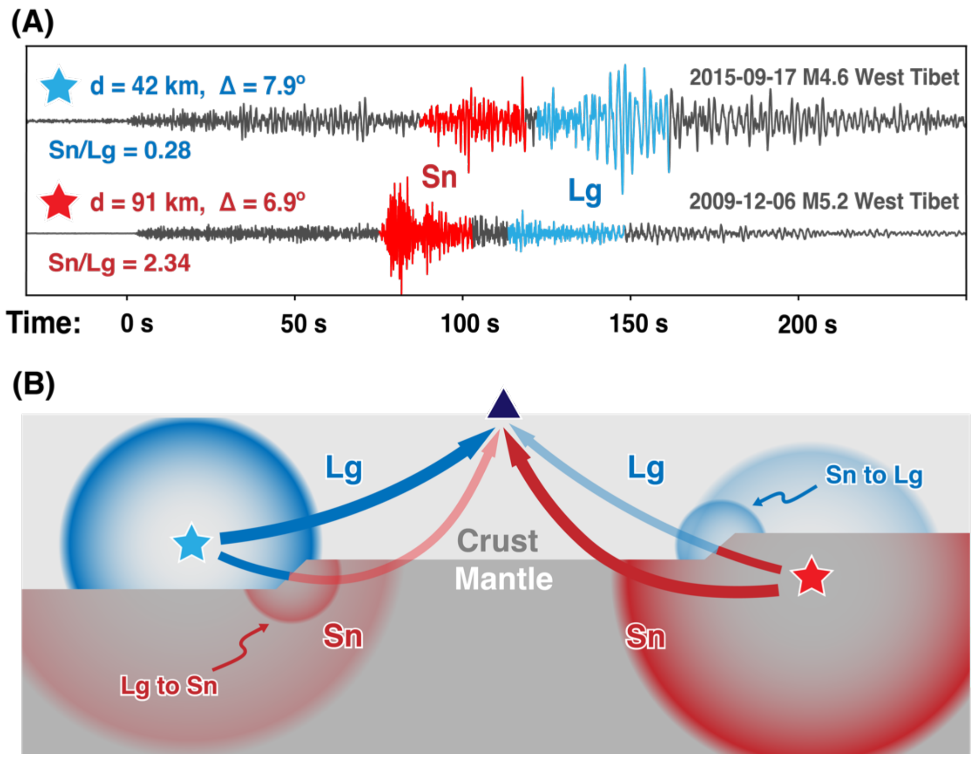

Fig. 2. (A) Examples of Sn and Lg selection (tangential component of two closely spaced west-Tibet earthquakes recorded at Kabul) and (B) schematic mechanisms of Sn and Lg amplitude differentiation. A crustal earthquake (blue star) excites stronger seismic waves in the crust (Lg) and weaker waves in the upper mantle (Sn) (left), and vice versa for an upper-mantle earthquake (red star, right). Some Sn and Lg conversion occurs at Moho ramps: Lg may be blocked travelling from thicker to thinner crust (left) and Sn when travelling from thinner to thicker crust (right) (Kennett, 1986).

2. Theoretical and numerical basis for Sn/Lg ratio analysis

Both the Sn and Lg phases, that are respectively confined largely to upper-mantle and crustal waveguides, can be understood by mode theory (Knopoff et al., 1973; Wang and Klemperer, 2021) or multiply reflected ray theory (Kennett, 1986; Press and Ewing, 1952). In this study, we restrict ourselves to the Love-mode interpretation of the transverse component of seismograms. We follow Wang and Klemperer (2021) in applying Generalized Eigenproblem Spectral Collocation (GESC, Denolle et al., 2012) to calculate and sum Love-wave eigenvectors to get the synthetic waveforms. The vertical variation of the eigenvectors shows that Sn and Lg concentrate their energy in the upper mantle and the crust, respectively, enabling Wang and Klemperer (2021) to establish the theoretical basis for a practical Sn/Lg analysis by synthesizing seismograms for oceanic, cratonic, and Tibetan wavespeed models, and for a variety of focal mechanisms and depths. Attenuation is not included in this modelling.

Here we show synthetics for simplified Tibet models with a thick single-layer crust above an upper-mantle lid and low-velocity zone (Fig. 3A, Zhao et al., 1991). We also calculate synthetics for doublet models with a 15-km-thick high-shear-velocity (“4.x” km/s) base-crustal layer (Fig. 3B) representative of a possible eclogitic layer (Henry et al., 1997). In south Tibet, a lower-crustal doublet or pair of receiver-function converters at the Moho and 10-20 km shallower (Kind et al., 2002) has been widely interpreted as eclogitized mafic Indian lower crust (Fig. 1A). Our doublet models have a $W = 15$ km thick lower-crustal layer (Fig. 3B1&2) with wavespeed and densities appropriate for eclogite (Shi et al., 2020; Wittlinger et al., 2009). The Moho depth (the base of the eclogite layer for the doublet models) is defined as H and varies from 50–70km for our single-Moho models and 62.5–82.5 km for our doublet models. We model a compressional double-couple source at different depths d ranging from 35 km above to 35 km below the Moho (Fig. 3A) or doublet top (Fig. 3B), as recorded at 800 km in the direction 45° from the source’s strike.

We use a Gaussian source time function (standard deviation 2 Hz) and calculate 100 modes of the eigenfunctions before bandpass filtering 0.5-4 Hz. The Sn and Lg windows are defined using a ray-theory approximation, the known earthquake depth, and a uniform crust and mantle with Moho depth (H) of 70 km to mimic the real-world situation where we do not know the Moho depth (Supplementary Material S1). Hence our Sn window can include energy (e.g., trapped in the crustal eclogite layer) that is not Sn as defined as travelling in the mantle. We measured amplitudes of the Sn and Lg phases as the root mean square of the signal within their time windows (Mousavi et al., 2014). Full discussion of our window selection and its robustness to potential uncertainties is in Supplementary Material S1.

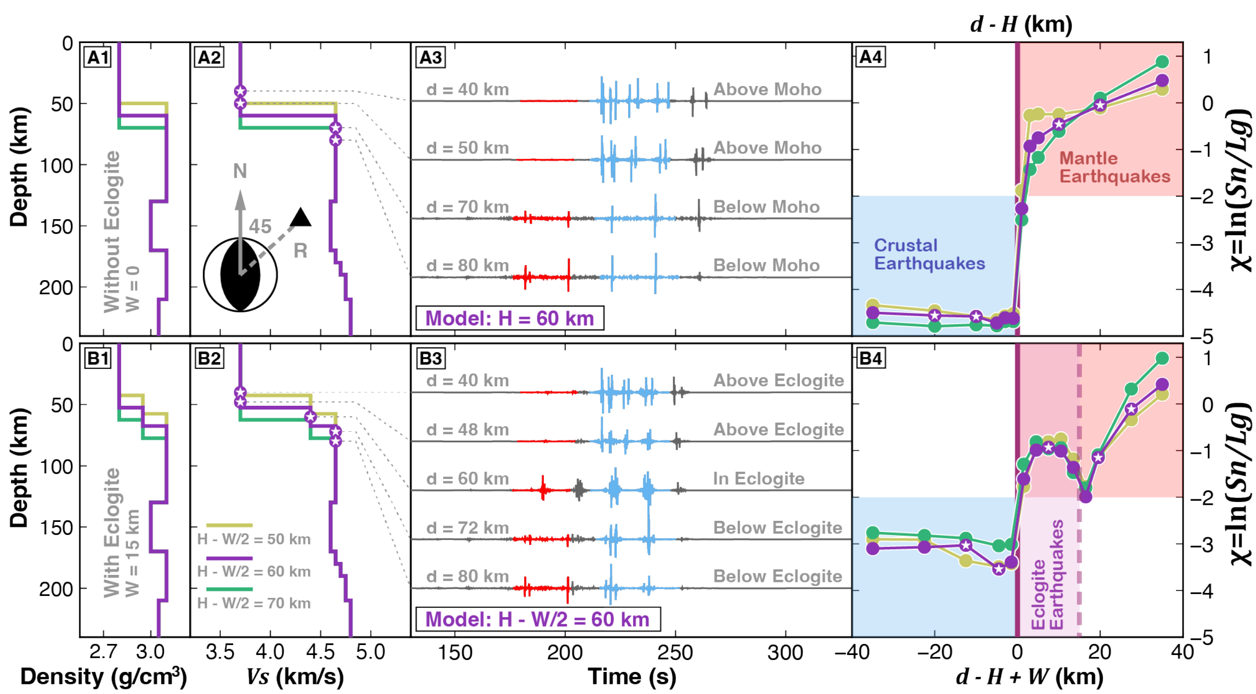

Fig. 3. Source and model parameters and resulting synthetics. (A1-2) Densities and s-wave velocities of the sharp-Moho models after Earth-flattening transform (Supplementary Material S2). Yellow, purple, and green lines represent Moho depths of $H = 50$ km, 60 km, and 70 km, respectively. The focal mechanism and the triangle in (A2) represent the source and receiver; synthetics are for $R = 800\ km$. Purple dots with stars mark the depths of the sources whose seismograms for the purple model are shown in (A3). **(A3) Synthetic waveforms for earthquakes at different depths in the model with a 60 km Moho depth.** Red and blue trace segments are the Sn and Lg windows, calculated as in Supplementary Material S1. **(A4) $\ln(Sn/Lg)$ vs $(d - H)$** (source depth minus Moho depth) for sources from 35 km above to 35 km below the Moho in the sharp-Moho models. **(B1-4) as (A1-4)** but for models with 15-km eclogitized lower crust.

For the simple Moho models, increasing source depth leads to a step increase of Sn/Lg ratio at the Moho depth H, followed by a gradual increase at larger depths (Fig. 3A). For the doublet models, a similar sharp increase of Sn/Lg ratio at the top of the eclogite layer is followed by a decrease at the bottom of the layer and then a rebound. The high Sn/Lg ratios in the eclogite layer can be explained by the ray-theoretical effect of the mirror source formed by the reflective base of eclogite, that vanishes for sources below the eclogite layer. For all our models (which are noise-free and do not include attenuation), we can make a binary classification with earthquakes below the Moho or within the doublet having $\chi = \ln(Sn/Lg) > -2$ and the crustal earthquakes above the doublet having $\chi \leq -2$ (respectively pink and blue regions in Fig. 3 A4, B4).

Previous studies have shown the relative lack of dependence of Sn/Lg on focal mechanism and receiver azimuth or distance (Wang and Klemperer, 2021). Our GESC synthetics do not model noise, geometric spreading, attenuation or scattering and in consequence synthetic Sn/Lg ratios are systematically smaller than observed in real data (see sections 3 and 4). This systematic difference does not impede our single-station Sn/Lg analysis, as a threshold χ ($= \ln(Sn/Lg)$) should also exist in the observations albeit larger than the threshold $\chi = -2$ seen in the synthetics.

3. Data processing

3.1 Data selection

We selected all earthquakes from $26°-38°$N and $75°-95°$E and depth range 30–150 km (20–150 km for southeast Tibet and northeast India) from 1998 to 2021 with $m \geq 3.5$ in the USGS-PDE catalogue (PDE, 2022), and $m \geq 3.2$ in the ISC-GEM (Global Instrumental Earthquake, Bondár et al., 2015) and Global CMT (Centroid-Moment-Tensor, Dziewonski et al., 1981) catalogues and in previous relocation studies (Alvizuri and Hetényi, 2019; Baur, 2007; Bloch et al., 2021; Craig et al., 2012; Diehl et al., 2017; Michailos et al., 2021; Monsalve et al., 2006; Parija et al., 2018). Earthquakes from sources other than the USGS-PDE are classified as "better-located" events in this study and are plotted as stars (Fig. 1A and B) in contrast to events only in the PDE catalog shown as circles (Fig. 1B). Our initial catalog contains 963 earthquakes across the Himalaya and Tibet (Fig. 1B; Supplementary Material S3).

For each earthquake we know the catalog depth d, and we estimate Moho depth H beneath its epicenter from a recent compilation of receiver-function (RF) Moho depths (Xia et al., 2023). We plot $(d - H)$ for every earthquake (Fig. 1C), highlighting those earthquakes nominally below local Moho. A first-order observation is that although earthquakes with catalog depths > 30 km are scattered across the entire Tibet Plateau, most that are nominally below-Moho lie broadly parallel to the Himalaya arc, largely between the Main Frontal thrust and the Yarlung-Zangpo suture, but continuing north to the Altyn-Tagh fault in northwest Tibet, and continuing south of the Main Frontal thrust in northeastern India. Because our methodology relies on comparing Sn/Lg ratios between earthquakes in similar locations, we group the data into smaller regions (white frames in Fig. 1B and C) that capture almost all these near-Moho earthquakes: west Tibet (WT), southwest Tibet (SWT), south Tibet (ST), southeast Tibet (SET), Qiangtang (QT), and Equidistant (between IU.KBL and IC.LSA). We study the earthquakes within these smaller regions, excluding those within 250 km of IC.LSA (dotted circle in Fig. 1C, the minimum distance beyond which Sn and Lg phases become well developed (Mousavi et al., 2014) and clearly differentiated in time (Fig. S1-2), using records from Lhasa (IC.LSA, 1998–present) or Kabul (IU.KBL, 2007–present).

3.2 The practical single-station method

We calculate $Sn\ and\ Lg$ windows as described for the synthetics (section 2.1), but with a fixed Moho depth H = 70 km as a crude average depth between source and receiver. We apply a 0.5–4 Hz bandpass for the Lg window and a 1–4 Hz bandpass for the Sn window and calculate the signal-to-noise ratios (SNR) of both phases (Supplementary Material S4). We discard earthquakes for which both SNR_{Lg} and $SNR_{Sn} < 3$, and for the remaining 595 events we calculate Sn/Lg ratios and uncertainties, using the measured SNR (Supplementary Material S4). Finally, we approximately correct the Sn/Lg ratios for geometric spreading effects (Fan and Lay, 2003; Wang and Klemperer, 2021; Yang et al., 2007) (Supplementary Material S5).

We focus on the records from Kabul in WT and SWT and the records from Lhasa in ST, SET and QT. Records from Kabul and from Lhasa are available in SWT and the Equidistant region. We next plot Sn/Lg amplitude ratios vs $(d - H)$ for each region. Based on our synthetics (Section 2.1), Sn/Lg is dominantly controlled by hypocentral distance above or below the Moho, so using $(d - H)$ instead of d largely removes the effect of Moho topography. Based on our entire dataset we choose a single threshold of $\chi = \ln(Sn/Lg) = 0$ to separate below-Moho from above-Moho earthquakes. In Supplementary Material S6 we show that a step change in χ at or close to $\chi = 0$ is a better fit to the data distribution than a continuous gradation in χ for WT, ST and likely also for SET. We project these earthquakes, with their Sn/Lg ratios, onto regional cross-strike lithospheric profiles to help understand the tectonic setting.

4. Sn/Lg results for Tibet earthquakes

4.1 West Tibet (WT)

Chen and Yang (2004) claimed that four earthquakes beneath the Jinsha-River suture in northwest Tibet originated in the mantle; but additional teleseismic analyses of these and six other events could not distinguish whether their hypocenters, at ~80–100 km depth, were above or below the Moho (Craig et al., 2012; Priestley et al., 2008). In this complex area, we follow previous work (Craig et al., 2012; Priestley et al., 2008) in separating the intermediate-depth earthquakes caused by the Hindu Kush subduction (Fig. 4, box HK) from the intermediate-depth earthquakes of interest in this paper that are associated with India-Asia convergence. Huang et al. (2011) showed with local recordings that at least some of the seismicity nucleated in the lower crust, and Wang and Klemperer (2021) used array Sn/Lg analysis of regional recordings to demonstrate that at least two, and very probably 12, hypocenters were sub-crustal, below-Moho. We measured Sn/Lg for 196 earthquakes in our west Tibet (WT) area from 2007 to 2021 from the IU.KBL station (Fig. 4). Starred earthquakes include better-located events from previous studies (Bloch et al., 2021; Craig et al., 2012; Parija et al., 2018) and ISC-GEM and GCMT catalogs (Bondár et al., 2015; Dziewonski et al., 1981). We describe the WT earthquakes in two subregions, WT1 and WT2 (Fig. 4A), and discuss their significance in section 5.1.

For the WT1 region that has prolific intermediate-depth seismicity (roughly southern Tarim to Bangong-Nujiang suture), there is on average a tripling of Sn/Lg ratio between earthquakes below and above Xia et al.'s (2022) Moho, as predicted by our synthetics. An intermediate zone of $\chi = \ln(Sn/Lg) \in (-0.2,\ 0.2)$ with almost no earthquakes separates the below-Moho from the above-Moho earthquakes (see color bar and red and blue boxes in Fig. 4B). It is this bimodality of reported hypocentral depths and corresponding bimodality of measured χ values that supports a step change in χ across the Moho. For tectonic interpretation we separate the region HK (Fig. 4, dots with diamonds embedded), an area identified as a continuation of the Hindu Kush subduction (Bloch et al., 2021; Priestley et al., 2008), from the main WT zone, even though these HK earthquakes all meet our expected (Sn/Lg) vs $(d - H)$ relation. Excluding these HK earthquakes, we find no definitive mantle seismicity (i.e., with $\chi > 0.2$ and with $d > H$) north of the Altyn-Tagh fault.

Earthquakes in the WT2 region (roughly Bangong-Nujiang suture to Main Frontal Thrust) are mostly located in the crust, with the few that are within uncertainty below the Moho all having 'crustal' Sn/Lg ratios (Fig. 4B2). All three better-located events are in the crust and have low Sn/Lg ratios. A few earthquakes apparently within the crust, that have intermediate or mantle Sn/Lg ratios, are in the region south of the Yarlung-Zangpo suture within the observed Moho doublet interpreted by Zhang et al. (2014) as an eclogitic lower-crustal layer.

Using the Xia et al. (2023) receiver-function Moho, for the whole WT region (including HK), 168 earthquakes (Supplementary Material S7) have Sn/Lg ratios matching their reported depths, and 19 match within error. Just 9 earthquakes have Sn/Lg ratios that fail to match their $(d - H)$ values, but we do not know whether this failure represents a breakdown of our Sn/Lg method, or larger-than-quoted errors in earthquake and Moho depth measurements. Thus, our single-station estimation of whether an earthquake is above or below the Moho appears to be correct for 86% of all 196 events. Given that 12% of events with PDE depths > 60 km have ‘better locations’ that are at < 30 km depth (Fig. S3.2a) we suspect that the major source of error is the PDE hypocentral depths, and that the true failure rate of our Sn/Lg method is only 5% (Tables S7-1, S7-2). We conclude that although any individual earthquake might be mischaracterized, Sn/Lg ratios do statistically separate above- and below-Moho earthquakes with high confidence despite several potentially confounding issues (e.g., noise, variable attenuation and Moho topography between source and receiver (see Supplementary Material S8); unknown focal mechanism; scattering of vertical and radial energy on to the transverse component).

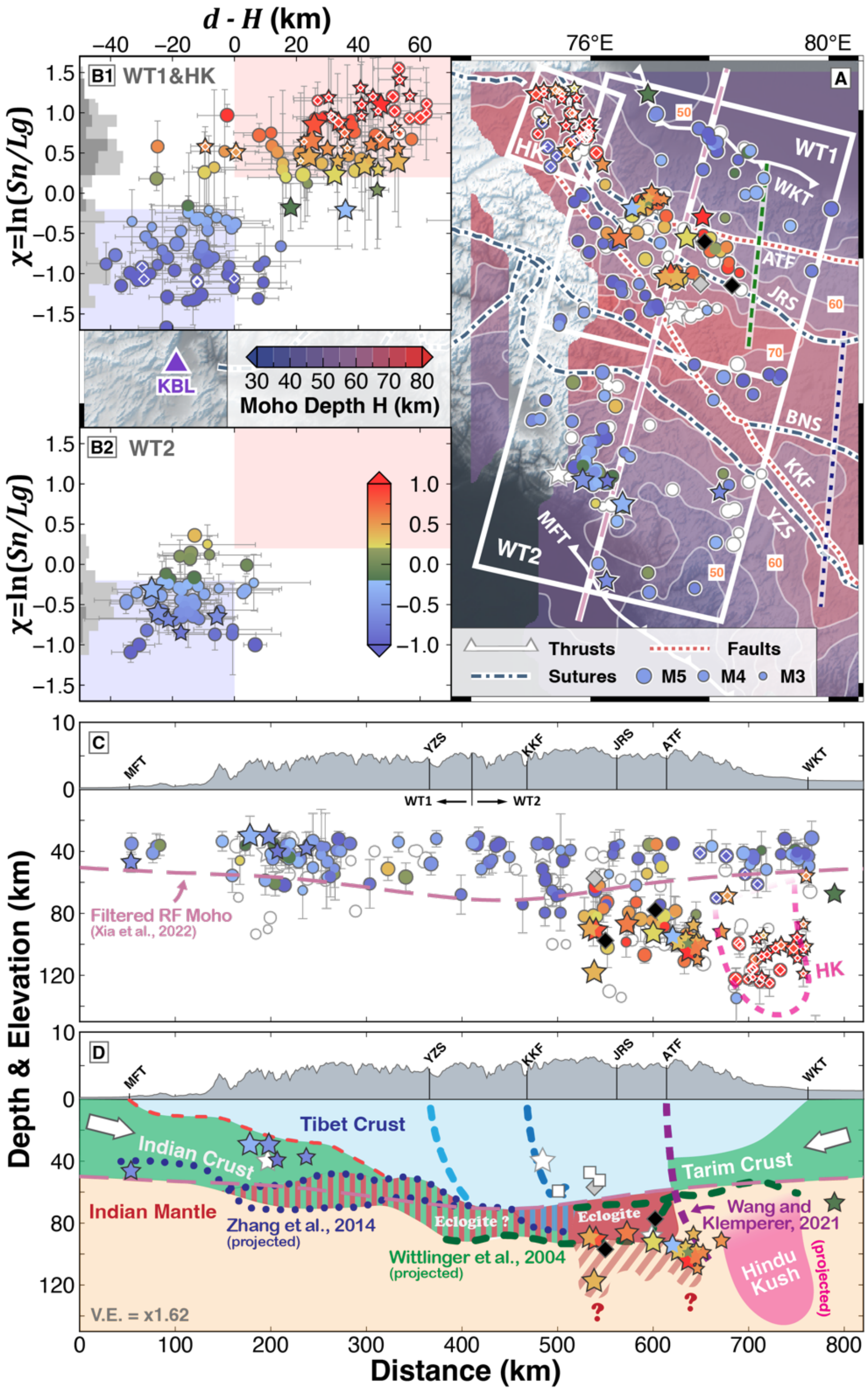

Fig. 4. (A) Sn/Lg amplitude ratios in west Tibet (WT) from recordings at Kabul (IU.KBL). Rectangular white borders show the WT region, separated into subregions WT1, WT2, and area HK (Hindu Kush), superimposed on Moho depth (Xia et al., 2023). Colored dots show the Sn/Lg ratios for each earthquake. Colored stars are events with better defined depths (see section 3.1). Pink dashed line: line of section in (C) and (D). White circles and stars are earthquakes for which Sn/Lg ratios are not available because of low SNR or missing data. White diamonds mark earthquakes in the HK region of well-accepted continental subduction (Kufner et al., 2016). Two black and one grey diamonds mark the earthquakes previously demonstrated to be below-Moho (black) and above-Moho (gray) by Wang and Klemperer (2021). Blue dotted and green dashed lines are Moho interpreted by Zhang et al. (2014) and Wittlinger et al. (2004b). Faults labeled as in Fig. 1A. **(B1-2)** $\mathbf{ln(}Sn/Lg\mathbf{)}$ **vs** $(d-H)$ **plots for the WT1 and WT2 regions.** Color bar is chosen based on natural breaks in the distribution of Sn/Lg values, as shown in grey histogram on left axis. Red, blue, and green segments of the color bar represent Sn/Lg of probable below-Moho earthquakes (pink box), probable above-Moho earthquakes (light blue box), and intermediate values. **(C) Cross-section of Sn/Lg ratios along profile A.** Pink dashed line is the filtered receiver-function Moho (Xia et al., 2023, Supplementary Material S9). **(D) Cartoon tectonic interpretation, showing only 'better-located' events (stars).** Blue dotted and green dashed lines mark the Moho and doublet layers from Zhang et al. (2014) and Wittlinger et al. (2004b) respectively. Boundary between green Indian crust and cyan Tibetan crust (Main Himalayan Thrust, red dashed line) from Gao et al. (2016). Purple dashed line: possible continuation of ATF below the Moho (Wang and Klemperer, 2021). White squares: projected WT lower-crustal earthquakes relocated by Huang et al. (2011).

4.2 Himalaya Arc

We apply the same analysis to our south, southeast, and southwest Tibet (ST, SET, SWT) regions in sequence from the region with the best constraints (ST) to the region with fewest data (SWT).

4.2.1 South Tibet (ST)

The Higher Himalayan and Tethyan Himalayan from ~86–89°E are rich in near-Moho seismicity (e.g., Craig et al., 2012; Diehl et al., 2017; Liang et al., 2008; Michailos et al., 2021; Monsalve et al., 2006). The 1991–1992 Tibet PASSCAL experiment recorded three earthquakes identified from waveform analysis of local/regional recordings (Zhu and Helmberger, 1996) and corroborated using Sn/Lg analysis (Wang and Klemperer, 2021) as having occurred below the Moho. An additional group of six tiny earthquakes have been shown to be below-Moho by their S-minus-P travel time compared to receiver functions recorded at the same temporary station (Schulte-Pelkum et al., 2019), but their magnitudes (<2.9) are below our cut-off of m_b = 3.2. We measure Sn/Lg ratios of 113 earthquakes in our ST region recorded at Lhasa from 1998 to 2022 (Fig. 5).

Recordings at IC.LSA from ST show an increase of Sn/Lg ratios with respect to depth, and a step change near Xia et al.'s (2023) receiver-function Moho (Figs. 5B, S6d), just as for Kabul recordings from WT (Fig. 4). Using identical criteria as for WT we see the same binary distribution with reference to the Moho, correctly categorizing almost all the events with more reliable depths (stars in Fig. 5). Most of the high Sn/Lg earthquakes are in a previously noted near-Moho seismogenic zone (Diehl et al., 2017; Liang et al., 2008; Monsalve et al., 2006), but whereas previous studies could not typically distinguish crustal from mantle earthquakes because of uncertainties in both earthquake depth and Moho depth, our Sn/Lg method shows this seismogenic zone crosses the Moho, nucleating earthquakes both in the crust and in the mantle (Fig. 5 B, C). A few nominally above-Moho earthquakes with large depth uncertainties show low Sn/Lg ratios (top left quadrant, Fig. 5B), and at ~20 km below the Moho several well-located earthquakes show intermediate Sn/Lg ratios (bottom right quadrant, Fig. 5B), possibly corresponding to the lower Sn/Lg ratios observed in our synthetics for earthquakes at or just below the base of an eclogite layer. The most dramatic outlier, event Cr2 (Fig. 5b), is shown with its CMT depth, but while this paper was in review a new re-location (Craig et al., 2023) convincingly placed this event at just 5-km depth, agreeing with our Sn/Lg analysis (see Discussion below).

4.2.2 Southeast Tibet (SET)

In contrast to WT and ST, possible mantle earthquakes in southeast Tibet (SET) are relatively rare north of the trace of the Main Frontal thrust, though we cannot use Sn/Lg ratios to properly examine a number of candidate ≥30-km deep earthquakes within ~250 km of Lhasa. Since the receiver-function Moho compilation of

Xia et al. (2023) does not include studies in NE India, south of 26.5°N we use data from Mitra et al. (2018), Fig. 6A). We measure Sn/Lg ratios at Lhasa for 172 earthquakes from SET, of which 79 are “well-located”, mostly from the GANSSER catalog (Diehl et al., 2017). India south of the Main Frontal Thrust has crust only ~40 km thick, so here our catalog includes all earthquakes with nominal depths >20 km.

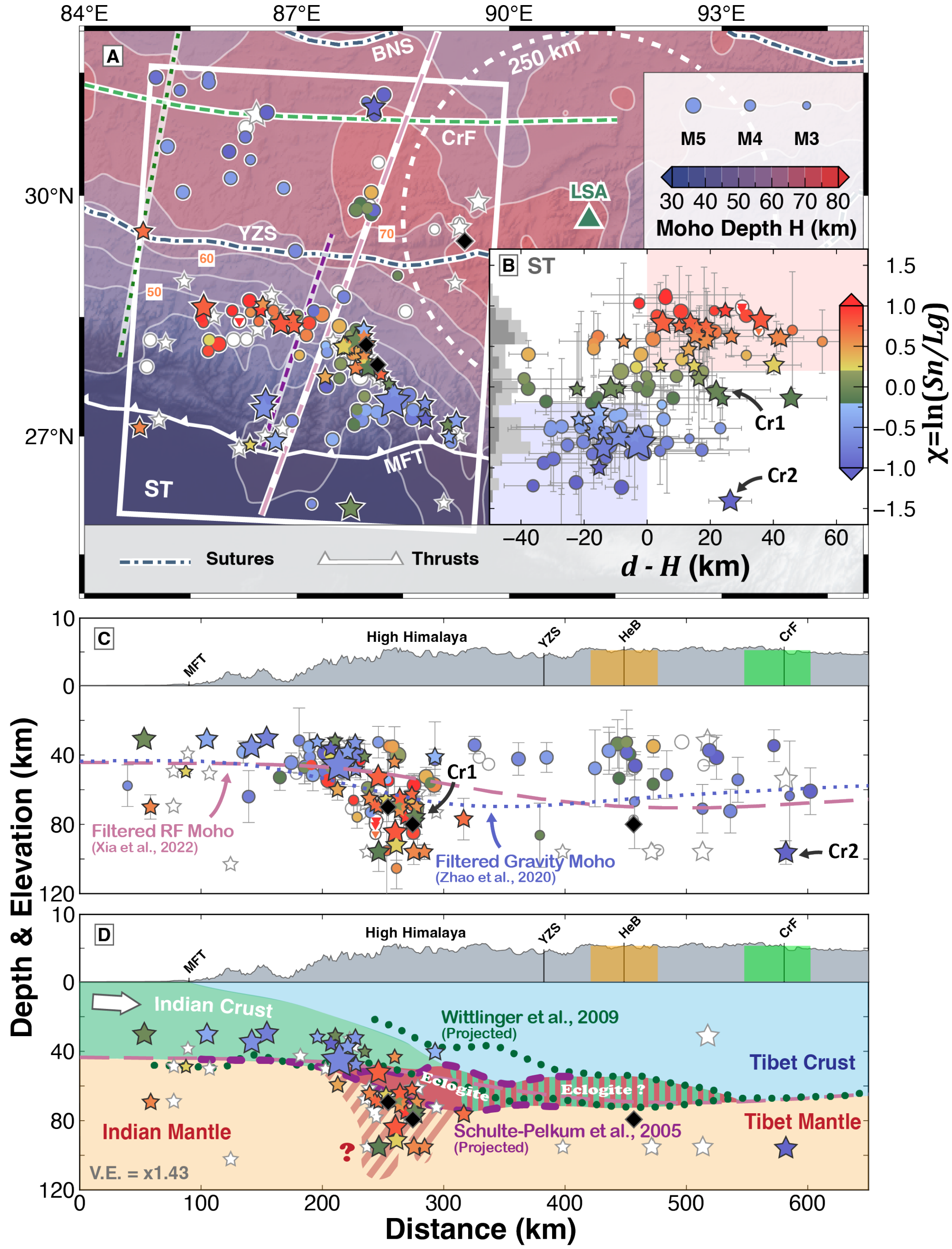

Fig. 5. (A) Spatial distribution of Sn/Lg ratios in south Tibet (ST) measured from recordings at IC.LSA (green triangle). Legend as in Fig. 4. White dots with colored triangles embedded are the earthquakes from the USGS-PDE catalog without depth uncertainties (likely poor located). Black diamonds mark three earthquakes previously demonstrated to be in the mantle (Wang and Klemperer, 2021; Zhu and Helmberger, 1996). White earthquake symbols are <250 km from Lhasa (shown by the white dot-dashed circle), too close for reliable Sn/Lg measurements; or as in Fig. 4 represent low SNR events or missing data. Dashed green line is the Indian crustal front (CrF, Nábělek et al., 2009). **(B) $\ln(Sn/Lg)$ vs $d - H$ plots for the ST region.** Cr1 and Cr2 are earthquakes

studied by Craig et al. (2023). **(C) Cross-section of Sn/Lg ratios along the profile in (A).** Dotted line: gravity Moho (Zhao et al., 2020). HeB denotes the ^{3}He/^{4}He boundary and possible mantle suture (Klemperer et al., 2022). CrF and HeB are oblique to the cross-section so are shown as broad regions. **(D) Cartoon tectonic interpretation, showing only 'better-located' events (stars).** Dotted green lines and dashed purple lines mark the Moho and receiver-function doublets (Schulte-Pelkum et al., 2005; Wittlinger et al., 2009).

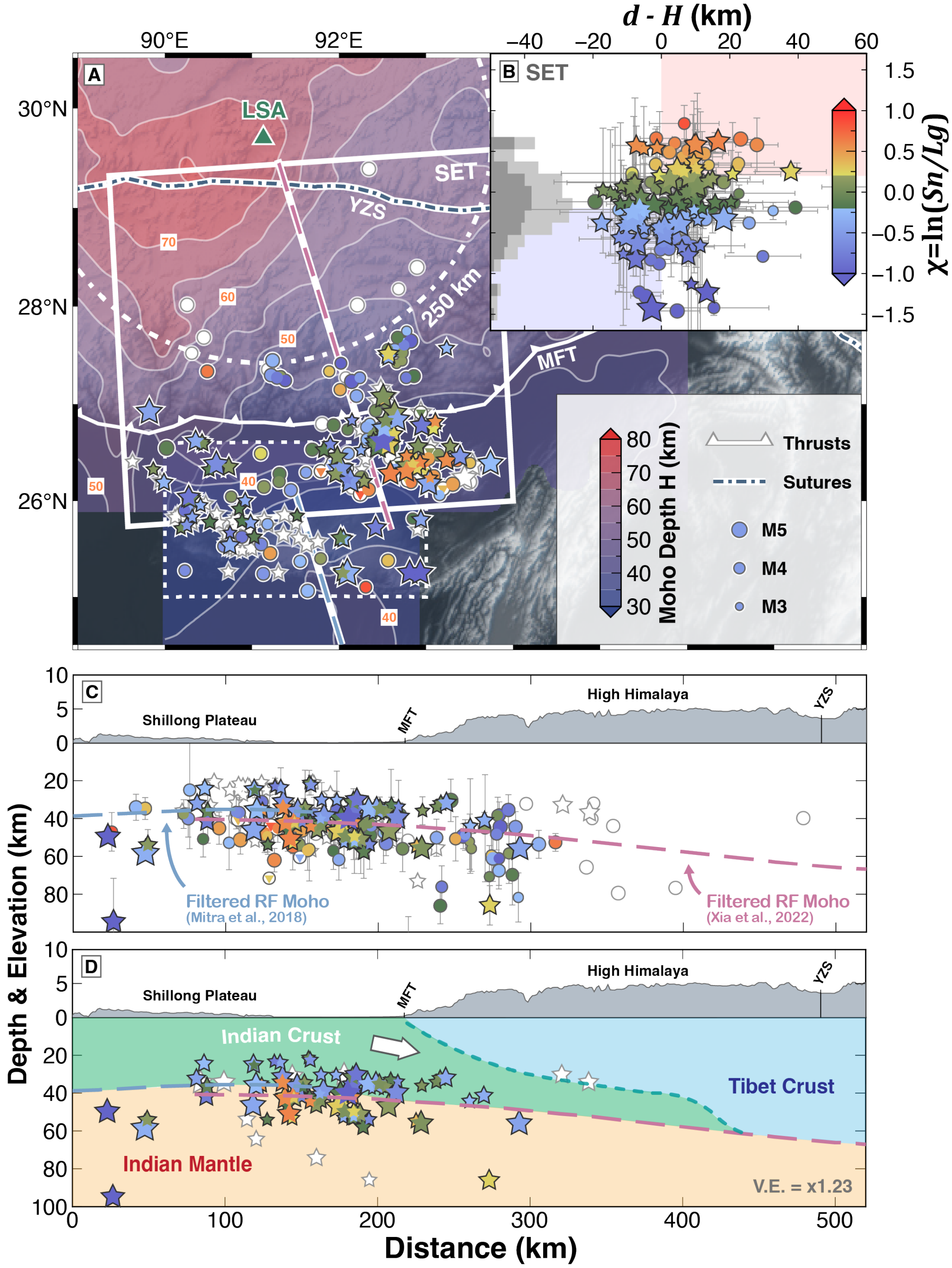

Fig. 6. (A) Spatial distribution of Sn/Lg ratios in southeast Tibet (SET). Dashed box uses receiver-function Moho of Mitra et al. (2018). **(B) $\ln(Sn/Lg)$ vs $d-H$ plots for the SET region.** Legends as in Fig. 5B. **(C) Cross-sectional view of the Sn/Lg**

ratios along the offset profiles in (A). Blue dashed line is the filtered receiver-function Moho from Mitra et al. (2018). Legends as in Fig. 4 and 5. **(D) Cartoon tectonic interpretation, showing only 'better-located' events (stars).** Boundary between green Indian crust and cyan Tibetan crust (Main Himalayan Thrust, mint dashed line) from Grujic et al. (2011).

SE Tibet shows a gradation of Sn/Lg ratios from values that in west Tibet and south Tibet are clearly separate above-Moho from below-Moho hypocenters. In SET there is a maximum in the number of earthquakes very close to Moho depths (Fig. 6B), as opposed to the minima observed in the equivalent histograms for WT and ST (Figs. 4B, 5B). Although the receiver-function Moho map in SE Tibet may have larger errors than elsewhere in Tibet, uncertainties in $d - H$ cannot explain the gradational Sn/Lg values nor the unusual spatial location of the near-Moho seismicity. However, unlike the cases in WT and ST, essentially all the near-Moho seismicity in SET is shallower than the 70 km Moho beneath the recording station Lhasa, leading to Sn blockage that will vary with the source depth to potentially smear out measured Sn/Lg ratios into a continuum (Fig. 2B). The "well-located" earthquakes from 50-90 km below the Shillong Plateau with unexpectedly low Sn/Lg may be good examples of Sn/Lg being reduced by the north-dipping Moho ramp beneath the High Himalaya.

It should be noted that northeast India has long been recognized as an area with potentially problematic focal depths spanning near-surface to upper-mantle (Uma Devi et al., 2009) due in part to large lateral variation in wavespeed from the Himalaya to the Bengal Basin. Some earthquakes re-located by multiple authors using different methodologies (using manual P and S picks on temporary arrays (Diehl et al., 2017), or by using P and sPn phases (Rajkumar et al., 2022)) continue to be reported with depths spanning the Moho and differing by 15–50 km, perhaps due to unclear arrivals or to different 1D wavespeed models. Pending analysis from more than our single station (IC.LSA), our SET data are less reliable than our results from West Tibet and South Tibet.

4.2.3 Southwest Tibet

Our southwest Tibet region has much less intermediate-depth seismicity than further west (WT) or east (ST) and extends north into a region of "no deep seismicity" (Craig et al. 2012; blue region in Fig. 1B and C). Our SWT is approximately equidistant from Lhasa and Kabul, allowing us to compare recordings from the two stations.

We obtained the Sn/Lg ratios of 47 earthquakes from 2000 to 2019 for IC.LSA and 30 earthquakes from 2007–2022 for IU.KBL (Fig. 7), of which 19 were recorded at both stations (Supplementary Materials S10). Because of the long distance to both stations (~700–1300 km, Fig. S10-1), the Sn/Lg ratios tend to have much larger uncertainties than results for WT and ST. We cannot observe any explicit binary classification in either of the Sn/Lg vs $d - H$ plots (Figs. 7A2, 7B2), as most of the recorded earthquakes locate in the crust. Our LSA and KBL analyses both successfully classify most of the crustal earthquakes as low Sn/Lg (< 1) using the same criteria developed in WT and ST. The few earthquakes with low Sn/Lg and depths well below the Moho have large depth uncertainty. IU.KBL recorded no earthquakes with high Sn/Lg. IC.LSA recorded a few earthquakes with high Sn/Lg ratios but only one well-located event (W1) is also well-recorded at IU.KBL and there has much lower Sn/Lg. We suggest that differences in crustal attenuation between raypaths from the SWT region to IU.KBL (largely across Indian craton) and to IC.LSA (entirely across Himalaya and Tibet) likely cause the very different Sn/Lg measured at the two stations for W1 (Fig. S10). With <50 earthquakes in SWT (less than half the number in WT, ST, or SET), we cannot tell whether WT1 and the nearby cluster of earthquakes (at cross-section distance 80–200 km, Fig. 7A3) cross from the lower crust into the upper mantle, but it is intriguing that the dimensions of this cluster, and its location beneath the highest Himalayan topography, resemble the Moho-crossing cluster in ST (Fig. 5C).

4.2.4 Qiangtang Tibet

We studied 56 earthquakes with nominal catalog depths from 30-80 km, but conclude from their Sn/Lg ratios that none of these earthquakes originated in the mantle (Supplementary Material S11).

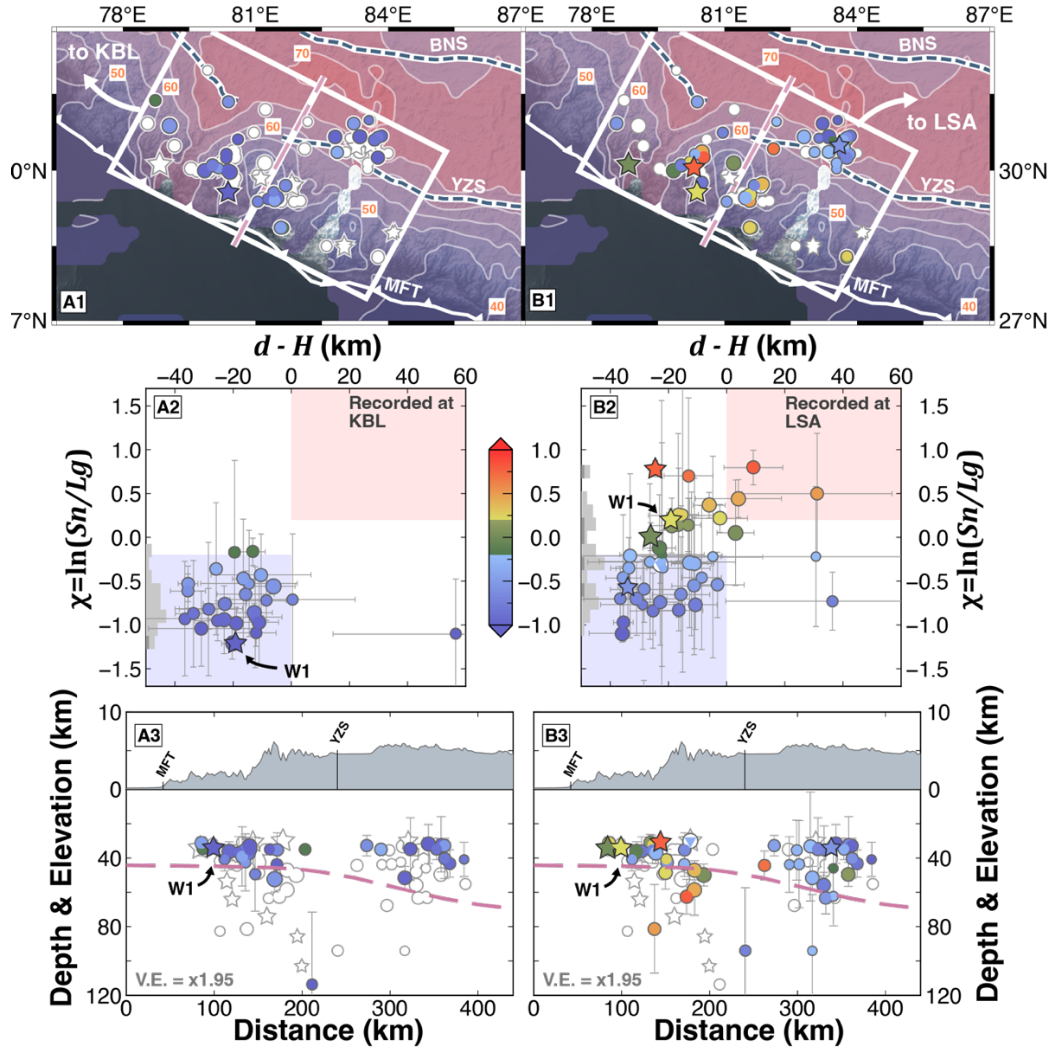

Fig. 7. (A1) Spatial distribution of Sn/Lg ratios in southwest Tibet as recorded at IU.KBL. (A2) $\ln(Sn/Lg)$ vs $d - H$ for SWT recorded at IU.KBL. (A3) Cross-section of Sn/Lg ratios along the profile in (A1). W1 is the only well-located earthquake recorded at both Kabul and Lhasa. **(B1-3) Sn/Lg ratios recorded at IC.LSA.** Legends as in Fig. 4, 5, and 6.

5. Discussion and Tectonic Implications

Our observations show that our single-station Sn/Lg method is able to statistically characterize earthquakes down to magnitude 3.2 as nucleating above or below the Moho. In west Tibet we find pronounced breaks in the distribution of Sn/Lg ratios that lets us confidently identify 50 earthquakes (and likely 72) as nucleating below the Moho, a huge increase over the 12 previously identified (Wang and Klemperer, 2021) (Table S7-2). In south Tibet we show at least 25 earthquakes (likely 40) $m_b \geq 3.2$ nucleated below the Moho, compared to 3 previously known (Wang and Klemperer, 2021). However, our southeast and southwest Tibet observations have less clear Sn/Lg depth separations, likely because SET is too close to the observing station, causing overlap of Sn and Lg windows (Supplementary Material S1) in a region of large lateral wavespeed variability and uncertain Moho depth, and because SWT is too far from IU.KBL and IC.LSA, leading to low SNR.

Our systematic search for intermediate-depth earthquakes across the entire Tibet plateau confirms previous conjecture that there are just two isolated areas where below-Moho earthquakes are common today (Craig et al., 2012; Priestley et al., 2008): beneath the Jinsha-River suture in northwest Tibet (Fig. 4) and beneath the southern Tangra-Yumco and Pumco-Xainza rifts in the southern Tethyan Himalaya (Fig. 5).

It is well-known that global and regional catalogs contain some spurious identifications of intermediate-depth earthquakes. Within Tibet, Langin et al. (2003) used a temporary local array to show that a $m_b = 4.1$ event with a PDE depth of 71 km, immediately south of our Qiangtang study area (too close to IC.LSA for us to analyze, event La1 in Fig. S11a), was in fact at just 5 km depth. Langin et al. concluded that "depths reported for events located solely with teleseismic data are unreliable." Similarly, Craig et al. (2023) discussed four specific Tibetan events, $4.6 \leq m_b \leq 4.8$, with PDE (and CMT) depths of 71 (70) km, 54 (96) km, 37 (18) km, and 33 (46) km, and show that the first (event Cr1 in Fig. 5) was well-located (re-locates to 77 km), but the second (Cr2 in Fig. 5), third and fourth all have correct depths < 5 km. We find an intermediate Sn/Lg value for Cr1, and a definitively crustal Sn/Lg for Cr2 (Fig. 5). The third and fourth events are not included in our study because their better locations with the smallest depth uncertainties are both < 30 km (respectively GCMT and ISC). Note that Cr2 is scored as a failure of our method, even though we found the correct result according to Craig et al. (2023). Craig et al. (2023) concluded that "Across the Tibetan Plateau itself [there are] no earthquakes between ~20 and ~60 km." Although we do not question the re-assignment of the specific earthquakes re-located by Langin et al. (2003) and by Craig et al. (2023), we draw very different conclusions from our study of a much larger number of earthquakes.

We argue that, notwithstanding a few very significant errors, catalog depth determinations are statistically reliable, with depth errors probably similar to the average absolute difference of 15 km between PDE depths and better-located depths (Fig. S3-2). We argue that the existence of re-located earthquakes with depths down to 90–100 km (Baur, 2007; Craig et al., 2012; Diehl et al., 2017; Michailos et al., 2021) as well as PDE events at these depths is a strong argument that seismicity is not restricted to "a strong and seismogenic Indian lower crust" (Craig et al., 2023) but that the mantle is also seismogenic beneath northwest and south Tibet. We believe that the agreement between even relatively poor USGS-PDE hypocentral depths and our Sn/Lg characterization implies that at least some of the lower-crustal depth-estimates found in all areas of Tibet are likely also reliable (Fig. S3-2). Hence, $m_b \geq 3.2$ earthquakes likely exist throughout the crust of Tibet, perhaps even including the Qiangtang (Fig. S11), albeit in much smaller numbers than in the shallow crust.

In both regions of abundant below-Moho earthquakes our catalog suggests a rich sequence from ~20 km above the Moho to >30 km below the Moho, dipping north across-strike for ~100 km (Fig. 4, 5C&D). Both zones of Moho-spanning earthquakes are in locations where receiver-function analyses have been used to argue for eclogitized mafic Indian lower crust in a base-crustal layer (Schulte-Pelkum et al., 2005; Wittlinger et al., 2009, 2004b). Because partially eclogitized lower crust has density and wave-speed intermediate between mantle and granulitic lower-crust (Shi et al., 2020; Wittlinger et al., 2009), seismic models may pick either the top or bottom of eclogite layers as the Moho whereas gravity models may pick a Moho location within the layer. Lower-crustal eclogitization in south Tibet is consistent with the difference between Xia et al.'s (2023) receiver-function Moho and Zhao et al.'s (2020) gravity Moho, with the gravity Moho up to 15-km deeper (Fig. 5C) but close to Schulte-Pelkum's (2005) receiver-function Moho (Fig. 5D).

An association between eclogitization processes and intermediate-depth earthquakes has been proposed in Tibet (Austrheim and Boundy, 1994; Jamtveit et al., 2018; Michailos et al., 2021; Shi et al., 2020), but also elsewhere to explain delamination or dripping in Vrancea (Lorinczi and Houseman, 2009) and the Hindu Kush (Sippl et al., 2013). Our cross-sections suggest the seismicity continues > 30 km beneath the receiver-function Moho that is interpreted as the base of a continuous Indian lower-crustal layer, into a depth range widely supposed to represent Indian ultramafic upper-mantle. The dipping zones of seismicity may represent material detaching from the crust and sinking within the mantle, either by delamination (laminar rollback) or dripping (Rayleigh-Taylor instability) (e.g., Beall et al., 2017).

In west Tibet the intermediate-depth seismicity is likely at the northern limit of the underthrust Indian plate (Craig et al., 2012; Wang and Klemperer, 2021), perhaps triggered by impingement of India against the Tarim craton across the Altyn-Tagh Fault (Figs. 4, 8). In this location at the north edge of the Indian plate, delamination of a lower-crustal layer (or triggered dripping in the terminology of Beall et al., 2017) (Fig. 8A) is geometrically plausible and potentially induced by the large Moho step across the Altyn-Tagh fault. In contrast, the intermediate-depth seismicity in south Tibet is concentrated ~200 km south of the proposed mantle suture (Klemperer et al., 2022) and ~300 km south of the Indian crustal front (Nábělek et al., 2009) (Fig. 5). In this location it is hard to imagine lower-crust delamination as a sheet (Fig. 8C) being replaced by Indian or Tibet mantle far south of the likely mantle suture, and beneath a remaining eclogite layer interpreted from the continuous receiver-function doublet (Nábělek et al., 2009; Wittlinger et al., 2009). Instead, dripping seems more plausible (Fig. 8D), given the limited cross-strike extent of below-Moho earthquakes (Fig. 5) as well as limited along-strike Moho disruption inferred from seismic images of west-east variability in the receiver-function doublet (Shi et al., 2020). We speculate that dripping at this latitude is triggered by bending of the Indian crust as it underthrusts beneath the High Himalaya and is further localized at this longitude by the NNE-trending Tangra-Yumco and Pumco-Xainza rifts (Shi et al., 2020). The lower crust here is estimated from gravity modelling to be only ~30% eclogitized on average, with average density less than the upper mantle (Shi et al., 2020). A Rayleigh-Taylor instability requires the lower-crustal density to exceed the upper-mantle density. This density inversion may be achievable by geologically instantaneous self-sustaining eclogitiation and densification (Malvoisin et al., 2020) following fluid influx along earthquake-generated preferential fluid pathways (Jamtveit et al., 2018) or from autologous fluids of dehydration metamorphism (Hetényi et al., 2007).

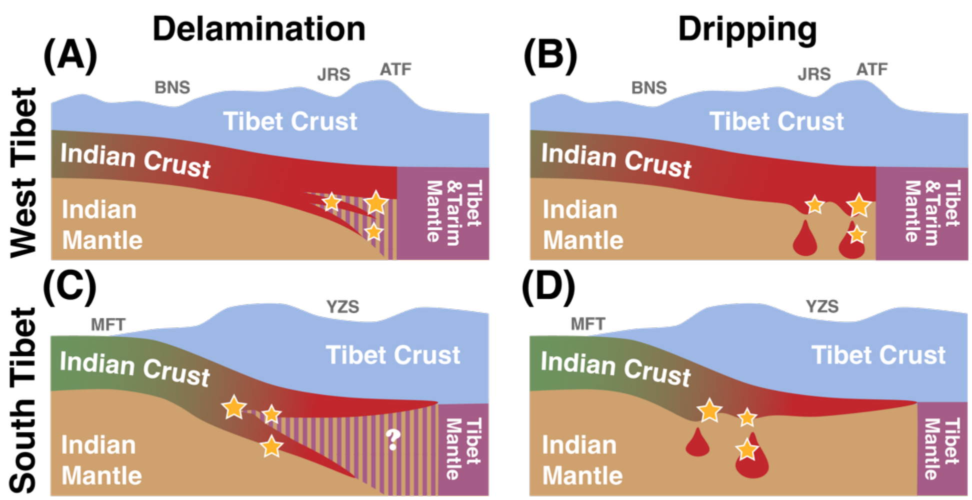

Fig. 8. Cartoons of deep-crustal and below-Moho earthquakes beneath west Tibet (A)(B) and south Tibet (C)(D), drawn to show Indian lower-crustal delamination (sheet-like rollback) (A, C) or dripping (circular in horizontal cross-section) (B, D). Fault abbreviations as in Fig. 1.

These hypotheses of seismogenic dripping and/or delamination raise the question of whether below-Moho earthquakes in WT and ST are occurring in ultramafic mantle or in eclogitic crust now below the Moho. Tibetan near-Moho earthquakes were first thought to have nucleated in a cold, brittle upper-mantle, leading to the “jelly sandwich” model of crustal rheology (Chen and Molnar, 1983), which was further supported by accumulating discoveries of below-Moho earthquakes (Chen and Yang, 2004) and lower-crustal seismicity gaps (Liang et al., 2008). However, reappraisal of these earthquakes' depth uncertainties allowed the hypothesis that they were located in the lower crust (Craig et al., 2012; Jackson, 2002; Priestley et al., 2008), leading to the “crème brûlée” model of a strong lower crust above a weaker upper mantle. The recent demonstration by Sn/Lg methods of below-Moho earthquakes existing in both south and northwest Tibet (Wang and Klemperer, 2021), as well as lower-crustal earthquakes in northwest Tibet (Huang et al., 2011), supported a fully seismogenic lithosphere with earthquakes at all depths. This fully seismogenic behavior may be restricted to the region of below-Moho seismicity beneath the Jinsha-River suture and Altyn-Tagh fault, and to areas underlain by cratonic Indian lower crust (green in Figs. 4D, 5D, 6D). Our areally complete Sn/Lg study across a 20-year time-scale shows that the Tibetan lower crust (cyan in Figs. 4D, 5D, 6D) has almost no ‘better-located’ lower-crustal earthquakes except in the two specific regions of Moho-crossing seismicity. These two regions beneath ST and WT are more seismically active below the Moho than above (Table S7-1) and may correspond to detachment from weak Tibetan middle crust of strong eclogitized Indian lower crust that deforms while sinking into the upper-mantle. Thus the below-Moho earthquakes may only be present in crustal lithologies (Klemperer et al., 2013).

In SE Tibet the geographic pattern of near-Moho earthquakes seems clearly different. These possible below-Moho events south of the Main Frontal Thrust might relate to Himalayan deformation stepping south to the Shillong Plateau, and to complex stresses near the syntaxis where Indian crust subducts both beneath the Himalaya and the Indo-Burman ranges. We defer further discussion of these events pending examination of their Sn/Lg ratios on Indian seismic stations south of the Himalaya.

6. Conclusions

We have demonstrated a single-station Sn/Lg method to detect below-Moho earthquakes beneath the Tibet plateau, based on synthetics of high-frequency waveforms from the summation of Love modes. We recognize a Sn/Lg amplitude-ratio step increase across the Moho that is largely independent of epicentral distance, crustal thickness, and the existence of a receiver–function doublet. Given the previously demonstrated near-independence of Sn/Lg ratios from focal-mechanism type and receiver azimuth (Wang and Klemperer, 2021), we anticipate the possibility of observing separation of low and high Sn/Lg ratios, and hence distinction of crustal and sub-crustal earthquakes, in many parts of the globe.

We apply our Sn/Lg method to 595 earthquakes with catalog depths >30 km in Tibet (>20 km in SET) and find with confidence 165 unique events nucleated above Moho and 101 events nucleated below Moho, even after taking the uncertainties into consideration (Table S7-2, 'definitive' results). Our Sn/Lg results identify concentrated zones of below-Moho earthquakes between the Jinsha-River suture and Altyn-Tagh fault in west Tibet and beneath the transition from the High Himalaya to the Tethyan Himalaya in south Tibet. The cross-sectional geometry of these earthquake clusters supports an eclogitized Indian lower crust currently delaminating or dripping into the upper mantle in response to local collision and/or bending stresses. The likely existence of these earthquakes in mafic eclogites may allow new constraints on temperatures and strain rates beneath Tibet (Molnar, 2020).

Acknowledgements

We thank Shiqi (Axel) Wang for his many helpful suggestions and software assistance. All seismograms were downloaded from IRIS (www.iris.edu).

References

Alvizuri, C., Hetényi, G., 2019. Source mechanism of a lower crust earthquake beneath the Himalayas and its possible relation to metamorphism. Tectonophysics 769, 128153. https://doi.org/10.1016/j.tecto.2019.06.023

Austrheim, H., Boundy, T.M., 1994. Pseudotachylytes generated during seismic faulting and eclogitization of the deep crust. Science 265, 82–83. https://doi.org/10.1126/science.265.5168.82

Baur, J.R., 2007. Seismotectonics of the Himalayas and the Tibetan Plateau : moment tensor analysis of regional seismograms. Oregon State University.

Bloch, W., Schurr, B., Yuan, X., Ratschbacher, L., Reuter, S., Kufner, S.-K., Xu, Q., Zhao, J., 2021. Structure and stress field of the lithosphere between Pamir and Tarim. Geophys. Res. Lett. 48, e2021GL095413. https://doi.org/10.1029/2021GL095413

Bondár, I., Engdahl, E.R., Villaseñor, A., Harris, J., Storchak, D., 2015. ISC-GEM: Global Instrumental Earthquake Catalogue (1900–2009), II. Location and seismicity patterns. Phys. Earth Planet. Inter., ISC-GEM Catalogue 239, 2–13. https://doi.org/10.1016/j.pepi.2014.06.002

Bürgmann, R., Dresen, G., 2008. Rheology of the lower crust and upper mantle: evidence from rock mechanics, geodesy, and field observations. Annu. Rev. Earth Planet. Sci. 36, 531–567. https://doi.org/10.1146/annurev.earth.36.031207.124326

Chen, W.-P., Molnar, P., 1983. Focal depths of intracontinental and intraplate earthquakes and their implications for the thermal and mechanical properties of the lithosphere. J. Geophys. Res. Solid Earth 88, 4183–4214. https://doi.org/10.1029/JB088iB05p04183

Chen, W.-P., Yang, Z., 2004. Earthquakes beneath the Himalayas and Tibet: evidence for strong lithospheric mantle. Science 304, 1949–1952. https://doi.org/10.1126/science.1097324

Craig, T.J., Copley, A., Jackson, J., 2012. Thermal and tectonic consequences of India underthrusting Tibet. Earth Planet. Sci. Lett. 353–354, 231–239. https://doi.org/10.1016/j.epsl.2012.07.010

Craig, T.J., Jackson, J., Priestley, K., Ekström, G., 2023. A cautionary tale: examples of the mis-location of small earthquakes beneath the Tibetan plateau by routine approaches. Geophys. J. Int. 233, 2021–2038. https://doi.org/10.1093/gji/ggad025

Craig, T.J., Kelemen, P.B., Hacker, B.R., Copley, A., 2020. Reconciling geophysical and petrological estimates of the thermal structure of southern Tibet. Geochem. Geophys. Geosystems 21, e2019GC008837. https://doi.org/10.1029/2019GC008837

Denolle, M.A., Dunham, E.M., Beroza, G.C., 2012. Solving the Surface-Wave Eigenproblem with Chebyshev Spectral Collocation. Bull. Seismol. Soc. Am. 102, 1214–1223. https://doi.org/10.1785/0120110183

Diehl, T., Singer, J., Hetényi, G., Grujic, D., Clinton, J., Giardini, D., Kissling, E., 2017. Seismotectonics of Bhutan: Evidence for segmentation of the Eastern Himalayas and link to foreland deformation. Earth Planet. Sci. Lett. 471, 54–64. https://doi.org/10.1016/j.epsl.2017.04.038

Dziewonski, A.M., Chou, T.-A., Woodhouse, J.H., 1981. Determination of earthquake source parameters from waveform data for studies of global and regional seismicity. J. Geophys. Res. Solid Earth 86, 2825–2852. https://doi.org/10.1029/JB086iB04p02825

Fan, G.-W., Lay, T., 2003. Strong Lg wave attenuation in the Northern and Eastern Tibetan Plateau measured by a two-station/two-event stacking method. Geophys. Res. Lett. 30, 1530. https://doi.org/10.1029/2002GL016211

Gao, R., Lu, Z., Klemperer, S.L., Wang, H., Dong, S., Li, W., Li, H., 2016. Crustal-scale duplexing beneath the Yarlung Zangbo suture in the western Himalaya. Nat. Geosci. 9, 555–560. https://doi.org/10.1038/ngeo2730

Grujic, D., Warren, C.J., Wooden, J.L., 2011. Rapid synconvergent exhumation of Miocene-aged lower orogenic crust in the eastern Himalaya. Lithosphere 3, 346–366. https://doi.org/10.1130/L154.1

Henry, P., Le Pichon, X., Goffé, B., 1997. Kinematic, thermal and petrological model of the Himalayas: constraints related to metamorphism within the underthrust indian crust and topographic elevation. Tectonophysics 273, 31–56. https://doi.org/10.1016/S0040-1951(96)00287-9

Hetényi, G., Cattin, R., Brunet, F., Bollinger, L., Vergne, J., Nábělek, J.L., Diament, M., 2007. Density distribution of the India plate beneath the Tibetan plateau: Geophysical and petrological constraints on the kinetics of lower-crustal eclogitization. Earth Planet. Sci. Lett. 264, 226–244. https://doi.org/10.1016/j.epsl.2007.09.036

Huang, G.-C.D., Roecker, S.W., Levin, V., 2011. Lower-crustal earthquakes in the West Kunlun range. Geophys. Res. Lett. 38. https://doi.org/10.1029/2010GL045893

Jackson, J., 2002. Strength of the continental lithosphere: Time to abandon the jelly sandwich? GSA Today 12 (9), 4–9. https://doi.org/10.1130/1052-5173(2002)012<0004:SOTCLT>2.0.CO;2

Jamtveit, B., Ben-Zion, Y., Renard, F., Austrheim, H., 2018. Earthquake-induced transformation of the lower crust. Nature 556, 487–491. https://doi.org/10.1038/s41586-018-0045-y

Jiang M., Zhou S., Tong X., Liang X., Chen Y., 2009. Accurate depth determination of deep earthquake in southern Tibet and its geodynamic implication. Chin. J. Geophys. 52, 2237–2244. https://doi.org/10.3969/j.issn.0001-5733.2009.09.007

Kennett, B.L.N., 1986. Lg waves and structural boundaries. Bull. Seismol. Soc. Am. 76, 1133–1141. https://doi.org/10.1785/BSSA0760041133

Kind, R., Yuan, X., Saul, J., Nelson, D., Sobolev, S.V., Mechie, J., Zhao, W., Kosarev, G., Ni, J., Achauer, U., Jiang, M., 2002. Seismic Images of Crust and Upper Mantle Beneath Tibet: Evidence for Eurasian Plate Subduction. Science 298, 1219–1221. https://doi.org/10.1126/science.1078115

Klemperer, S.L., Kennedy, B.M., Sastry, S.R., Makovsky, Y., Harinarayana, T., Leech, M.L., 2013. Mantle fluids in the Karakoram fault: Helium isotope evidence. Earth Planet. Sci. Lett. 366, 59–70. https://doi.org/10.1016/j.epsl.2013.01.013

Klemperer, S.L., Zhao, P., Whyte, C.J., Darrah, T.H., Crossey, L.J., Karlstrom, K.E., Liu, T., Winn, C., Hilton, D.R., Ding, L., 2022. Limited underthrusting of India below Tibet: 3He/4He analysis of thermal springs locates the mantle suture in continental collision. Proc. Natl. Acad. Sci. 119, e2113877119. https://doi.org/10.1073/pnas.2113877119

Knopoff, L., Schwab, F., Kauselt, E., 1973. Interpretation of Lg. Geophys. J. Int. 33, 389–404. https://doi.org/10.1111/j.1365-246X.1973.tb02375.x

Kufner, S.-K., Schurr, B., Sippl, C., Yuan, X., Ratschbacher, L., Akbar, A. s/of M., Ischuk, A., Murodkulov, S., Schneider, F., Mechie, J., Tilmann, F., 2016. Deep India meets deep Asia: Lithospheric indentation, delamination and break-off under Pamir and Hindu Kush (Central Asia). Earth Planet. Sci. Lett. 435, 171–184. https://doi.org/10.1016/j.epsl.2015.11.046

Langin, W.R., Brown, L.D., Sandvol, E.A., 2003. Seismicity of central Tibet from project INDEPTH III seismic recordings. Bull. Seismol. Soc. Am. 93, 2146–2159. https://doi.org/10.1785/0120030004

Levin, V., Huang, G.D., Roecker, S., 2013. Crust–mantle coupling at the northern edge of the Tibetan plateau: Evidence from focal mechanisms and observations of seismic anisotropy. Tectonophysics 584, 221–229. https://doi.org/10.1016/j.tecto.2012.05.013

Liang, X., Zhou, S., Chen, Y.J., Jin, G., Xiao, L., Liu, P., Fu, Y., Tang, Y., Lou, X., Ning, J., 2008. Earthquake distribution in southern Tibet and its tectonic implications. J. Geophys. Res. Solid Earth 113. https://doi.org/10.1029/2007JB005101

Lorinczi, P., Houseman, G.A., 2009. Lithospheric gravitational instability beneath the Southeast Carpathians. Tectonophysics, TOPO-EUROPE: The Geoscience of coupled Deep Earth-surface processes 474, 322–336. https://doi.org/10.1016/j.tecto.2008.05.024

Maggi, A., Jackson, J.A., McKenzie, D., Priestley, K., 2000. Earthquake focal depths, effective elastic thickness, and the strength of the continental lithosphere. Geology 28, 495–498. https://doi.org/10.1130/0091-7613(2000)28<495:EFDEET>2.0.CO;2

Malvoisin, B., Austrheim, H., Hetényi, G., Reynes, J., Hermann, J., Baumgartner, L.P., Podladchikov, Y.Y., 2020. Sustainable densification of the deep crust. Geology 48, 673–677. https://doi.org/10.1130/G47201.1

McNamara, D.E., Owens, T.J., Walter, W.R., 1995. Observations of regional phase propagation across the Tibetan Plateau. J. Geophys. Res. Solid Earth 100, 22215–22229. https://doi.org/10.1029/95JB01863

Michailos, K., Carpenter, N.S., Hetényi, G., 2021. Spatio-temporal evolution of intermediate-depth seismicity beneath the Himalayas: implications for metamorphism and tectonics. Front. Earth Sci. 9. https://doi.org/10.3389/feart.2021.742700

Mitra, S., Priestley, K.F., Borah, K., Gaur, V.K., 2018. Crustal structure and evolution of the eastern Himalayan plate boundary system, northeast India. J. Geophys. Res. Solid Earth 123, 621–640. https://doi.org/10.1002/2017JB014714

Molnar, P., 2020. The brittle-plastic transition, earthquakes, temperatures, and strain rates. J. Geophys. Res. Solid Earth 125, e2019JB019335. https://doi.org/10.1029/2019JB019335

Monsalve, G., McGovern, P., Sheehan, A., 2009. Mantle fault zones beneath the Himalayan collision: Flexure of the continental lithosphere. Tectonophys. 477, 66–76. https://doi.org/10.1016/j.tecto.2008.12.014

Monsalve, G., Sheehan, A., Schulte-Pelkum, V., Rajaure, S., Pandey, M.R., Wu, F., 2006. Seismicity and one-dimensional velocity structure of the Himalayan collision zone: Earthquakes in the crust and upper mantle. J. Geophys. Res. Solid Earth 111. https://doi.org/10.1029/2005JB004062

Mousavi, S.M., Cramer, C.H., Langston, C.A., 2014. Average QLg, QSn, and observation of Lg blockage in the continental margin of Nova Scotia. J. Geophys. Res. Solid Earth 119, 7722–7744. https://doi.org/10.1002/2014JB011237

Nábělek, J., Hetényi, G., Vergne, J., Sapkota, S., Kafle, B., Jiang, M., Su, H., Chen, J., Huang, B.-S., Team, the H.-C., 2009. Underplating in the Himalaya-Tibet collision zone revealed by the Hi-CLIMB experiment. Science 325, 1371–1374. https://doi.org/10.1126/science.1167719

Parija, M.P., Kumar, S., Tiwari, V.M., Rao, N.P., Kumar, N., Biswal, S., Singh, I., 2018. Microseismicity, tectonics and seismic potential in the Western Himalayan segment, NW Himalaya, India. J. Asian Earth Sci. 159, 1–16. https://doi.org/10.1016/j.jseaes.2018.03.016

PDE, 2022. The Preliminary Determination of Epicenters (PDE) Bulletin [WWW Document]. URL https://earthquake.usgs.gov/data/comcat/catalog/us/ (accessed 8.9.22).

Press, F., Ewing, M., 1952. Two slow surface waves across North America. Bull. Seismol. Soc. Am. 42, 219–228. https://doi.org/10.1785/BSSA0420030219

Priestley, K., Jackson, J., McKenzie, D., 2008. Lithospheric structure and deep earthquakes beneath India, the Himalaya and southern Tibet. Geophys. J. Int. 172, 345–362. https://doi.org/10.1111/j.1365-246X.2007.03636.x

Rajkumar, Prajapati, S.K., Pal, S.K., Srivastava, H.N., 2022. Determination of focal depths of moderate earthquakes in Northeast Indian region using depth phase sPn. Nat. Hazards 114, 427–455. https://doi.org/10.1007/s11069-022-05396-7

Schulte-Pelkum, V., Monsalve, G., Sheehan, A., Pandey, M.R., Sapkota, S., Bilham, R., Wu, F., 2005. Imaging the Indian subcontinent beneath the Himalaya. Nature 435, 1222–1225. https://doi.org/10.1038/nature03678

Schulte-Pelkum, V., Monsalve, G., Sheehan, A.F., Shearer, P., Wu, F., Rajaure, S., 2019. Mantle earthquakes in the Himalayan collision zone. Geology 47, 815–819. https://doi.org/10.1130/G46378.1

Shi, D., Klemperer, S.L., Shi, J., Wu, Z., Zhao, W., 2020. Localized foundering of Indian lower crust in the India–Tibet collision zone. Proc. Natl. Acad. Sci. 117, 24742–24747. https://doi.org/10.1073/pnas.2000015117

Shi, F., Wang, Y., Yu, T., Zhu, L., Zhang, J., Wen, J., Gasc, J., Incel, S., Schubnel, A., Li, Z., Chen, T., Liu, W., Prakapenka, V., Jin, Z., 2018. Lower-crustal earthquakes in southern Tibet are linked to eclogitization of dry metastable granulite. Nat. Commun. 9, 3483. https://doi.org/10.1038/s41467-018-05964-1

Sippl, C., Schurr, B., Tympel, J., Angiboust, S., Mechie, J., Yuan, X., Schneider, F.M., Sobolev, S.V., Ratschbacher, L., Haberland, C., 2013. Deep burial of Asian continental crust beneath the Pamir imaged with local earthquake tomography. Earth Planet. Sci. Lett. 384, 165–177. https://doi.org/10.1016/j.epsl.2013.10.013

Stephens, C., Isacks, B.L., 1977. Toward an understanding of Sn: Normal modes of love waves in an oceanic structure. Bull. Seismol. Soc. Am. 67, 69–78. https://doi.org/10.1785/BSSA0670010069

Tapponnier, P., Zhiqin, X., Roger, F., Meyer, B., Arnaud, N., Wittlinger, G., Jingsui, Y., 2001. Oblique Stepwise Rise and Growth of the Tibet Plateau. Science 294, 1671–1677. https://doi.org/10.1126/science.105978

Taylor, M., Yin, A., 2009. Active structures of the Himalayan-Tibetan orogen and their relationships to earthquake distribution, contemporary strain field, and Cenozoic volcanism. Geosphere 5, 199–214. https://doi.org/10.1130/GES00217.1

Uma Devi, E., Rao, N.P., Ravi Kumar, M., 2009. Modelling of sPn phases for reliable estimation of focal depths in northeastern India. Curr. Sci. 96, 1251–1255.

Wang, S., Klemperer, S.L., 2021. Love-wave normal modes discriminate between upper-mantle and crustal earthquakes: Simulation and demonstration in Tibet. Earth Planet. Sci. Lett. 571, 117089. https://doi.org/10.1016/j.epsl.2021.117089

Wittlinger, G., Farra, V., Hetényi, G., Vergne, J., Nábělek, J., 2009. Seismic velocities in Southern Tibet lower crust: a receiver function approach for eclogite detection. Geophys. J. Int. 177, 1037–1049. https://doi.org/10.1111/j.1365-246X.2008.04084.x

Wittlinger, G., Farra, V., Vergne, J., 2004a. Lithospheric and upper-mantle stratifications beneath Tibet: New insights from Sp conversions. Geophys. Res. Lett. 31. https://doi.org/10.1029/2004GL020955

Wittlinger, G., Vergne, J., Tapponnier, P., Farra, V., Poupinet, G., Jiang, M., Su, H., Herquel, G., Paul, A., 2004b. Teleseismic imaging of subducting lithosphere and Moho offsets beneath western Tibet. Earth Planet. Sci. Lett. 221, 117–130. https://doi.org/10.1016/S0012-821X(03)00723-4

Xia, B., Artemieva, I.M., Thybo, H., Klemperer, S.L., 2023. Strong variability in the thermal structure of Tibetan lithosphere. J. Geophys. Res. Solid Earth 128, e2022JB026213. https://doi.org/10.1029/2022JB026213

Yang, X., Lay, T., Xie, X.-B., Thorne, M.S., 2007. Geometric spreading of Pn and Sn in a spherical earth model. Bull. Seismol. Soc. Am. 97, 2053–2065. https://doi.org/10.1785/0120070031

Zhang, Z., Wang, Y., Houseman, G.A., Xu, T., Wu, Z., Yuan, X., Chen, Y., Tian, X., Bai, Z., Teng, J., 2014. The Moho beneath western Tibet: Shear zones and eclogitization in the lower crust. Earth Planet. Sci. Lett. 408, 370–377. https://doi.org/10.1016/j.epsl.2014.10.022

Zhao, G., Liu, J., Chen, B., Kaban, Mikhail.K., Zheng, X., 2020. Moho beneath Tibet based on a joint analysis of gravity and seismic data. Geochem. Geophys. Geosystems 21, e2019GC008849. https://doi.org/10.1029/2019GC008849

Zhao, L.-S., Helmberger, D.V., Harkrider, D.G., 1991. Shear-velocity structure of the crust and upper mantle beneath the Tibetan Plateau and southeastern China. Geophys. J. Int. 105, 713–730. https://doi.org/10.1111/j.1365-246X.1991.tb00807.x

Zhu, L., Helmberger, D.V., 1996. Intermediate depth earthquakes beneath the India-Tibet Collision Zone. Geophys. Res. Lett. 23, 435–438. https://doi.org/10.1029/96GL00385

Supplementary Materials for:

Numerous Tibetan lower-crustal and upper-mantle earthquakes, detected by *Sn/Lg* ratios, suggest crustal delamination or drip tectonics

Xiaohan Song, Simon L. Klemperer
Department of Geophysics, Stanford University, Stanford, CA 94305, USA

<u>**Sections**</u>

<u>**Tables Attached Separately**</u>

S1. Definition of Sn and Lg windows for synthetics & data

Our picking of Sn and Lg phases is based on ray tracing in a simple 1-D model with uniform crust and mantle and depends only on epicentral distance and source depth. We set the Sn onset time, T_{Sn}, to be the S head-wave arrival (Sn) for crustal earthquakes and the direct S arrival for mantle earthquakes. The Lg onset time, T_{Lg}, is set to be the direct S arrival (Sg) for crustal earthquakes, and for sub-Moho earthquakes is taken as direct S from the Moho vertically above the earthquake (Fig. S1-1). T_{Sn} and T_{Lg} can be calculated through the following equations in which R is the epicentral distance, d is the source depth, H is the Moho depth, and v_{sc} and v_{sm} are crustal and mantle shear wavespeeds:

$$T_{Lg} = \frac{\sqrt{R^2 + d^2}}{v_{sc}}$$ Lg arrival for crustal earthquakes (eqn. S1.1a)

$$T_{Lg} = \frac{\sqrt{R^2 + H^2}}{v_{sc}} + \frac{d - H}{v_{sm}}$$ Lg arrival for mantle earthquakes (eqn. S1.1b)

$$T_{Sn} = \frac{R}{v_{sm}} + (2H - d) * \frac{\sqrt{v_{sm}^2 - v_{sc}^2}}{v_{sm} v_{sc}}$$ Sn arrival for crustal earthquakes (eqn. S1.1c)

$$T_{Sn} = \frac{\sqrt{x^2 + (d - H)^2}}{v_{sm}} + \frac{\sqrt{(R - x)^2 + H^2}}{v_{sc}}$$ Sn arrival for mantle earthquakes (eqn. S1.1d)

where x is the solution of:

$$\frac{x}{v_{sm}\sqrt{x^2 + (d - H)^2}} = \frac{R - x}{v_{sc}\sqrt{(R - x)^2 + H^2}} \qquad \text{(eqn. S1.2)}$$

For our synthetics, d, H, and R are fixed and known, as is the velocity structure (v_{sc}, v_{sm}). For the real data, d is set at the catalog depth; H is set at 70 km; and R is sufficiently well-known. Crustal and mantle wavespeed are defined as $v_{sc} = 3.7$ km/s and $v_{sm} = 4.7$ km/s.

The windows in which we pick the Sn and Lg amplitudes, L_{Sn} and L_{Lg}, have lengths set to be 4 and 5 times of the source-receiver distance in degrees, respectively. The Sn window begins at $T_{Sn} - 0.2L_{sn}$, and the Lg window begins at $T_{Lg} - 0.1L_{Lg}$. When the two windows overlap at short offsets, the Sn window is truncated at $T_{Lg} - 0.05L_{Lg}$ and the Lg window starts at this time. Our method differs slightly from some previous studies that use maximum and minimum mantle and crustal velocities ("velocity-range" method) to determine the start and end of the Sn and Lg windows (Mousavi et al., 2014; Wang and Klemperer, 2021). Our method (Fig. S1-2a) is almost equivalent to the velocity-range method if v_{sm} is in the range 4.2–4.9 km/s and v_{sc} 3.2–3.8 km/s (Fig. S1-2b) and our windows are very comparable to those used by Wang and Klemperer (2021) who used v_{sm} from 4.3–4.8 km/s and v_{sc} from 3.1–3.6 km/s. We prefer our window-determination method because we include a few seconds of the waveform before the predicted earliest arrivals to more-certainly capture the phase onset, and because we only require two parameters, average v_{sm} and v_{sc}, instead of four (max and min v_{sc} and max and min v_{sm}).

We select 250 km to be the minimum distance for our Sn/Lg analysis, beyond which a significant fraction of the Sn and Lg windows should not overlap, even though some overlap remains out to $R \sim 400\text{–}500$ km (Fig. S1-2). To test the sensitivity of measured Sn/Lg to uncertainties in H, d, v_{sc}, v_{sm}, we use our synthetics for the 70-km single-layer crust (Fig. 3A) and re-calculate Sn and Lg windows and resultant Sn/Lg amplitude ratio for different values of earthquake depth d, Moho depth H, crustal wavespeed v_{sc} and mantle wavespeed v_{sm} (Fig. S1-3).

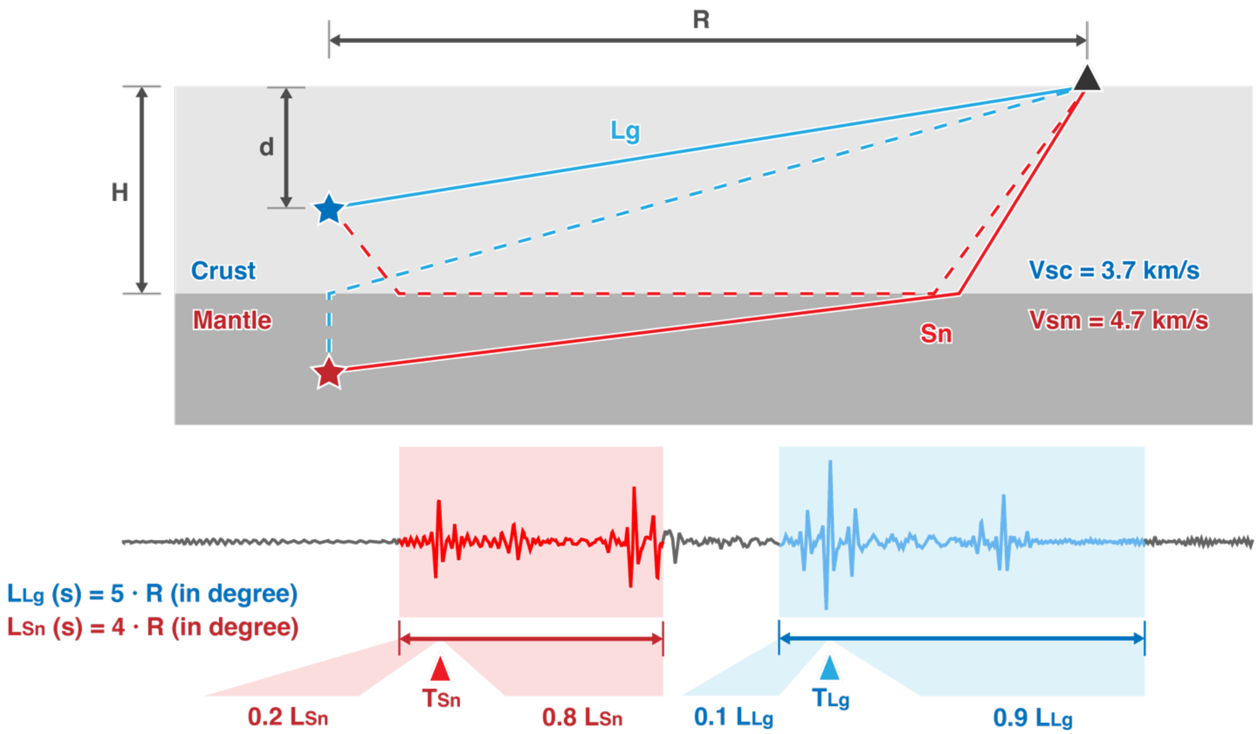

Fig. S1-1. Ray paths used to calculate the windows in which Sn and Lg phases arrive, and definitions of window lengths L_{Sn} and L_{Lg}.

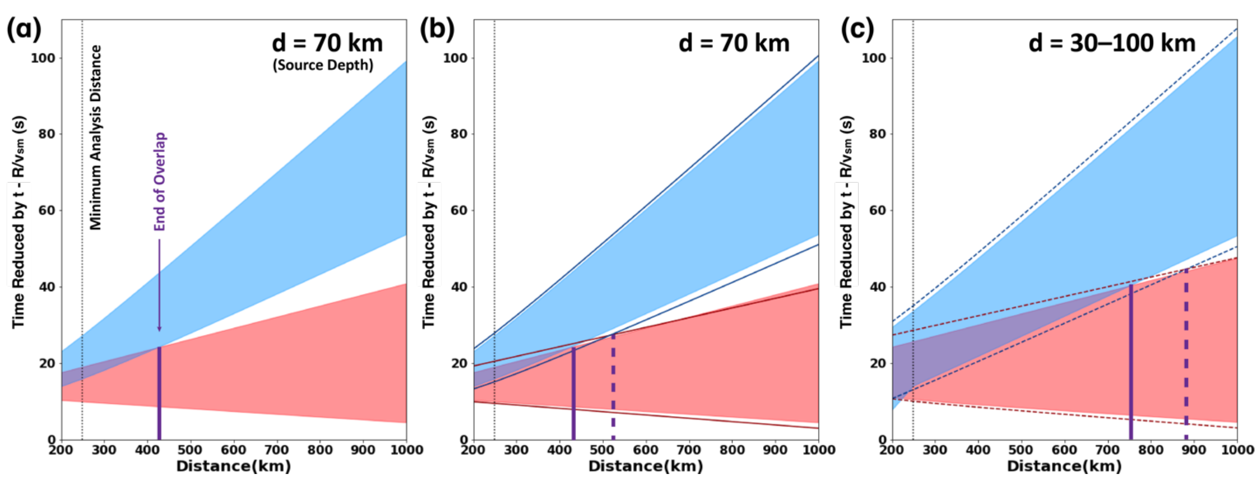

Fig. S1-2. Window ranges for Sn and Lg phases (reduced travel-time vs. offset). (a) Windows determined as in Fig. S1-1 with fixed source depth 70 km. Red: Sn window. Blue: Lg window. **(b)** as (a), with addition of lines representing windows determined by velocity-range methods (v_{sm}: 4.2–4.9 km/s; v_{sc}: 3.2–3.8 km/s) with fixed source depth 70 km. **(c) Window ranges determined for source depths 30–100 km.** Oblique solid and dashed lines: window ranges determined with our method and velocity-range method, respectively. In all three parts, vertical dotted line marks the 250-km cut-off distance below which we do not attempt to measure Sn/Lg ratios, and vertical solid and dashed lines mark the distance beyond which the Sn and Lg windows no longer overlap under different scenarios.

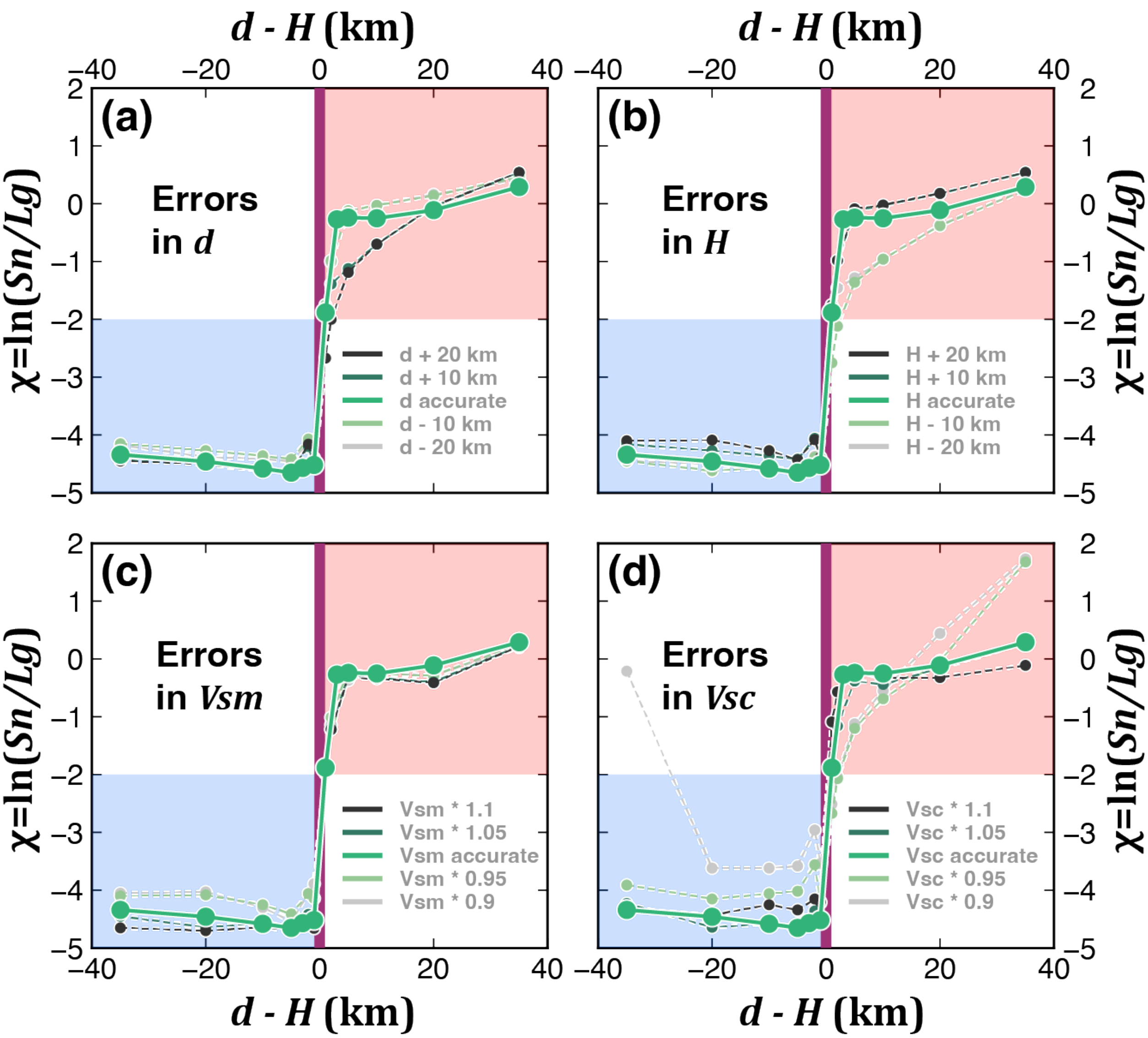

Fig. S1-3. Effect of uncertainties in d, H, v_{sm}, and v_{sc} on $\ln(Sn/Lg)$.

A 20-km variation of H and d ($> 25\%$) has limited influence on the Sn/Lg vs $d - H$ plots, meaning that our Sn/Lg method is robust to uncertain Moho and source depths (Fig. S1-3 a, b). A 10% uncertainty in the mantle S wavespeed is similarly unimportant (Fig. S1-3 c). However, 10% uncertainty in average crustal shear wavespeed can potentially have a dramatic effect on Sn/Lg (Fig. S1-3 d) if a lower-then-expected v_{sc} delays Lg arrivals beyond the Lg window so artificially increases the measured Sn/Lg. Fortunately, Sn and Lg in Tibet are well characterized with onset velocities of 4.6 and 3.6 km/s at regional distances (McNamara et al., 1995a) and our Lg windows capture all arrivals down to $v_{sc} = 3.2$ km/s.

We further demonstrate (Fig. S1-4) the robustness of our observations to incorrect source depths that produce inappropriate window lengths. We compare our preferred Sn/Lg measurements made using catalog hypocentral depths to Sn/Lg measurements made using a fixed hypocentral depth of 60 km for WT (Fig. S1-4a, b) and for ST (Fig. S1-4c, d). Almost no changes to the Sn/Lg ratios are visible.

For the phase picking model applied in our main study, we set the Moho depth H to be 70 km, the mantle S-wave velocity $v_{sm} = 4.7\ km/s$, and the crustal S-wave velocity $v_{sc} = 3.7\ km/s$. Even a 5% reduction in regional wavespeeds ($v_{sm} \leq 4.5$ km/s; $v_{sc} \leq 3.5$ km/s) or 5% increase ($v_{sm} \geq 4.9$ km/s; $v_{sc} \geq 3.9$ km/s) seems quite unlikely (McNamara et al., 1995a).

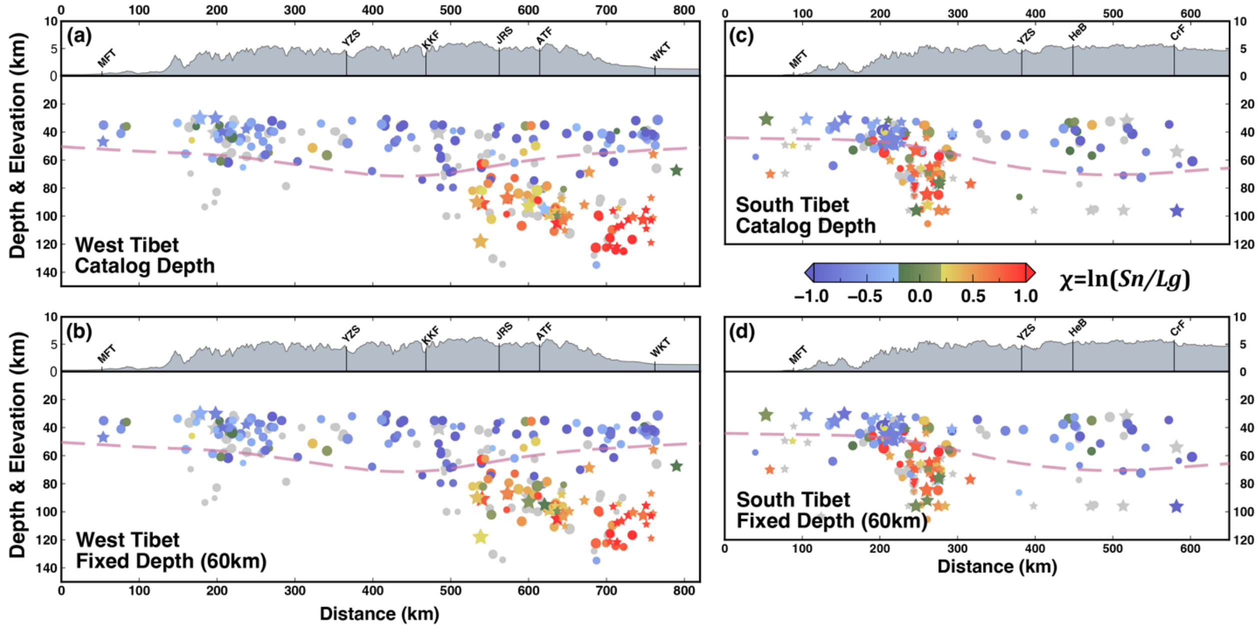

Fig. S1-4. Cross-sections of Sn/Lg along profiles in Figs. 4 and 5, using the same legends and colorscale. **(a) (c) Cross-sections of west and south Tibet with Sn and Lg values and windows calculated using catalog depths for every earthquake. (b) (d) Same profiles but with Sn and Lg values and windows calculated using a fixed source depth (60 km).**

S2. Flattened velocity model

The input model for our GESC synthetics is the simplified Tibetan velocity model of Zhao et al. (1991). GESC expects a flattened earth model, so here we show the implied spherical-Earth velocity & density model calculated from the flattened input model (Fig. S2). Velocity differences caused by the flattening transform are <6%, within the tolerance of our Sn/Lg method (Fig. S1-3).

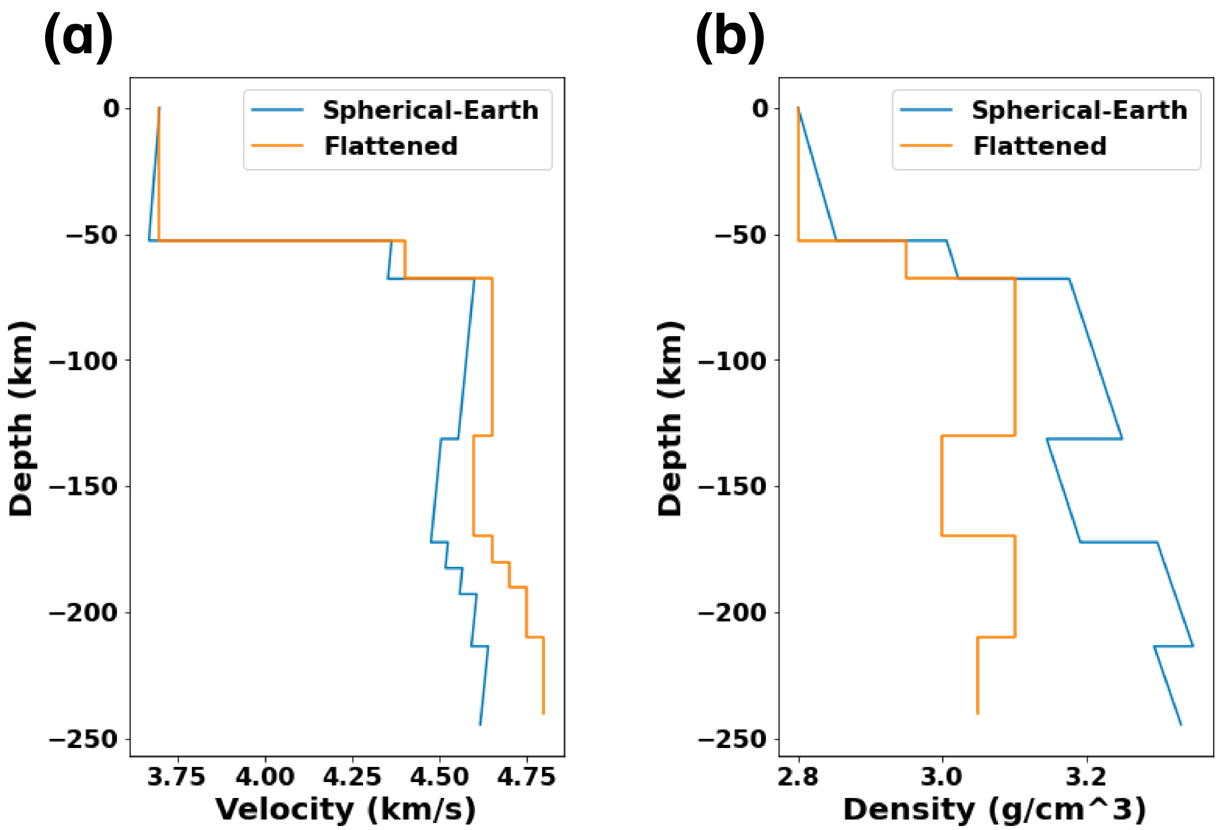

Fig. S2. Comparison between the flattened and spherical-Earth models. (a) velocity; (b) density.

S3. Catalog selection and robustness

We use histograms of the depth distribution of earthquakes to check there is no temporal bias of the USGS-NEIC PDE locations (Fig. S3-1). Aside from the peaks in the USGS-NEIC histograms representing earthquakes arbitrarily assigned to 10 km, 33 km, or 35 km, the histogram for 1999-2007 (after IC.LSA data became available) (Fig. S3-1b) and 2008-2021 (after IU.KBL provided data) (Fig. S3-1c) have similar features. Most earthquakes locate above 60 km and only very few are deeper. In contrast, the histogram for 1991-1998 (which we did not use as neither LSA nor KBL was operational) (Fig. S3-1a) has a more uniform distribution with depth, likely indicative of larger depth errors because of the paucity of stations at that time.

We also compare the USGS histograms in our south Tibet (ST) catalog with regional catalogs from previous studies in this area (Jiang et al., 2009; Michailos et al., 2021; Monsalve et al., 2006). All four catalogs show an earthquake cluster around 70 km depth. The minor variations between the three relocation catalogs that have different but shorter timescales suggest differences between the USGS histogram and the other three are unimportant.

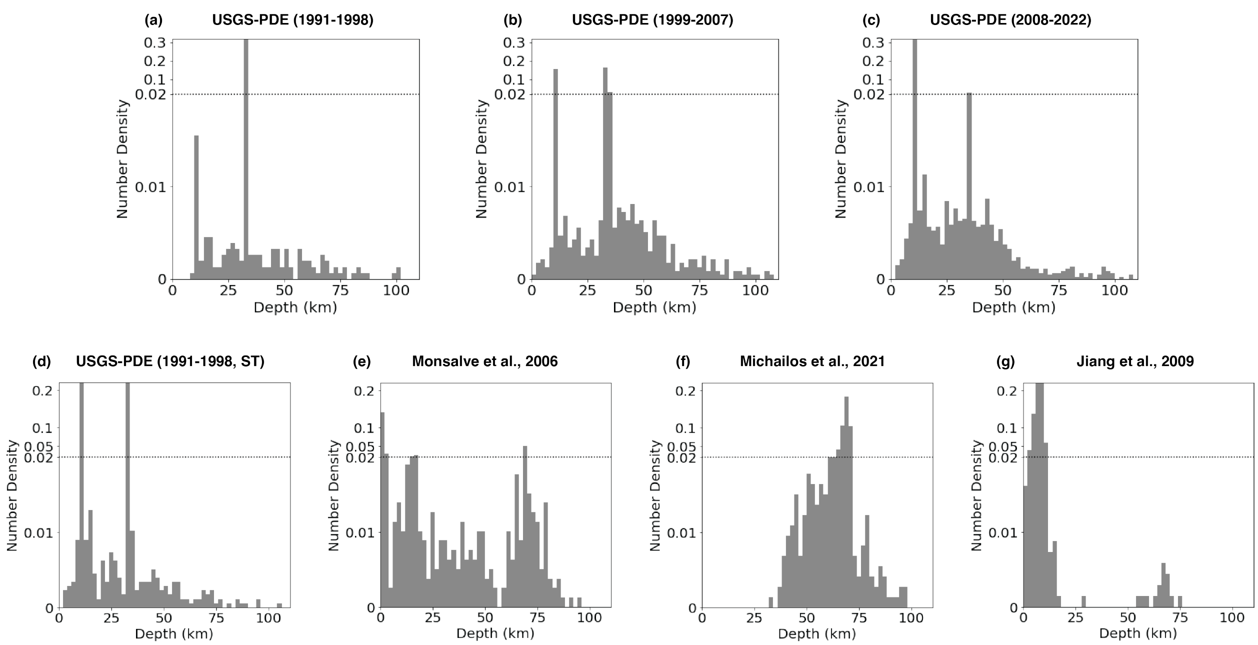

Fig. S3-1. (a - c). Histograms of the earthquake depths in USGS-PDE catalogs for three different epochs. Number densities are calculated in 2 km bins. **(d - g). Histograms for earthquake depths for South Tibet only in four different catalogs.** Note scale change in ordinate (number density) at 0.02. Note the catalog of Michailos et al. (2021) only includes events with initial depth determinations > 40 km.

We compared USGS-PDE catalog depths and the ISC-GEM, GCMT, Craig et al. (2012) and Baur (2007) catalog depths across our entire Tibet study region to help evaluate depth uncertainty (Fig. S3-2). 155 events with PDE depths ≥30 km (Fig. S3-2a, central and right columns with depth ≥30 km) also appear in one of these other four catalogs (for simplicity here we ignore additional compilations (Alvizuri and Hetényi, 2019; Bloch et al., 2021; Diehl et al., 2017; Michailos et al., 2021; Monsalve et al., 2006; Parija et al., 2018) that are limited in time and space and have very few overlapping earthquakes). Of 374 events with PDE depths <30 km (Fig. S3-2a, left column), only 14 (< 5%) are likely deeper, but none have published locations >40 km. Of 138 events with PDE depths from 30 to 60 km (Fig. S3-2a, central column), only 49 (~one-third) are confirmed as deep (>30 km) events by another catalog; but of the 17 events with PDE depths >60 km (Fig. S3-2a, right column) the large majority (15, ~90%) also have hypocentral depths >60 km in at least one of the four nominally more accurate catalogs (Fig. S3-2a, top right corner). Fig. S3-2b shows that the individual events shown in Fig S3-2a can have very large discrepancies between catalogs. The three different PDE events with depths from 55–60 km appear respectively 40-km deeper in the GCMT catalog, at the same depth in Baur (2007) and 30-km shallower in GCMT. But our ‘better-located’ catalogs also have significant uncertainty: two events with PDE depths ~70–80 km have GCMT depths ~10-km shallower than the Craig et al. (2012) re-location, and a third has a GCMT depth ~25-km deeper than in Craig et al. (2012).

These results inform the likelihood that we have missed additional deep earthquakes, or calculated *Sn/Lg* ratios for shallow events <30 km, when working with PDE events not reported elsewhere. We did not calculate *Sn/Lg* ratios for the 379 PDE events not sufficiently well-recorded to appear in other catalogs that have depths <30 km (or for PDE events with depths fixed at 10.0 km which we expect to have the largest uncertainty) (Fig. S3-2c). We may thereby have missed ~15 events with true depths >30 km, but likely no events below 60 km, based on the 374 PDE earthquakes above 30 km for which we also have ‘better locations’ (Fig. S3-2a). 325 PDE events in the range 30–60 km but not reported elsewhere passed our *Sn/Lg* SNR test, and are included in our catalog, even though Fig. S3-2a suggests that ~ 200 of these have true depths < 30 km. A handful of these 325 events also likely have true depths >70 km (2 of 138 in this depth range were re-categorized to >70 km in Fig. S3-2a, b), so potentially are mantle events that, if correctly determined as such by our *Sn/Lg* method, would be recorded as failures of our method (Supplementary Material S7). Of 107 PDE events with depths >60 km, not reported elsewhere but that passed our *Sn/Lg* SNR test, a dozen are statistically likely to be upper-crustal events, and again if correctly determined as such by our *Sn/Lg* method would be recorded as failures of our method (Supplementary Material S7).

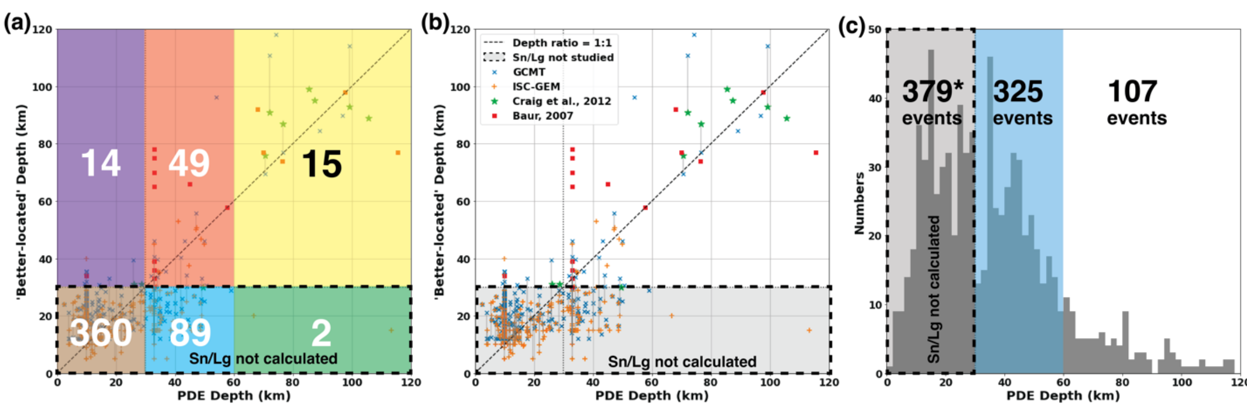

Fig. S3-2. (a) Depth comparison between the USGS PDE catalog and the ISC-GEM, GCMT, Baur (2007) and Craig et al. (2012) locations, showing number of events in different parts of the plot. (b) Same plot with no overlay. Vertical lines link same event in two different ‘better-located’ catalogs. Shaded region marks the events not included in our Sn/Lg analysis. **(c)** Depths **of PDE** earthquakes that do not appear in any other catalog. Above 30 km this excludes all events with depth fixed at 10.0 km; below 30 km we exclude earthquakes with assigned 33 km or 35 km depths, and depths that lack uncertainties, and only include events which passed our *Sn/Lg* SNR threshold.

Our primary catalog includes all $m \geq 3.5$ earthquakes with $d \geq 30$ km from 1998-2021 from the PDE catalog. We first delete those earthquakes located at exactly 33 km or 35 km depth for which no uncertainties were given. We also search all other catalogs which likely have better depth locations, including ISC-GEM, GCMT, and previous relocation & focal-mechanism studies, selecting all $m \geq 3.2$ earthquakes. Duplicate earthquakes are removed, and a single catalog depth assigned to each event duplicated in multiple non-USGS catalogs, prioritizing the relocation study with the smallest quoted uncertainty, then GCMT and ISC locations depending on which catalog gives smaller depth uncertainty. All these better-located earthquakes are marked with stars on figures in the main text.

For the better-located events (stars in Fig. 1B), ‘better-located depth’ minus ‘PDE depth’ averages +9 km, has an average absolute value of 15 km, and an RMS difference of 18 km.

S4. Calculation of Sn/Lg and $\ln(Sn/Lg)$ and their uncertainties

We measure the root mean square (RMS) amplitudes, A_{sn} and A_{Lg}, of the Sn and Lg-windows. We measure the noise amplitude A_{noise} in a window from 30–15 s before the calculated first P arrival. We measure the signal-to-noise ratio (SNR) for both windows ($SNR_{Lg} = A_{Lg}/A_{noise}$; $SNR_{Sn} = A_{Sn}/A_{noise}$) and discard all earthquakes for which both $SNR_{Lg} < 3$ and $SNR_{Sn} < 3$. For the remaining earthquakes we calculate the Sn/Lg ratio and the uncertainties of the Sn and Lg amplitudes, σ_{Sn} and σ_{Lg}. Finally, we calculate the uncertainties in Sn/Lg and $\ln(Sn/Lg)$:

$$Sn/Lg = \frac{A_{Sn}}{A_{Lg}} \qquad \text{(eqn. S4.1)}$$

$$\sigma_{Sn/Lg} = \sqrt{\frac{\sigma_{Sn}^2}{A_{Lg}^2} + \frac{A_{Sn}^2\sigma_{Lg}^2}{\left(A_{Lg}^2\right)^2}} \qquad \text{(eqn. S4.2)}$$

$$\sigma_{\ln(Sn/Lg)} = \frac{\sigma_{Sn/Lg}}{Sn/Lg} \qquad \text{(eqn. S4.3)}$$

An important note is that this uncertainty estimation only takes into consideration random noise. In real seismograms, both in this paper (Tables SA, SB, SC) and as shown by Wang and Klemperer (2021, their Fig. S10), the influence of SH-converted P wave can be non-negligible. We lack a simple method to account for this high-frequency Rayleigh-Love coupling.

In addition to calculating the Sn/Lg amplitude ratios using RMS amplitudes, we also test using peak amplitudes:

$$Sn/Lg = \frac{\max\{|Sn|\}}{\max\{|Lg|\}} \qquad \text{(eqn. S4.4)}$$

The difference between the Sn/Lg peak amplitude ratios (Eqn. S4.4) and the Sn/Lg RMS ratios (Eqn. S4.1) for the seismograms on which we measured Sn/Lg (Fig. S4) is typically $< \pm\, 0.3$ (natural log value) (Fig. S4). Although there are some outliers, we find no important statistical differences in our Sn/Lg analysis between using these two Sn/Lg calculation methods. Accordingly, RMS amplitudes are used throughout this paper.

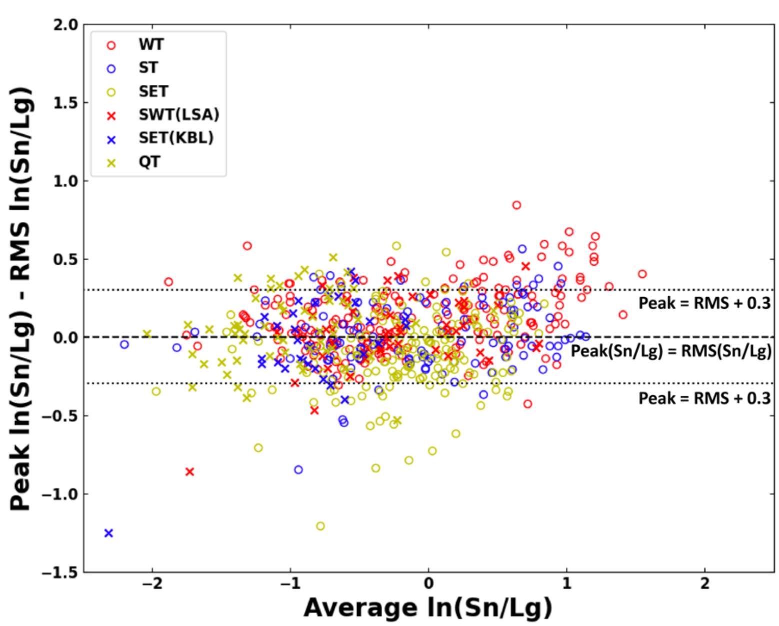

Fig. S4. Difference between $\ln(Sn/Lg)$ RMS ratios and $\ln(Sn/Lg)$ Peak ratios for all events with acceptable SNR, plotted against mean $\ln(Sn/Lg)$.

S5. Geometric spreading detrend

The recorded amplitude is influenced by multiple effects (Hasegawa, 1985; Wang and Klemperer, 2021):

$$A(f,R) = S(f)G(R,f)\psi(R,f)I(f)P(f) \qquad \text{(eqn. S5.1)}$$

where A is the recorded amplitude as a function of frequency f and epicentral distance R, S is the source amplitude, G is the geometric spreading factor, ψ is the intrinsic attenuation, I is the instrument response, and P is the site response. For a single station, I and P can be neglected. ψ is discussed in the main paper (Section 5-Discussion). We use a theoretically derived G to detrend our data. Even though this is a second order correction to the Sn/Lg ratios, it is helpful in comparing the results from two regions with different receiver distances, albeit unnecessary for Sn/Lg analysis in a small region.

We approximate $G(R,f)$ for Sn and Lg (Fan and Lay, 2003; Wang and Klemperer, 2021; Yang, 2002; Fig. S5). We assume $\log_{10}(G_{Sn})$ is flat out to 800 km distance then increases at $0.0006/\text{km}$. We assume $\log_{10}(G_{Lg})$ decreases at $0.00025/\text{km}$. Using a reference distance of 500 km, we detrend our data by multiplying the amplitudes, A_{Sn} and A_{Lg}, with the coefficients:

$$K_{Sn} = -10\text{^}[(0, R - 800\text{ km})_{max} * 0.0006/\text{km}] \qquad \text{(eqn. S5.2a)}$$

$$K_{Lg} = 10\text{^}[(R - 500\text{ km}) * 0.00025/\text{km}] \qquad \text{(eqn. S5.2b)}$$

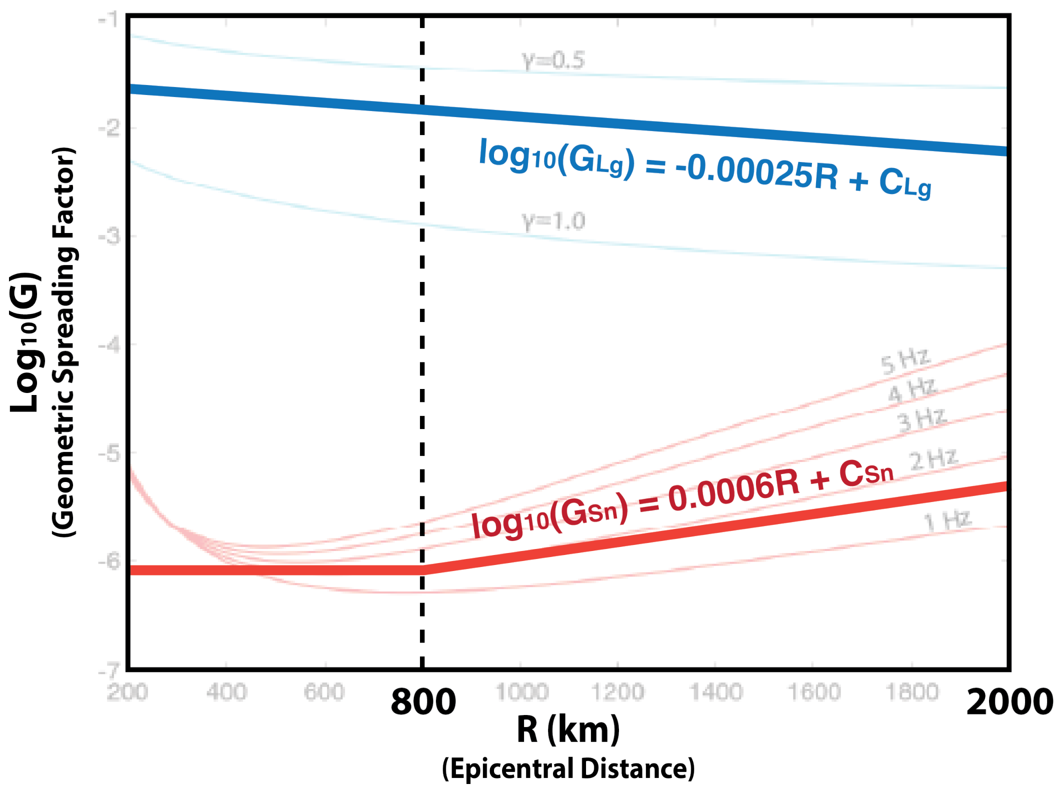

Fig. S5. Geometric spreading curves $G(R,f)$ for Sn (red) and Lg (blue) from Wang and Klemperer (2021) for different frequency & γ (Lg spreading exponent). Thick lines represent the simplified function used for detrending in this research. C_{Sn} and C_{Lg} are arbitrary constants.

S6. Demonstration of step-change in $\chi(d-H)$ and estimation of the separation threshold

It is not immediately obvious whether our observed $\chi = \ln(Sn/Lg)$ vs. $d-H$ plots show a gradational increase in χ with no change at the Moho, or a step-change in χ across some threshold value that separates below-Moho from above-Moho earthquakes. We address this by finding the best linear fit to $\chi(d-H)$, then using this fit to de-trend χ and checking the residual signal. If χ has a linear relationship to $(d-H)$ with a normally distributed uncertainty σ_χ (eqn. S6.1; Fig. S6-1a), the detrended χ, here written $\tilde{\chi}$, must follow the normal distribution $\mathcal{N}(0,\sigma_\chi)$ which is independent of $d-H$ (eqn. S6.2; Fig. S6-1b):

$$\chi(d-H) = a(d-H) + b + \mathcal{N}(0,\sigma_\chi) \qquad \text{Linear trend (eqn. S6.1)}$$

$$\tilde{\chi}(d-H) = \chi - a(d-H) - b = \mathcal{N}(0,\sigma_\chi) \qquad \text{(eqn. S6.2)}$$

i.e. the residual after de-trending χ has no structure (Fig. S6-2b).

However, if the underlying data distribution has a step-change described e.g. by the following equations:

$$\chi(d-H) = \begin{cases} \mathcal{U}(0,\chi_{lim}), & (d-H>0) \\ \mathcal{U}(-\chi_{lim},0), & (d-H<0) \end{cases} \qquad \text{Step change-U (eqn. S6.3)}$$

or

$$\chi(d-H) = \begin{cases} \mathcal{N}(\chi_{avg},\sigma_\chi), & (d-H>0) \\ \mathcal{N}(-\chi_{avg},\sigma_\chi), & (d-H<0) \end{cases} \qquad \text{Step change-N (eqn. S6.4)}$$

we can then observe a second-order structure in the detrended χ scatter plots, in this case, a zigzag trend around $\tilde{\chi} = 0$ (Fig. S6-1d, f).

We first conduct a test on synthetic $\chi = \ln(Sn/Lg)$ scatter plots. We generate three 200-point scatter plots based on distributions given by eqn. S6.1, eqn. S6.3 and eqn. S6.4 (Figs. S6-1a,c,e). We chose $\sigma_\chi = 0.5$ (the observed r.m.s. variation of $\tilde{\chi}$ for WT), $\chi_{lim} = 1.5$ (most of our observations lie within $\chi \in (-1.5, 1.5)$ (Fig. 4B1), and $\chi_{avg} = 0.75$ (half of χ_{lim})). We use a synthetic bimodal earthquake-depth distribution (Fig. S6-1g) as is observed for WT earthquakes (Fig. 4B1). We calculate the moving average of $\tilde{\chi}$ across a 15-km depth window. For the linear relationship between χ and $(d-H)$ (eqn. S6.1) there is no second-order trend (Fig. S6-1b), but for the step-change relationships between χ and $(d-H)$ (eqns. S6.3, S6.4) the second-order trend zigzags across the zero line, including a zero-crossing at $d-H=0$ (Figs. S6-1d,f). Substituting the value of $d-H$ at the central zero-crossing back into the best-fit line we obtain the best separation threshold for χ, in this case $\chi = 0$.

We apply the same method to our actual observations (Fig. S6-2). Both WT and ST show a clear pattern in $\tilde{\chi}$, with negative values for $(d-H) < \sim 0$ then positive values for $(d-H) > \sim 0$ (Figs. S6-2b,d). For WT, the maximum value of the moving average $\tilde{\chi} \approx 0.4$ (Fig. S6-2b), a value approaching our synthetic test results. The SET moving average $\tilde{\chi}$ has a much weaker, but still visible, negative-then-positive zigzag (Fig. S6-2f).

We can show that $\tilde{\chi}$ statistically supports a step-change by comparing the peak of the moving average of $\tilde{\chi}$ with the expected variance of the moving average, and showing that the observed moving average deviates too far from zero for our data to represent a gradational variation of χ with $(d-H)$. If we assume that the points $\tilde{\chi}_i$ (the detrended individual observation of χ, one for each earthquake) follow a normal distribution $\mathcal{N}(0,\sigma_\chi)$ (eqn. S6.1), their average will have a probability distribution function of $\mathcal{N}(0,\sigma_\chi/\sqrt{N})$ where N is the number of points. Taking the WT data for example, σ_χ is estimated to be 0.5, and N, the number of $\tilde{\chi}_i$ points within a

15-km window, ranges from 15 to 30 (for window centers less than 20 km from the zero-crossing point). The standard deviation of the moving average for WT is therefore $\sigma_{AVG\_WT} = \sigma_\chi/\sqrt{N} \approx 0.13$. Similarly, $\sigma_{AVG\_ST} \approx 0.13$ and $\sigma_{AVG\_SET} \approx 0.10$. In contrast, the peak absolute values of the moving averages of $\tilde{\chi}$ are about 0.4 for WT (three times σ_{AVG_WT}), 0.25 for ST (twice σ_{AVG_ST}), and 0.1 for SET ($\approx \sigma_{AVG\_SET}$). Thus, the WT χ values show a strong step-change signal, ST χ values show a moderate signal, and the SET χ values show only a weak step-change signal (Figs. S6-2b,d,f).

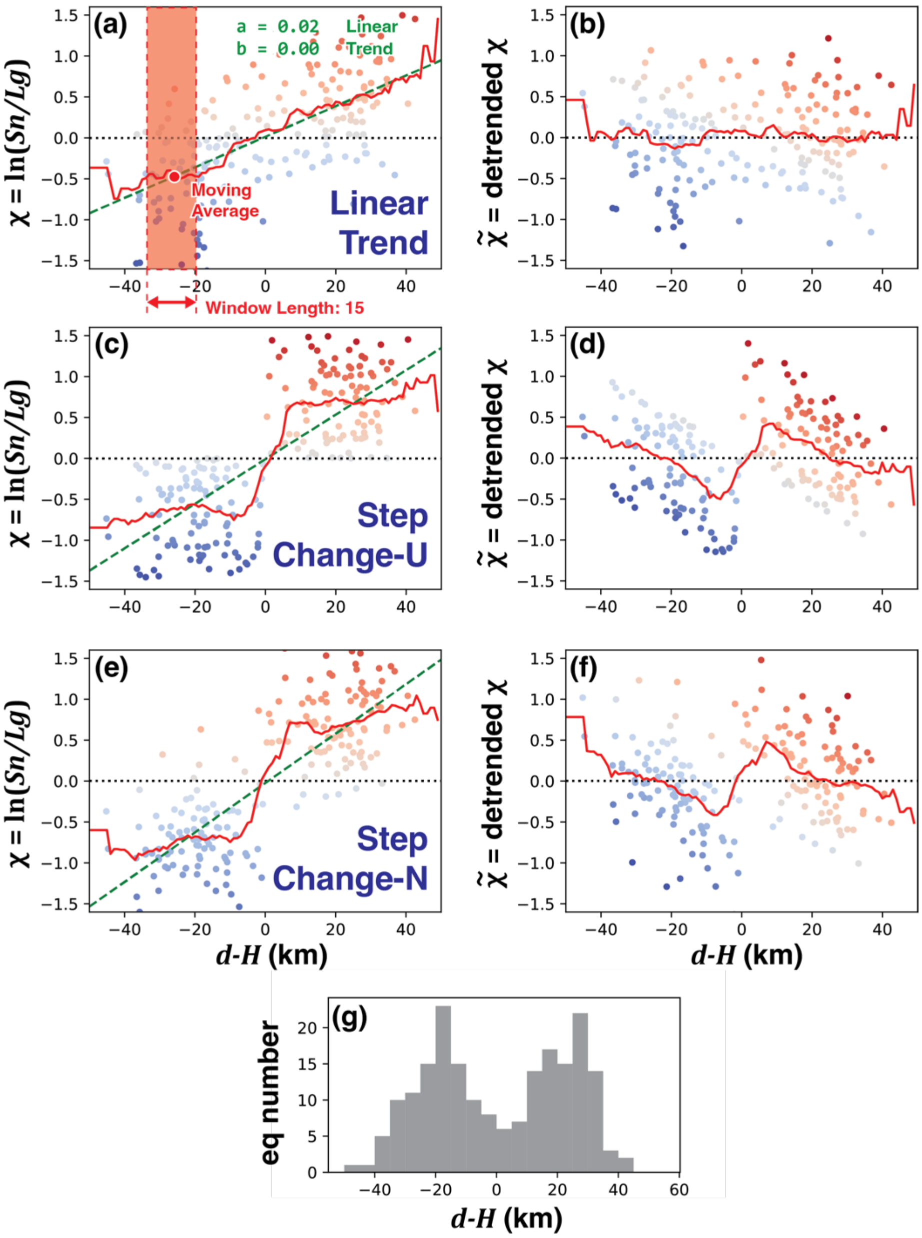

Fig. S6-1. Detrending test on synthetic χ vs. (d-H) datasets. (a) and (b). χ and $\tilde{\chi}$ (detrended χ) for a synthetic linear trend with normal distributed noise (eqn. S6-1). Green line is the best fit linear trend, defined by constants a and b (egn. S6-1). Red lines are the moving average for χ and $\tilde{\chi}$. **(c) and (d). χ and $\tilde{\chi}$ (detrended χ)** for the step-change uniform distribution (eqn. S6-3); lines plotted as in (a) and (c). **(e) and (f). χ and $\tilde{\chi}$** for the step-change normal distribution (eqn. S6-4); lines plotted as in (a) and (c). **(g). Histogram of the synthetic depths.**

Both ST and SET have zero-crossing points near $(d-H)=0$, whereas the zero-crossing point of WT data is at $(d-H)=15$ km, which means a systematically 15-km deeper Moho would provide a better fit to our WT observations. This 15-km discrepancy is visually obvious in Figs. 4C,D, in that Xia et al.'s (2021) Moho is always shallower than Zhang et al.'s (2014) Moho and Wittlinger et al.'s (2009) Moho, and that using the deeper Mohos instead of Xia et al. (2021) would better fit the measured Sn/Lg (Fig. 4C).

In Figs. S6-2a,c,f we show the best-fit linear relationship between χ and $(d-H)$ and list the appropriate constants a and b (in eqn. S6-1) for each area. Substituting the zero-crossing values of $(d-H)$ (Figs. S6-2b,d,f) into the best-fit lines for χ (Figs. S6-2a,c,e), we find the best separation thresholds are χ = 0.078 (WT), χ = -0.081 (ST) and χ = -0.152 (SET). It would be possible to use more complex schemes taking into account earthquake magnitudes, Sn/Lg uncertainties, and/or depth uncertainties in doing the linear fitting, and thereby get slightly different threshold values. Hence, for simplicity and consistency, we select $\chi=0$ to be the threshold value everywhere, and in addition we use a 'buffer zone' of $\ln(Sn/Lg)=\pm 0.2$ to ensure that we only categorize earthquakes that are convincingly on one or other side of the step change in χ. This separation at $\chi=0$ works well for our WT and ST observations (Figs. 4B1, 5B). In detail, the threshold $\chi=0$ is a little bit too high for the SET observations (Fig. 6B), but we prefer to use a single threshold for all our data.

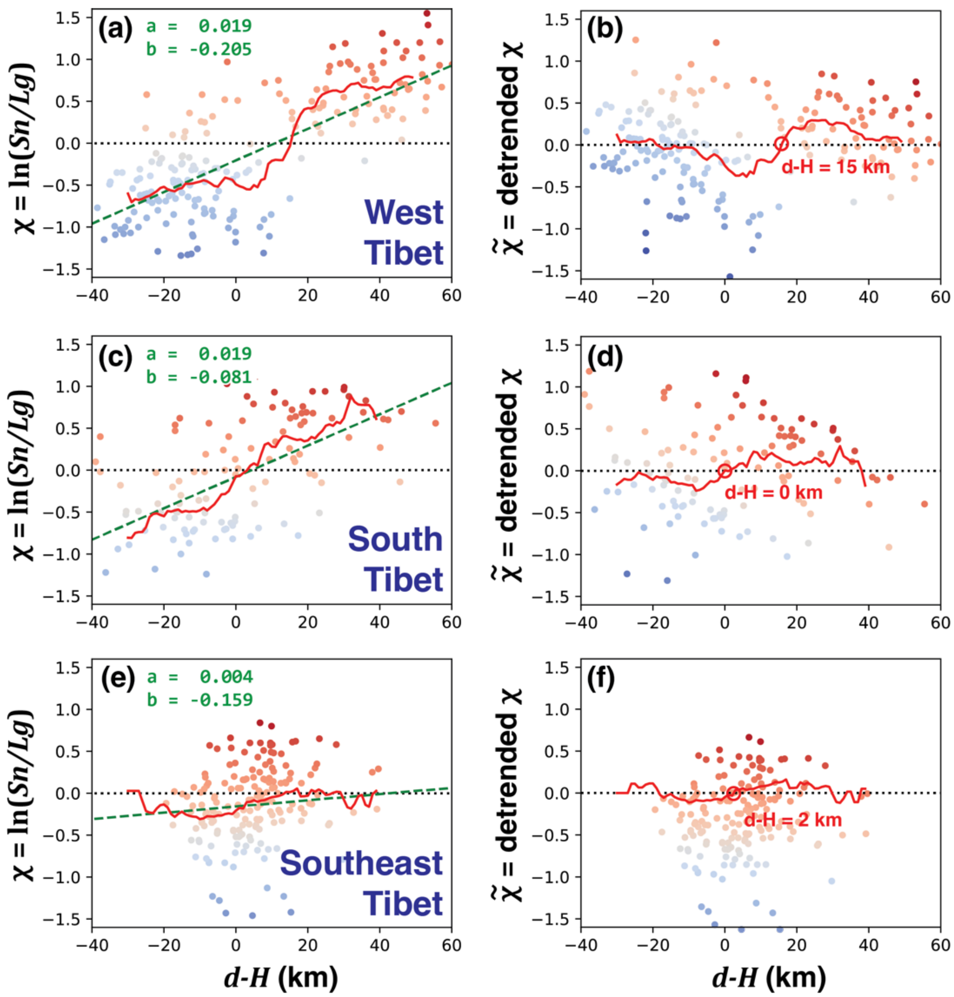

Fig. S6-2. (a) (c) and (e) $\chi=\ln(Sn/Lg)$ observations for WT, ST, and SET. As in Fig. S6-1 we show the best linear fit (dashed green lines) and moving average (red lines). **(b) (d) and (f) $\tilde{\chi}$ (detrended χ) corresponding to (a), (b) and (c),** with the central zero-crossing points of the moving averages marked by red circles. Legends as Fig. S6-1.

<u>S7. Earthquake classifications</u> as definitive or likely below- and above-Moho

We classify the earthquakes we studied into the following categories: "definitive" represents the events that the Sn/Lg and depth agree even considering the worst situation that the uncertainty allows; "likely" represents the other events for which Sn/Lg and depth agree without considering uncertainties; and "possible" represents remaining events for which Sn/Lg and depth agrees within uncertainty (Fig. S7-1). The small number of events for which the Sn/Lg ratio predicts an incorrect location with respect to Moho, even after allowing for uncertainty, are considered as failures of our method. Note that depth errors are as specified by the source catalogs and the Moho determination is assigned zero error; if these errors are too small some 'definitive' events will be downgraded to 'likely', and some 'failures' could become 'possible' successes.

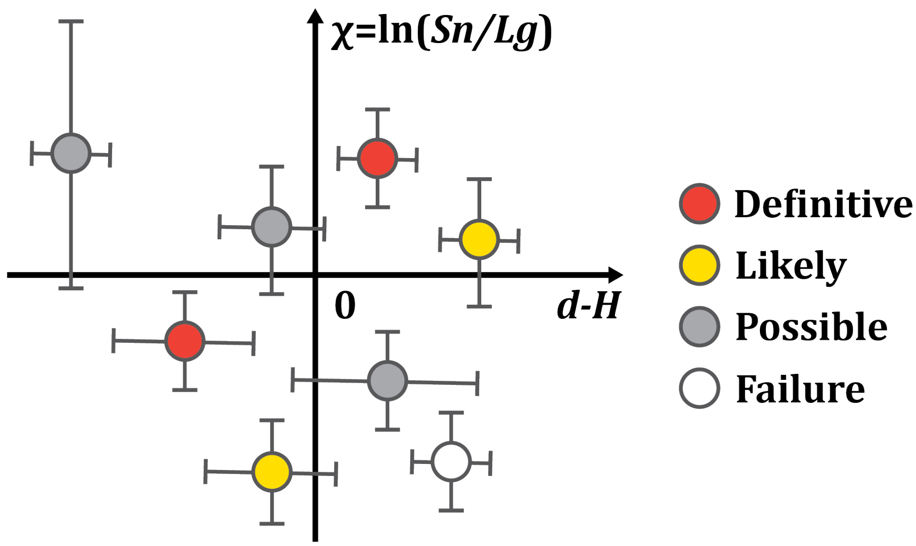

Fig. S7-1. Earthquake classification criteria.

Using only the 'better-located' earthquakes, we have a >70% success rate and <10% failure rate (Table S7-1), and indeed if we ignore SE Tibet where the Moho depth is less-well known our success rate increases to 90% and the failure rate drops to 5%. When we include the PDE-only events (Table S7-2), these percentages do not change drastically, but we see a very large proportional increase in the number of above-Moho events (for WT we show 34 below-Moho and 5 above-Moho 'better-located' events, but 38 below- and 91 above-Moho PDE-only events. We doubt these changed proportions represents bias in the GCMT and ISC-GEM catalogs even though these are only complete for m>5 earthquakes (Ammon et al., 2021; Storchak et al., 2013), because GCMT or ISC-GEM only contribute ~15% of 'better-located' events in WT and ~40% for our entire Tibet catalog. A modest effect could be the greater attention paid to deeper earthquakes, so increasing the probability that below-Moho events are over-represented in the 'better-located' category. However, we expect that the increased number of above-Moho events include a very substantial fraction of shallow seismicity mis-located in the PDE catalog: Fig. S3-2a suggests that >60% of the PDE-only events with catalog depths 30–60 km may in fact be upper-crustal earthquakes <30 km, corresponding to ~200 excess events on our cross-sections at 30–60 km. Additionally, as noted in Supplementary Material S3, we statistically expect that 10–20 events that are only in the PDE catalog are grossly mislocated, e.g., with true sub-Moho depths but located in the upper crust, or vice versa, so if correctly determined with respect to Moho by our Sn/Lg method would be recorded as failures of our method. These events could represent a substantial fraction of the ~50 total failures recorded in Table S7-2 compared to the 15 failures in Table S7-1.

Table S7-1. Classification of 'better-located' earthquakes (stars in Figs. 4–7) based on the catalog depths, RF Moho depths, Sn/Lg ratios, and their uncertainties.

	Definitive		Definitive & Likely		Possible		Failure	Success Rate	Failure Rate
	Sub Moho	Above Moho	Sub Moho	Above Moho	Sub Moho	Above Moho			
Region	$\chi > \sigma_\chi$ $d - H > \sigma_d$	$\chi < -\sigma_\chi$ $d - H < -\sigma_d$	$\chi > 0$ $d - H > 0$	$\chi < 0$ $d - H < 0$	$\chi > 0$ $-\sigma_d < d - H < 0$ Or $-\sigma_\chi < \chi < 0$ $d - H > \sigma_d$	$\chi < 0$ $0 < d - H < \sigma_d$ Or $0 < \chi < \sigma_\chi$ $d - H < -\sigma_d$	$\chi < -\sigma_\chi$ $d - H > \sigma_d$ Or $\chi > \sigma_\chi$ $d - H < -\sigma_d$	$\frac{\text{Definitive} + \text{Likely}}{\text{All}}$	$\frac{\text{Failure}}{\text{All}}$
WT	21	4	34	5	1	0	2	93%	5%
ST	13	6	20	13	2	0	2	89%	5%
SET	8	11	21	28	9	13	9	61%	11%
SWT (KBL)	0	1	0	1	0	0	0	-	-
SWT (LSA)	0	2	0	2	0	1	2	-	-
QT	0	1	0	1	0	0	0	-	-

$\chi = \ln(Sn/Lg)$

Table S7-2. As Table S7-1, but for all earthquakes, including PDE-only events.

	Definitive		Likely & Definitive		Possible		Failure	Success Rate	Failure Rate
	Sub Moho	Above Moho	Sub Moho	Above Moho	Sub Moho	Above Moho			
Region	$\chi > \sigma_\chi$ $d - H > \sigma_d$	$\chi < -\sigma_\chi$ $d - H < -\sigma_d$	$\chi > 0$ $d - H > 0$	$\chi < 0$ $d - H < 0$	$\chi > 0$ $-\sigma_d < d - H < 0$ Or $-\sigma_\chi < \chi < 0$ $d - H > \sigma_d$	$\chi < 0$ $0 < d - H < \sigma_d$ Or $0 < \chi < \sigma_\chi$ $d - H < -\sigma_d$	$\chi < -\sigma_\chi$ $d - H > \sigma_d$ Or $\chi > \sigma_\chi$ $d - H < -\sigma_d$	$\frac{\text{Definitive} + \text{Likely}}{\text{All}}$	$\frac{\text{Failure}}{\text{All}}$
WT	50	71	72	96	7	12	9	86%	5%
ST	25	24	40	50	7	4	12	80%	11%
SET	26	16	53	42	19	33	25	53%	15%
SWT (KBL)	0	21	0	28	0	1	1	93%	3%
SWT (LSA)	0	14	4	29	1	9	4	70%	9%
QT	0	27	0	44	0	11	1	79%	2%

$\chi = \ln(Sn/Lg)$

We plot the magnitude distributions for all earthquakes for which we calculated Sn/Lg, for the "definitive" & "likely" earthquakes, and for the "failure" earthquakes (Fig. S7-2). There is no clear correlation between success rate and event magnitude. However, there is a clear improvement in success rate (from 77% to 91%), and decline in failure rate (from 9% to 5%) when using only 'well-located' earthquakes (Table S7-1) compared to 'PDE-only' earthquakes (difference between Table S7-2 and S7-1, calculated for WT and ST). Most of our studied earthquakes' magnitudes are > 4.0. However, the well-located earthquakes include relocation studies from temporary arrays so contain a higher portion of $M < 4.0$ earthquakes than the PDE-only category, perhaps helping explain the lack of correlation of success rate with magnitude.

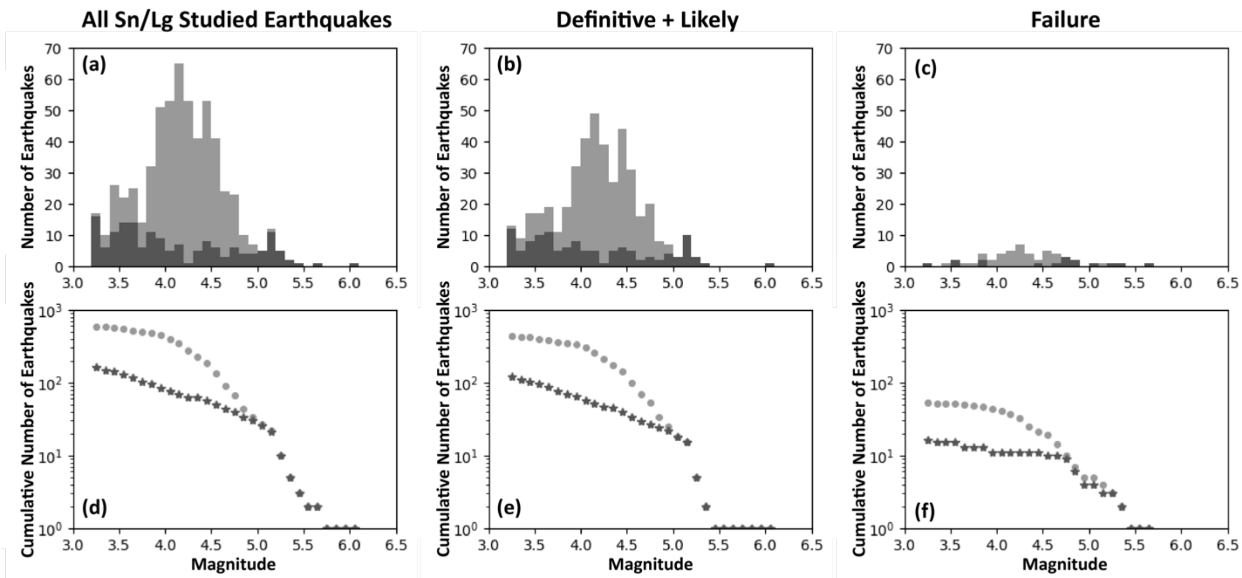

Fig. S7-2. (a–c) Histograms of earthquake number vs. magnitude and (d–f) Gutenberg-Richter plots ($\log_{10}$ cumulative earthquake number vs. magnitude). (a, d) all the studied earthquakes; (b, e) only 'Definitive + Likely' earthquakes; and (c, f) only 'Failure' earthquakes. Dark gray columns and stars denote well-located earthquakes; light gray columns and dots denote PDE-only events.

S8. Sn and Lg Blockage or Leakage

The normal-mode synthetics for Sn/Lg (Fig. 3; Wang and Klemperer, 2021) are calculated for 1-D earth models, but it is well-known that structural boundaries (e.g., Moho ramps, Fig. 2B) can modify Sn & Lg amplitudes (Kennett, 1986). The obvious binary classification and clear separation of apparently above-Moho from below-Moho earthquakes in WT (Fig. 4) suggests Sn or Lg blockage can only be a secondary-order effect. Nonetheless, we plot ray paths from the WT earthquakes to KBL on a recent Moho map (Fig. S8) inferred from gravity measurements (Zhao et al., 2020) (the RF Moho map used in Fig. 4 ((Xia et al., 2023) does not extend west to IU.KBL). Raypaths from many earthquakes in WT1 (north half) are crudely parallel to the Moho contours, so should be little affected by Sn or Lg blockage. The northeasternmost band of earthquakes (C1 in Fig. S8a) above a 55 km Moho and beneath WKT (Fig. 4) are all above Moho based both on reported depths and their low Sn/Lg, consistent with crustal paths and hence no Lg blockage. Similarly the earthquakes labelled M (Fig. S8a) beneath the surface traces of the JRS & ATF (Fig. 4) are likely all south of the ATF at depth (Wang and Klemperer, 2021) so their below-Moho assignation based on hypocentral depth and high Sn/Lg is consistent with no Sn blockage as energy travels to the SE from thicker crust. The earthquakes C2 (Fig. S8) have ray paths from thick to thin crust, so would be expected to show Lg blockage (Fig. 2B, left) but nonetheless have low Sn/Lg consistent with their nominally crustal hypocenters. Perhaps any Lg blockage in transiting from thick Tibetan crust to thin Indian crust is balanced by Sn blockage when transiting from thin Indian crust to thick Hindu Kush crust. In summary however, we have no clear examples of Sn or Lg blockage being an important effect between WT and KBL.

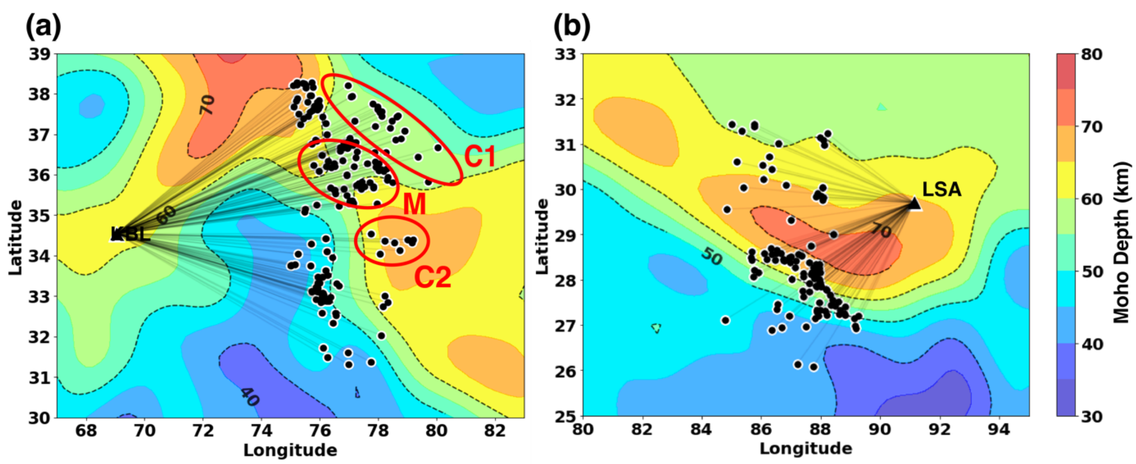

Fig. S8. Ray paths superimposed on the Moho map of Zhao et al. (2020). (a) WT earthquakes recorded at KBL. (b) ST earthquakes recorded at LSA.

Earthquakes from south Tibet recorded at LSA (Figs. 5, S8b) have a less-clear binary classification than the WT earthquakes recorded at KBL, but we have not found systematic changes in *Sn/Lg* ratios that we can associate with Sn or Lg blockage. The large discrepancy between receiver-function Moho (Xia et al., 2023) and gravity Moho (Zhao et al., 2020) (Fig. 5c) may as noted in the main text be indicative of partial ecologitization that can modify *Sn/Lg* ratios (Fig. 3b).

S9. Filter applied to the Moho map

We apply an elliptical 100 × 200 km Gaussian filter to the raw Moho data map of Xia et al. (2023) to get a representative Moho profile in our cross-sectional plots. This filter has its short axis across tectonic strike, along the profile. Standard deviations of the Gaussian filter are half of the respective axis lengths (50 km along the profile, 100 km across the profile).

S10. Comparison between LSA and KBL in west Tibet

We select the region in which earthquakes are roughly equidistant (~900-1300 km) from Kabul and Lhasa, for comparison of Sn/Lg as recorded at each station (Fig. S10). 38 earthquakes below 30 km (magenta stars and circles in Fig. S10), including 8 PDE events and 30 events from GCMT and ISC, passed our SNR criteria at both stations. All these earthquakes are located in the crust.

Earthquakes in the north part of the selected region (Qiangtang) have similar low Sn/Lg ratios at both LSA and KBL's records. However, earthquakes located south of the YZS on average have higher Sn/Lg ratios at LSA, including several events with "intermediate" or weak "mantle" Sn/Lg, including W1 (Fig. S10-B1). These differences are likely the result of lower Lg and higher crustal attenuation for Tibetan ray paths to LSA than for Indian ray paths to KBL (Fig. S8) (Taylor et al., 2003), as is also suggested by the noisier records (having larger Sn/Lg uncertainties) at Lhasa than at Kabul. Analogous effects have been explicitly shown for single Tibetan earthquakes recorded on 2D arrays that cross regions of different attenuation (Wang & Klemperer, 2021, their Fig. 7). Lg blockage due to Moho topography is probably not the cause (Supplementary Material S8): these eight earthquakes' ray paths to Lhasa travel through crust that is never thinner than at the hypocenter, so should not experience any Lg blockage (Kennett, 1986).

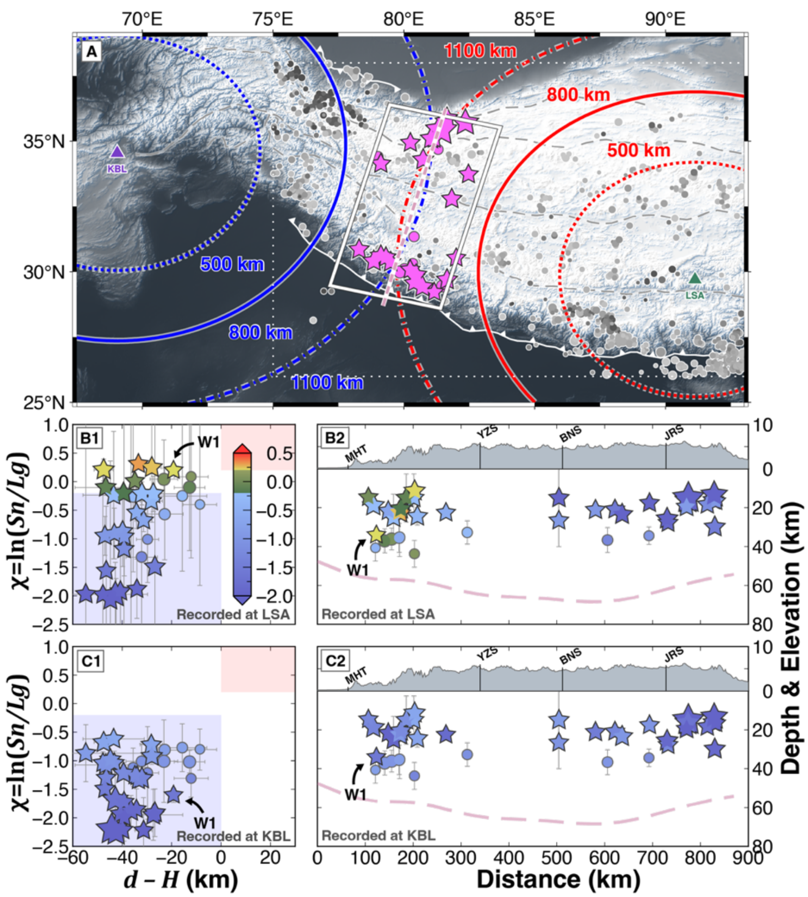

Fig. S10. (A) Earthquakes recorded with acceptable SNR at both KBL and LSA (magenta circles and stars). Red and blue circles mark distances from IC.LSA and IU.KBL respectively. White frame marks the region in which earthquakes have about the same distance to the two stations. Gray smaller dots are the other earthquakes in our catalog. Dashed pink line is the line of cross-section in B2 & C2. **(B1 & C1) Sn/Lg vs $(d - H)$ plots for the selected earthquakes from IC.LSA and IU.KBL respectively.** Legends as in Fig. 5B, but Sn/Lg color bar is modified to range from -2.0 to 0.5**. (B2 & C2): Cross-sectional view of the Sn/Lg ratios for the selected earthquakes from IC.LSA and IU.KBL respectively.** Legends as in Fig. 5C.

S11. Sn/Lg results from the Qiangtang

We obtain the Sn/Lg ratios of 56 earthquakes in the eastern Qiangtang (QT), a region with high Sn attenuation and likely high mantle temperature (McNamara et al., 1995b). Most earthquakes in this region are nominally crustal, and all but one have low Sn/Lg ratios. All 10 earthquakes nominally below the Moho are within depth uncertainty of the Moho, and nine have low Sn/Lg and one has intermediate Sn/Lg (with large uncertainty). Considering the large depth uncertainties for these earthquakes and the lack of apparent depth-dependent Sn/Lg, we conclude there is no evidence for mantle seismicity in the Qiangtang. The average Sn/Lg ratios in QT are lower than those in ST, SET, and SWT, consistent with strong source-side Sn attenuation in the Qiangtang.

The apparent existence of ~50 earthquakes nominally in the lower-crust of the hottest part of Tibet is remarkable given that the temperature likely exceeds 700℃ at 25-km depth (Wang et al., 2016). Comparison of PDE depths and 'better-located' depths (Fig. S3-2) suggests that one-third of these 50 earthquakes may have true hypocenters at >30 km depth.

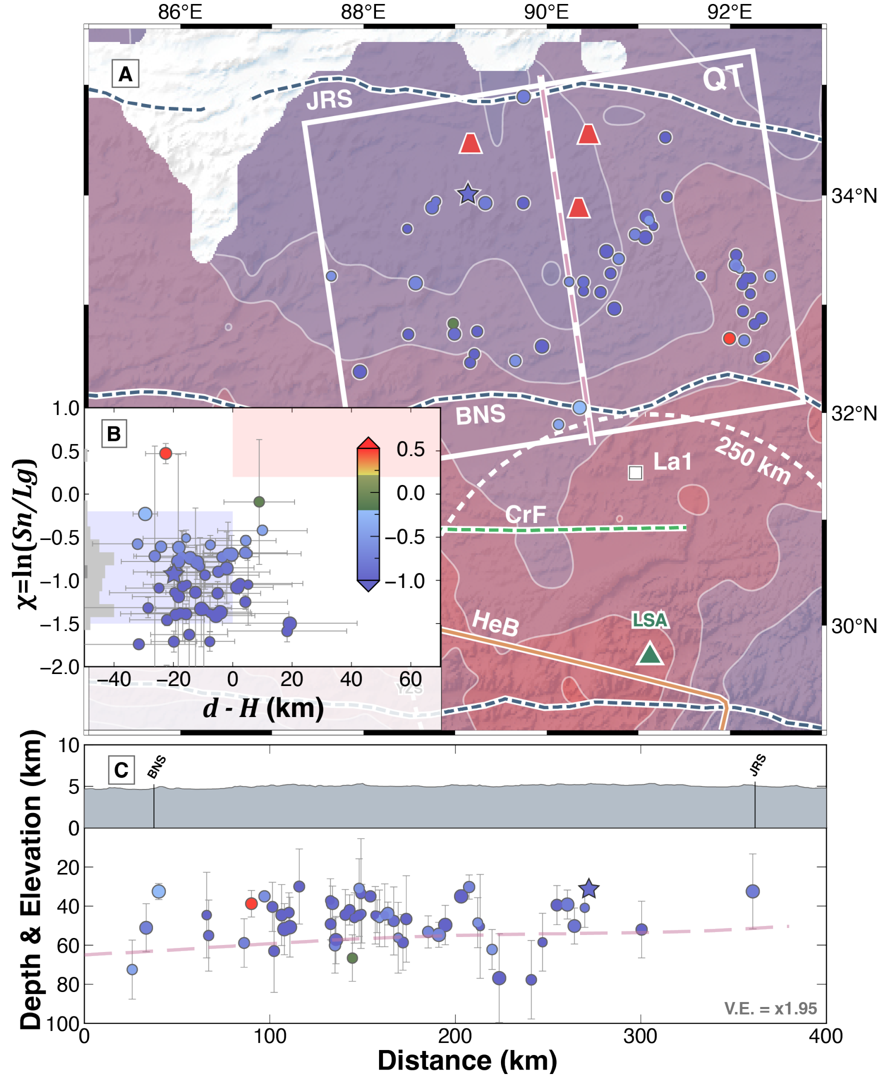

Fig. S11. (A) Sn/Lg ratio spatial distribution in Qiangtang (QT). Legends as in Fig. S4 (A). Red trapezoids: Pliocene-Quaternary volcanic lavas (Wang et al., 2016). **(B) $\ln(Sn/Lg)$ vs $d-H$ plots for QT.** White square (La1): earthquake (1998 Dec. 14, m_b4.1) studied by Langin et al. (2003). Legends the same with Fig. 5 (b). **(C) Cross-sectional view of the Sn/Lg ratios along the profile direction in (A).** Legends as in Fig. 5C.

Supplementary References:

Ammon, C.J., Velasco, A.A., Lay, T., Wallace, T.C., 2021. Chapter 19 - Imaging seismic-sources, in: Ammon, C.J., Velasco, A.A., Lay, T., Wallace, T.C. (Eds.), Foundations of Modern Global Seismology (2nd Edition). Academic Press, pp. 515–535. https://doi.org/10.1016/B978-0-12-815679-7.00027-6

Fan, G.-W., Lay, T., 2003. Strong Lg wave attenuation in the Northern and Eastern Tibetan Plateau measured by a two-station/two-event stacking method. Geophys. Res. Lett. 30, 1530. https://doi.org/10.1029/2002GL016211

Jiang M., Zhou S., Tong X., Liang X., Chen Y., 2009. Accurate depth determination of deep earthquake in southern Tibet and its geodynamic implication. Chin. J. Geophys. 52, 2237–2244. https://doi.org/10.3969/j.issn.0001-5733.2009.09.007

Kennett, B.L.N., 1986. Lg waves and structural boundaries. Bull. Seismol. Soc. Am. 76, 1133–1141. https://doi.org/10.1785/BSSA0760041133

Langin, W.R., Brown, L.D., Sandvol, E.A., 2003. Seismicity of central Tibet from project INDEPTH III seismic recordings. Bull. Seismol. Soc. Am. 93, 2146–2159. https://doi.org/10.1785/0120030004

McNamara, D.E., Owens, T.J., Walter, W.R., 1995. Observations of regional phase propagation across the Tibetan Plateau. J. Geophys. Res. Solid Earth 100, 22215–22229. https://doi.org/10.1029/95JB01863

Michailos, K., Carpenter, N.S., Hetényi, G., 2021. Spatio-temporal evolution of intermediate-depth seismicity beneath the Himalayas: implications for metamorphism and tectonics. Front. Earth Sci. 9. https://doi.org/10.3389/feart.2021.742700

Monsalve, G., Sheehan, A., Schulte-Pelkum, V., Rajaure, S., Pandey, M.R., Wu, F., 2006. Seismicity and one-dimensional velocity structure of the Himalayan collision zone: Earthquakes in the crust and upper mantle. J. Geophys. Res. Solid Earth 111. https://doi.org/10.1029/2005JB004062

Mousavi, S.M., Cramer, C.H., Langston, C.A., 2014. Average QLg, QSn, and observation of Lg blockage in the continental margin of Nova Scotia. J. Geophys. Res. Solid Earth 119, 7722–7744. https://doi.org/10.1002/2014JB011237

Storchak, D.A., Di Giacomo, D., Bondar, I., Engdahl, E.R., Harris, J., Lee, W.H.K., Villasenor, A., Bormann, P., 2013. Public Release of the ISC-GEM Global Instrumental Earthquake Catalogue (1900-2009). Seismol. Res. Lett. 84, 810–815. https://doi.org/10.1785/0220130034

Taylor, S.R., Yang, X., Phillips, W.S., 2003. Bayesian Lg Attenuation Tomography Applied to Eastern Asia. Bull. Seismol. Soc. Am. 93, 795–803. https://doi.org/10.1785/0120020010

Wang, Q., Hawkesworth, C.J., Wyman, D., Chung, S.-L., Wu, F.-Y., Li, X.-H., Li, Z.-X., Gou, G.-N., Zhang, X.-Z., Tang, G.-J., Dan, W., Ma, L., Dong, Y.-H., 2016. Pliocene-Quaternary crustal melting in central and northern Tibet and insights into crustal flow. Nat. Commun. 7, 11888. https://doi.org/10.1038/ncomms11888

Wang, S., Klemperer, S.L., 2021. Love-wave normal modes discriminate between upper-mantle and crustal earthquakes: Simulation and demonstration in Tibet. Earth Planet. Sci. Lett. 571, 117089. https://doi.org/10.1016/j.epsl.2021.117089

Wittlinger, G., Farra, V., Hetényi, G., Vergne, J., Nábělek, J., 2009. Seismic velocities in Southern Tibet lower crust: a receiver function approach for eclogite detection. Geophys. J. Int. 177, 1037–1049. https://doi.org/10.1111/j.1365-246X.2008.04084.x

Xia, B., Artemieva, I.M., Thybo, H., Klemperer, S.L., 2023. Strong variability in the thermal structure of Tibetan lithosphere. J. Geophys. Res. Solid Earth 128, e2022JB026213. https://doi.org/10.1029/2022JB026213

Yang, X., 2002. A numerical investigation of Lg geometrical spreading. Bull. Seismol. Soc. Am. 92, 3067–3079. https://doi.org/10.1785/0120020046

Zhang, Z., Wang, Y., Houseman, G.A., Xu, T., Wu, Z., Yuan, X., Chen, Y., Tian, X., Bai, Z., Teng, J., 2014. The Moho beneath western Tibet: Shear zones and eclogitization in the lower crust. Earth Planet. Sci. Lett. 408, 370–377. https://doi.org/10.1016/j.epsl.2014.10.022

Zhao, G., Liu, J., Chen, B., Kaban, Mikhail.K., Zheng, X., 2020. Moho beneath Tibet based on a joint analysis of gravity and seismic data. Geochem. Geophys. Geosystems 21, e2019GC008849. https://doi.org/10.1029/2019GC008849

Zhao, L.-S., Helmberger, D.V., Harkrider, D.G., 1991. Shear-velocity structure of the crust and upper mantle beneath the Tibetan Plateau and southeastern China. Geophys. J. Int. 105, 713–730. https://doi.org/10.1111/j.1365-246X.1991.tb00807.x

Date	Mag.	Lon.	Lat.	Dep.(km)	ln{Sn/Lg} (RMS)	ln{Sn/Lg} (maxAmpl)	d-H(km)
2022-04-06	4.2	75.96	37.63	115.8	1.55	1.95	53.1
2008-09-13	3.6	75.59	37.79	121.7[9]	1.41	1.55	53.4
2016-09-12	3.5	75.77	38.16	102.9[9]	1.31	1.63	40.7
2009-02-15	3.4	75.85	37.65	121.3[9]	1.21	1.85	56.7
2014-02-06	4.5	75.66	37.96	116.7	1.20	1.68	51.1
2016-09-13	3.7	75.96	37.76	106.6[9]	1.20	1.71	44.7
2017-05-11	3.6	75.52	38.15	95.6[9]	1.19	1.77	30.4
2019-04-13	4.0	75.12	37.68	100.7	1.15	1.45	26.9
2019-12-18	4.0	75.91	37.80	125.0	1.11	1.36	62.1
2016-05-31	4.7	77.89	36.56	105.1[9]	1.10	1.48	47.3
2015-09-05	3.8	75.98	37.84	102.5[9]	1.10	1.46	41.1
2014-08-30	4.3	75.91	37.63	115.3	1.02	1.56	51.7
2016-04-24	3.5	76.00	37.70	107.9[9]	1.02	1.69	46.4
2008-01-14	4.1	75.95	37.69	124.5	0.99	1.07	62.0
2016-08-19	3.4	75.82	37.69	96.3[9]	0.97	1.55	31.2
2012-01-03	4.6	77.35	35.78	62.9	0.97	1.34	-2.4
2015-10-29	3.3	75.22	38.22	109.0[9]	0.96	1.22	41.0
2015-10-23	4.0	77.90	36.33	88.6	0.95	1.15	29.0
2021-04-27	4.5	75.67	37.55	99.4	0.94	1.25	31.8
2008-09-30	4.7	76.10	37.43	122.5	0.94	1.07	60.1
2013-10-06	4.1	75.79	37.62	122.4	0.93	0.75	56.6
2007-04-11	4.4	78.31	35.87	87.9	0.92	1.00	26.1
2008-05-30	3.6	78.50	35.81	98.6	0.92	1.20	37.6
2009-10-08	4.5	75.09	38.21	102.6[9]	0.88	0.93	33.7
2009-12-06	5.2	77.35	35.78	91.0[2]	0.85	0.71	25.8
2022-04-24	4.3	76.82	36.78	94.9	0.84	1.43	38.0
2010-05-27	3.2	75.22	38.27	118.9[9]	0.82	1.33	51.8
2013-06-09	4.2	77.14	36.74	95.1	0.76	0.83	38.9
2014-07-08	4.5	77.27	36.58	97.6	0.76	0.97	38.6
2016-07-07	4.0	75.71	37.96	100.6[9]	0.75	0.84	35.6
2015-09-06	4.1	78.32	35.95	72.9	0.75	1.01	11.8
2007-10-14	4.3	75.93	37.61	116.7	0.74	0.83	53.3
2012-08-06	4.6	77.71	35.80	72.7	0.72	0.29	8.0
2009-03-08	4.6	78.02	36.10	106.9	0.72	1.02	45.6
2007-02-19	4.5	75.95	37.66	109.7	0.70	0.70	47.1
2022-04-22	4.3	77.02	36.72	110.9	0.67	0.62	57.2
2011-03-23	5.1	76.49	36.28	87.0[2]	0.65	0.92	25.0
2016-11-11	4.0	77.12	36.81	103.6[9]	0.65	0.92	48.2
2016-08-28	4.6	77.01	36.83	102.2[9]	0.64	1.48	47.9
2017-02-24	3.3	75.53	38.21	87.0[9]	0.64	1.00	22.5
2016-12-14	3.8	77.03	36.90	99.7[9]	0.60	0.68	44.1
2015-08-31	4.3	77.45	35.83	76.7	0.59	1.09	12.1
2009-10-22	3.9	75.42	38.26	55.8[9]	0.58	0.48	-9.4
2019-10-22	4.4	78.29	36.15	35.5	0.58	1.10	-24.8
2010-06-07	3.4	75.47	38.25	101.2[9]	0.56	0.86	36.4
2017-04-02	3.3	77.23	36.80	110.1[9]	0.55	0.47	52.9
2016-04-09	4.0	76.20	37.27	92.0[9]	0.55	0.72	30.0
2020-09-22	4.1	77.83	35.70	62.2	0.52	0.78	-3.1
2017-04-25	4.4	75.61	37.45	68.7[9]	0.51	0.82	0.5
2018-09-11	4.4	76.28	36.34	79.4	0.51	0.77	13.9
2012-02-21	4.5	76.83	36.68	78.5	0.50	0.51	21.1
2016-05-27	4.1	77.91	36.20	84.8	0.48	0.56	24.3
2021-02-04	4.5	76.83	36.78	93.7	0.47	0.95	36.9
2013-10-20	5.0	77.26	35.74	89.9[*]	0.45	0.57	24.2
2008-08-22	4.6	76.94	36.67	96.8	0.42	0.60	41.0
2007-07-30	4.8	76.78	36.35	83.9	0.42	0.26	23.2
2010-01-25	3.2	75.23	37.88	94.2[9]	0.40	0.78	21.4
2015-05-07	4.1	76.86	36.76	96.8	0.40	0.89	41.1
2015-09-15	3.6	77.03	36.84	97.9[9]	0.40	0.42	43.4
2017-05-01	3.7	76.98	36.82	87.7[9]	0.40	0.22	33.3
2017-12-06	5.2	77.45	35.74	118.1[*]	0.39	0.68	52.7
2010-04-08	4.4	77.24	36.43	88.1	0.37	0.35	28.2
2007-10-24	4.2	77.43	35.65	81.9	0.37	0.57	15.6
2017-04-18	4.6	76.42	33.96	51.3	0.36	0.39	-12.9
2014-11-09	4.0	76.25	37.00	95.7	0.35	0.70	33.2
2010-06-03	4.6	76.84	36.70	99.0[2]	0.33	0.67	42.1
2015-12-10	3.7	76.95	36.75	95.9[9]	0.33	0.44	42.2
2014-10-21	4.0	78.19	36.09	54.4	0.32	0.43	-6.5
2012-08-08	4.3	77.54	35.71	81.2	0.29	0.49	15.6
2016-04-11	3.6	76.96	36.76	99.9[9]	0.29	0.04	46.4
2010-04-23	4.6	76.92	35.99	102.1	0.28	0.39	39.0
2019-12-08	4.5	78.01	36.27	49.9	0.26	0.43	-9.7
2010-02-09	3.3	75.73	38.29	158.6[9]	0.25	0.55	97.1
2008-05-29	3.5	76.09	32.59	45.9	0.25	0.43	-8.7
2011-09-27	5.0	76.70	36.59	81.7	0.23	0.18	22.1
2009-05-21	5.1	77.62	36.28	93.0[2]	0.23	0.69	32.4
2008-07-17	3.2	76.81	36.67	80.5	0.20	0.13	22.8
2017-01-09	4.1	77.83	35.68	82.1	0.20	0.09	16.6
2016-02-21	4.5	78.10	36.13	35.7	0.18	0.55	-25.1
2010-03-13	4.7	75.71	34.29	56.6	0.14	0.28	-14.1
2008-03-12	3.6	78.26	36.55	80.8	0.12	0.43	23.6
2007-06-17	3.8	78.23	33.01	54.7	0.12	0.33	-8.1
2015-10-08	4.2	76.97	31.60	36.0	0.10	0.13	-17.6
2017-05-19	4.5	76.14	33.02	43.0	0.07	0.18	-14.4
2017-03-31	3.6	76.97	36.77	99.6[9]	0.04	0.31	46.1
2014-11-18	4.3	76.06	32.94	60.8	-0.01	0.20	4.0
2017-05-20	4.2	76.30	32.87	35.4	-0.12	0.00	-22.2
2015-09-04	3.5	78.42	37.15	39.4	-0.15	-0.22	-14.8
2013-12-18	4.2	78.64	37.43	39.3	-0.16	-0.32	-15.0
2020-06-30	4.7	75.87	33.12	43.9	-0.17	0.24	-13.0
2008-11-05	4.5	76.96	38.21	67.5[9]	-0.18	0.19	18.2
2009-01-31	3.9	76.56	32.53	36.1	-0.18	-0.14	-20.6
2008-06-15	4.3	76.37	32.97	36.3	-0.19	-0.31	-20.9
2008-09-08	3.4	76.94	36.00	54.7	-0.21	0.02	-8.3
2011-04-02	4.7	76.70	36.68	95.0[2]	-0.21	0.01	35.8
2016-05-24	4.1	76.09	33.08	35.0	-0.22	-0.09	-23.4
2008-04-05	3.5	75.92	33.24	65.2	-0.23	-0.19	6.3
2014-06-17	4.2	76.45	32.33	33.5	-0.24	0.02	-21.3
2012-06-27	4.1	79.36	36.44	36.7	-0.24	-0.21	-14.9
2018-05-06	4.1	76.12	32.88	41.6	-0.25	-0.32	-15.1
2020-06-30	4.2	75.93	33.19	46.8	-0.27	0.21	-11.8
2018-03-15	4.5	76.10	33.03	39.8	-0.29	-0.29	-17.9
2007-11-25	3.9	77.19	37.33	48.5	-0.30	-0.43	-5.8
2008-07-05	3.5	75.94	33.47	56.6	-0.30	-0.01	-5.1
2013-06-04	5.2	76.54	32.58	30.0[+]	-0.31	-0.15	-26.7
2015-09-03	4.2	78.06	37.53	41.9	-0.31	-0.16	-11.3
2016-02-09	4.2	76.08	32.99	40.2	-0.32	-0.06	-17.0
2012-03-07	4.3	78.11	32.03	55.6	-0.32	-0.34	3.6
2012-09-04	4.6	78.79	36.89	41.1	-0.32	-0.38	-12.3
2007-05-01	3.9	78.60	36.87	134.8	-0.34	-0.48	81.8
2012-09-09	4.1	78.91	37.08	51.8	-0.34	-0.21	-2.6
2014-04-19	4.1	76.24	34.10	34.0	-0.35	-0.43	-31.6
2008-11-05	3.6	77.96	35.29	39.2	-0.35	-0.36	-33.1
2016-02-04	4.3	76.04	32.85	58.7	-0.35	-0.31	2.8
2014-04-18	4.2	78.69	37.46	45.2	-0.36	-0.47	-9.0
2013-08-05	4.1	75.93	33.33	50.5	-0.37	-0.18	-9.7
2013-06-08	4.2	77.17	36.21	61.9	-0.38	-0.20	0.3
2017-05-29	4.5	75.93	33.30	35.9	-0.39	-0.29	-23.8
2008-10-30	3.5	76.52	36.20	35.3	-0.42	-0.37	-26.7
2007-08-14	4.3	77.08	37.93	49.5	-0.43	-0.53	-0.9
2008-05-10	4.4	76.12	33.06	44.7	-0.44	-0.48	-13.4
2010-03-23	4.2	75.15	33.78	39.8	-0.44	-0.55	-17.4
2011-07-28	4.5	76.00	33.32	33.3	-0.44	-0.49	-27.5
2013-04-17	4.0	76.66	33.25	42.2	-0.45	-0.45	-16.0
2015-07-06	4.2	77.98	37.62	44.1	-0.46	-0.63	-8.6
2019-01-10	4.6	78.24	34.36	34.5	-0.46	-0.53	-34.9
2020-10-08	4.1	75.47	35.08	51.4	-0.47	-0.11	-17.3
2013-08-05	4.3	76.02	33.46	46.8	-0.48	-0.50	-15.4
2017-08-16	4.4	76.24	32.87	44.8	-0.49	-0.64	-12.7
2016-03-17	4.1	78.07	34.04	31.9	-0.49	-0.43	-35.1
2013-11-06	4.4	76.13	31.73	41.1	-0.50	-0.77	-12.8
2013-10-26	4.5	75.94	33.10	41.6	-0.53	-0.38	-16.1
2008-08-04	4.1	75.89	35.26	43.7	-0.54	-0.50	-28.7
2008-02-29	3.8	75.01	33.75	51.1	-0.57	-0.65	-4.8
2015-02-15	4.7	76.20	34.43	48.0	-0.58	-0.46	-23.5
2016-08-01	4.5	76.99	31.31	35.1	-0.59	-0.33	-15.0
2019-09-09	4.9	75.87	32.92	30.1[*]	-0.60	-0.38	-24.7
2022-01-04	4.3	76.07	33.03	40.1	-0.60	-0.77	-17.7
2016-10-04	4.3	75.69	33.75	35.0	-0.61	-0.53	-25.4
2015-03-10	4.1	76.82	35.65	39.2	-0.62	-0.54	-26.6
2012-05-21	4.8	77.11	37.95	31.4	-0.63	-0.83	-18.6
2013-08-18	4.8	75.87	33.22	44.8	-0.64	-0.29	-13.3
2013-08-29	4.4	76.27	31.48	47.0[4]	-0.65	-0.96	-5.6
2008-02-23	3.9	75.90	36.84	80.7	-0.66	-0.71	15.0
2008-03-05	4.2	75.03	33.77	39.4	-0.66	-0.91	-16.8
2015-09-24	4.7	78.12	37.57	42.8	-0.67	-0.56	-10.4
2008-03-08	3.8	76.57	33.31	37.2	-0.67	-0.83	-21.8
2013-07-09	4.0	78.33	32.85	36.9	-0.68	-0.73	-24.4
2007-02-21	4.1	77.75	31.37	36.6	-0.68	-0.80	-11.4
2013-07-09	4.1	78.17	32.74	38.0[4]	-0.69	-0.60	-21.4
2013-05-14	4.3	75.74	33.12	35.7	-0.69	-0.70	-19.5
2014-10-10	4.0	79.15	34.33	45.3	-0.71	-0.75	-23.3
2012-06-03	4.3	79.72	35.83	45.2	-0.75	-0.51	-11.4
2013-10-21	4.5	77.00	35.29	35.0	-0.77	-0.41	-38.5
2015-07-14	4.5	77.82	37.75	43.1	-0.78	-0.77	-8.8
2011-06-21	4.5	75.49	35.15	47.2	-0.80	-1.01	-21.7
2012-07-11	4.1	76.53	35.54	65.4	-0.80	-0.58	-6.6
2010-08-14	4.1	78.74	34.12	67.9	-0.81	-0.87	-0.6
2018-09-11	4.4	76.21	33.64	35.0	-0.82	-0.80	-28.3
2017-03-19	4.4	77.89	37.20	45.2	-0.83	-0.95	-8.5
2007-11-13	4.9	80.05	36.67	43.1	-0.84	-0.67	-8.8
2012-05-01	4.0	76.50	35.63	79.6	-0.85	-0.81	9.8
2013-06-05	4.0	76.29	32.91	40.0[4]	-0.85	-0.90	-17.3
2011-09-24	4.2	75.25	34.04	61.0	-0.87	-0.68	-0.7
2012-07-26	4.4	76.11	33.47	56.2	-0.87	-1.06	-6.3
2013-11-15	4.2	77.75	34.54	30.8	-0.88	-0.90	-41.5
2008-12-19	4.0	76.22	36.20	41.8	-0.89	-0.98	-24.8
2013-11-24	4.0	77.03	35.35	79.6	-0.91	-0.91	7.8
2012-07-11	4.2	76.51	35.62	68.1	-0.91	-0.88	-1.7
2017-10-25	4.5	75.33	37.24	41.1	-0.92	-0.84	-29.9
2016-03-17	3.9	78.48	37.33	41.8	-0.94	-0.92	-12.4
2014-09-09	4.4	76.08	36.48	44.6	-0.96	-0.93	-19.4
2014-10-11	4.5	79.20	34.39	35.0	-0.99	-0.97	-33.7
2009-01-27	4.0	76.39	36.18	36.9	-1.00	-0.74	-27.1
2013-05-14	4.7	75.73	33.10	61.7	-1.00	-0.66	6.7
2017-10-19	4.6	76.26	33.51	32.1	-1.00	-0.78	-30.8
2010-06-02	4.4	75.98	36.08	65.5	-1.01	-0.67	-2.1
2014-11-21	4.3	79.00	34.40	36.7	-1.03	-0.89	-32.1
2013-09-19	4.2	75.43	37.38	70.0	-1.06	-1.15	-0.1
2011-01-10	4.7	75.28	37.51	42.9	-1.07	-1.21	-29.3
2019-05-31	4.5	75.85	36.87	35.0	-1.08	-1.04	-31.2
2017-12-10	4.6	78.57	34.32	35.5	-1.09	-0.85	-33.5
2022-06-13	4.3	75.20	37.83	61.3	-1.09	-1.11	-12.1
2018-06-06	4.3	75.75	37.60	54.7	-1.11	-1.05	-11.9
2014-12-24	4.1	75.79	36.23	74.1	-1.11	-0.91	9.3
2014-11-17	4.4	77.12	35.36	35.0	-1.15	-1.09	-36.6
2007-12-26	4.0	76.65	35.22	74.2	-1.18	-0.98	-0.1
2015-09-17	4.6	77.97	37.68	41.8	-1.26	-0.96	-10.7
2015-07-14	4.5	78.13	37.45	31.9	-1.29	-1.20	-21.7
2021-04-04	4.2	75.73	36.77	74.7	-1.31	-0.73	7.7
2015-12-20	4.3	78.03	37.60	40.5	-1.32	-1.20	-12.4
2013-11-16	4.3	77.11	35.34	58.8	-1.33	-1.20	-13.4
2013-11-11	4.0	77.10	35.34	56.7	-1.34	-1.20	-15.3
2011-10-16	4.5	76.38	35.68	46.2	-1.67	-1.73	-22.0
2013-12-09	4.0	76.92	35.49	69.1	-1.75	-1.74	1.4
2013-10-24	4.2	77.14	35.30	51.4	-1.88	-1.53	-21.9

Table SA. Source parameters and waveforms of WT earthquakes, and their ln(Sn/Lg) calculated using RMS and maximum amplitude ratios. Waveforms aligned by P arrival (set to be 60 s here).
Depths listed are from the PDE catalog except where marked with a superscript: 1: Alvizuri and Hetényi, (2019); 2: Craig et al., (2012); 3: Baur, (2007); 4: Parija et al., (2018); 5: Michailos et al., (2021); 6: Diehl et al., (2017); 7: Monsalve et al., (2006); 8: Jiang et al., (2009); 9: Bloch et al., (2021); *: GCMT; +: ISC-GEM.

Date	Mag.	Lon.	Lat.	Dep.(km)	ln{Sn/Lg} (RMS)	ln{Sn/Lg} (maxAmpl)	d-H(km)
2005-12-25	4.0	86.09	28.58	54.9	1.14	1.14	5.9
2015-04-02	4.6	86.33	28.70	57.3	1.10	1.11	5.8
2010-10-18	4.0	85.65	28.49	43.0	1.03	1.02	-2.5
2012-11-05	4.5	86.19	28.45	77.8	0.99	0.97	30.1
2003-06-23	4.2	88.17	27.79	80.3	0.96	1.30	30.0
2002-05-08	3.7	86.49	28.58	75.9[1]	0.94	1.39	24.8
2008-06-22	3.7	85.68	28.43	66.1	0.94	0.88	21.3
2013-08-30	4.9	85.90	28.16	54.7	0.93	0.80	10.7
2019-06-17	4.6	87.17	28.42	84.8	0.88	1.00	31.4
2013-08-30	4.1	85.75	28.07	45.8	0.88	0.82	3.1
2010-02-26	5.1	86.77	28.41	84.5*	0.83	0.62	36.1
2003-01-22	4.2	86.96	28.38	64.7[5]	0.80	1.17	13.7
2010-10-17	5.2	85.68	28.62	52.9+	0.79	0.98	4.9
2002-06-24	3.5	88.19	27.78	68.9[5]	0.76	1.09	18.6
2003-02-25	3.6	86.95	28.48	62.7[5]	0.75	0.69	10.2
2002-03-07	4.2	84.83	29.56	77.0[3]	0.72	0.91	15.6
2007-04-06	3.7	86.46	28.44	95.2	0.70	0.69	46.0
2005-10-30	3.9	87.99	27.85	85.5	0.69	0.96	35.4
2002-05-08	3.5	87.93	27.89	70.0[5]	0.69	0.57	19.6
2008-09-19	4.0	86.67	28.58	69.2	0.68	1.24	18.3
2012-08-09	4.7	86.74	28.46	70.2	0.68	0.96	21.4
2002-01-05	3.3	87.69	28.16	69.1[5]	0.64	0.97	16.6
2013-08-04	4.3	87.14	28.27	35.5	0.62	0.76	-15.6
2002-07-16	3.8	87.83	27.86	65.0[3]	0.62	0.68	15.1
2002-07-02	3.9	84.78	27.11	70.0[3]	0.62	0.79	26.7
2014-11-19	3.9	87.95	28.25	96.0[6]	0.61	0.40	41.0
2014-08-22	4.4	87.98	28.16	96.0[6]	0.60	0.77	42.3
2014-12-26	4.9	87.35	28.53	57.3	0.59	0.84	1.8
2002-10-29	3.9	87.74	28.12	72.0[5]	0.58	0.52	19.0
2014-07-28	3.5	87.95	28.01	44.0[6]	0.56	0.43	-7.5
2000-09-06	3.7	86.35	28.56	105.4	0.56	0.48	55.5
2002-12-26	3.6	86.52	28.66	70.0[5]	0.54	0.76	18.0
2021-01-11	4.1	87.79	28.03	35.0	0.54	0.52	-16.9
2021-02-09	4.3	87.86	28.03	35.0	0.47	0.43	-16.9
2002-06-28	3.9	87.40	27.75	60.1[5]	0.46	0.23	13.1
2013-04-06	4.6	88.05	30.04	35.0	0.40	0.03	-37.7
2013-07-15	4.7	87.60	28.38	52.5	0.40	0.60	-2.0
2007-11-07	3.7	87.04	28.02	75.8	0.39	0.64	31.4
2019-11-27	4.4	87.87	28.17	64.7	0.34	0.17	11.0
2004-02-27	4.6	87.66	28.13	92.0[3]	0.27	0.33	40.1
2002-12-12	3.7	87.97	27.94	65.7[5]	0.26	0.37	14.9
2002-10-16	3.3	86.34	26.89	49.6[5]	0.26	0.58	4.2
2016-05-09	4.2	85.76	28.21	39.3	0.24	0.21	-3.5
1999-08-01	5.2	86.73	28.44	40.2	0.19	0.03	-8.4
2007-04-17	4.1	87.76	28.26	72.2	0.19	-0.10	17.7
2008-04-01	3.9	87.01	28.52	69.9	0.14	0.18	16.0
2007-02-06	4.3	87.62	27.91	58.9	0.13	0.29	9.3
2011-12-14	4.0	87.96	27.50	47.5	0.13	0.35	-0.2
2002-12-23	4.0	87.71	28.12	68.8[5]	0.10	0.17	16.4
2004-07-08	4.2	88.00	29.84	32.6	0.10	-0.14	-39.0
2013-04-19	4.2	87.85	27.33	47.1	0.02	-0.12	0.6
2013-12-08	4.0	87.60	27.73	44.8	0.00	-0.16	-3.1
2012-03-27	5.0	87.76	26.09	31.0[2]	-0.02	0.20	-11.6
2013-09-20	3.2	88.30	27.66	40.9[6]	-0.02	-0.22	-8.7
2002-05-09	4.6	87.84	29.83	33.6	-0.02	-0.23	-37.7
2014-06-02	3.5	89.13	27.14	31.7[6]	-0.03	-0.14	-22.2
2003-11-30	3.5	88.42	29.01	86.3	-0.04	-0.17	20.5
2016-04-19	4.3	87.84	28.34	55.9	-0.05	-0.14	-0.1
2005-03-26	4.8	87.84	28.21	76.0[2]	-0.06	0.19	21.9
2004-06-26	4.2	88.05	30.04	56.8	-0.13	-0.30	-15.8
2018-06-20	4.4	87.81	27.15	52.9	-0.14	-0.29	8.2
2014-07-04	4.8	88.01	27.87	95.9[6]	-0.14	-0.28	45.6
2002-07-18	3.7	87.93	28.20	78.0[3]	-0.15	0.01	23.8
2002-01-31	4.3	87.90	29.90	39.6	-0.18	-0.05	-32.1
2002-03-21	4.2	88.05	29.77	53.4	-0.20	0.16	-17.6
2006-04-11	3.5	87.41	28.14	54.3	-0.22	-0.31	4.7
2014-03-18	4.1	87.95	28.34	41.1[6]	-0.30	-0.12	-15.3
2018-06-20	4.4	87.50	26.96	38.3	-0.34	-0.38	-8.3
2012-05-30	4.3	87.97	27.33	35.4	-0.36	-0.70	-10.3
2012-06-11	4.5	88.13	27.31	51.5	-0.40	-0.45	5.2
2013-02-09	3.5	89.15	26.99	32.4[6]	-0.40	-0.40	-21.7
2006-02-03	4.7	86.70	26.94	30.9*	-0.40	-0.18	-15.7
2011-05-24	4.5	85.39	30.04	41.4	-0.49	-0.57	-27.1
2011-08-11	4.2	86.81	30.09	37.9	-0.49	-0.56	-30.5
2013-06-27	4.2	89.25	27.20	38.1[6]	-0.49	-0.63	-16.7
2018-05-08	4.0	87.43	28.06	32.6	-0.50	-0.64	-16.2
2004-08-25	4.4	86.07	30.21	47.7	-0.50	-0.49	-20.9
2012-09-18	4.6	88.64	27.33	42.2	-0.51	-0.29	-8.6
2007-09-01	4.0	87.87	27.85	73.1	-0.51	-0.45	23.2
2005-05-11	4.6	85.17	30.60	37.5	-0.53	-0.38	-30.6
2005-06-14	4.6	87.92	27.20	44.4	-0.56	-0.76	-0.2
2009-11-07	4.1	89.18	26.92	41.1	-0.56	-0.69	-13.0
2014-05-02	3.9	88.38	27.56	33.0[6]	-0.57	-0.53	-17.0
2011-02-10	4.0	88.21	27.22	46.2	-0.61	-1.16	-0.3
2014-07-19	3.8	88.81	27.42	48.3[6]	-0.62	-1.15	-4.0
2016-11-27	5.2	86.53	27.35	35.4*	-0.62	-0.54	-9.0
2005-04-06	3.6	86.35	30.44	66.9	-0.63	-0.31	-1.4
2005-05-27	3.5	87.21	26.14	57.7	-0.64	-0.68	13.4
2018-06-17	4.4	88.47	27.42	49.8	-0.66	-0.69	-0.9
2010-07-10	4.6	86.98	29.32	42.3	-0.68	-0.74	-20.2
2001-06-13	4.5	85.76	31.38	72.4	-0.69	-0.96	6.3
2011-09-18	6.9	88.35	27.44	46.0*	-0.70	-0.72	-2.7
2007-05-16	4.0	87.85	27.29	31.7	-0.71	-0.84	-14.3
2001-06-13	4.1	85.75	31.44	54.3	-0.71	-0.32	-11.5
2015-10-10	4.3	88.80	27.25	48.2	-0.71	-0.77	-3.2
2015-08-01	4.4	87.66	28.75	34.3	-0.72	-0.87	-25.3
2011-09-18	4.8	88.58	27.52	40.1	-0.73	-0.88	-11.9
2014-12-18	5.0	86.56	27.46	30.3*	-0.76	-0.63	-13.8
2007-08-03	4.3	86.93	27.20	64.0	-0.78	-0.48	17.3
2007-08-15	4.0	85.35	31.28	71.0	-0.79	-0.77	4.1
2008-12-25	4.8	88.63	27.24	49.2	-0.82	-0.91	-0.9
2006-10-28	3.5	87.98	31.15	63.6	-0.82	-0.60	-5.7
2002-12-30	4.2	86.27	30.72	51.3	-0.83	-0.45	-17.4
2015-05-25	4.3	87.24	28.57	42.4	-0.87	-0.93	-13.0
2006-01-20	4.6	85.01	31.44	37.3	-0.89	-0.83	-29.7
2002-08-22	4.5	88.09	29.82	38.5	-0.94	-1.79	-32.8
2014-10-29	3.9	88.82	27.21	36.2[6]	-1.00	-1.14	-15.3
2004-01-06	4.6	86.04	30.54	46.2	-1.18	-0.95	-22.5
2016-10-01	4.2	88.10	30.98	34.6	-1.22	-1.14	-36.2
2005-08-28	4.8	87.42	27.64	38.8	-1.24	-1.24	-8.2
2005-08-20	4.9	88.09	31.08	54.0	-1.69	-1.66	-16.0
2002-11-05	4.8	86.58	31.01	41.3	-1.82	-1.89	-27.2
2002-10-11	4.7	88.23	31.23	60.9	-2.20	-2.25	-8.0

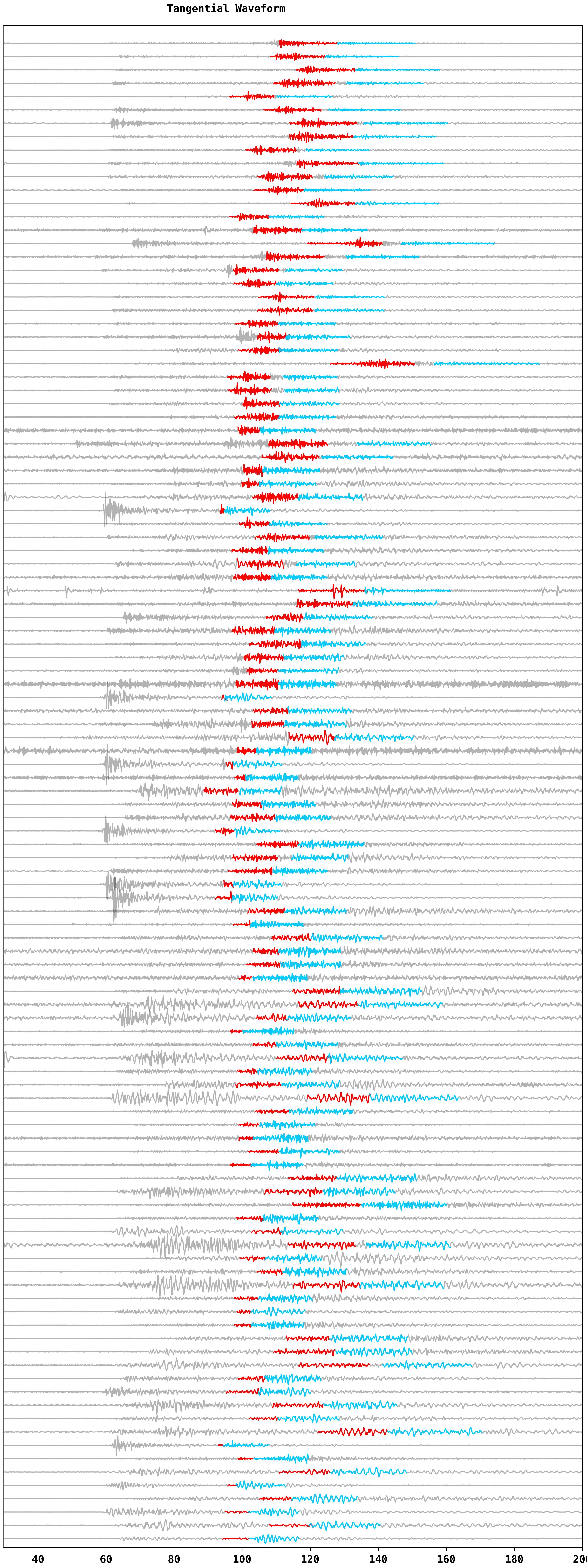

Table SB. Source parameters and waveforms of ST earthquakes, and their ln(Sn/Lg) calculated using RMS and maximum amplitude ratios. Waveforms aligned by P arrival (set to be 60 s here).
Depths listed are from the PDE catalog except where marked with a superscript: 1: Alvizuri and Hetényi, (2019); 2: Craig et al., (2012); 3: Baur, (2007); 4: Parija et al., (2018); 5: Michailos et al., (2021); 6: Diehl et al., (2017); 7: Monsalve et al., (2006); 8: Jiang et al., (2009); 9: Bloch et al., (2021); *: GCMT; +: ISC-GEM.

Date	Mag.	Lon.	Lat.	Dep.(km)	ln{Sn/Lg} (RMS)	ln{Sn/Lg} (maxAmpl)	d-H(km)
2011-05-24	4.1	92.31	25.10	47.0	0.84	1.05	6.7
2008-04-17	4.6	92.24	26.07	43.8	0.80	0.82	9.9
2005-03-11	4.4	90.49	27.34	52.6	0.66	0.81	-1.5
2015-11-25	4.7	92.97	26.41	54.5	0.65	0.75	23.2
2018-06-11	5.1	92.59	26.28	50.7[+]	0.62	0.65	16.6
2015-09-05	4.2	92.83	26.19	47.2	0.61	0.73	15.7
2008-05-29	4.5	91.79	26.31	45.5	0.60	0.38	6.8
2013-12-29	4.0	92.93	26.40	40.8[6]	0.60	0.74	9.6
2015-02-01	4.2	93.36	26.42	45.2	0.60	0.82	3.9
2014-04-01	4.9	92.78	26.31	42.4[6]	0.58	0.23	10.1
2012-10-30	4.6	92.34	26.12	62.0	0.58	0.63	27.9
2014-10-30	3.7	92.78	26.46	44.4[6]	0.57	0.44	9.6
2014-05-29	4.5	93.24	26.42	34.2[6]	0.57	0.19	-7.3
2014-08-21	3.9	93.11	26.82	41.8[6]	0.54	0.31	-1.3
2013-07-28	3.6	93.05	26.24	35.6[6]	0.53	0.51	-5.2
2015-12-23	4.3	93.09	26.26	48.5	0.51	0.72	7.7
2012-09-06	4.5	91.21	25.45	45.1	0.49	0.20	9.8
2019-04-27	4.6	93.03	26.44	43.8	0.49	0.15	2.4
2019-11-13	4.7	93.31	26.17	51.2	0.48	0.59	10.5
2020-04-05	4.5	92.77	26.41	46.3	0.47	0.24	12.6
2008-08-27	4.2	92.01	27.15	50.7	0.43	0.46	6.1
2013-03-12	3.7	92.52	27.05	54.5[6]	0.38	-0.06	9.5
2003-04-08	4.6	93.19	26.13	40.5	0.36	0.42	-0.2
2016-10-06	4.3	92.77	26.44	56.8	0.35	0.42	22.5
2018-05-25	4.0	93.51	26.39	49.2	0.34	0.46	8.2
2017-03-21	4.4	92.56	25.38	34.7	0.34	0.49	-1.7
2002-01-12	3.9	91.89	27.34	59.5	0.33	0.09	13.9
2008-03-18	4.1	92.84	26.47	56.2	0.30	0.40	22.0
2014-02-10	3.8	92.85	26.38	42.3[6]	0.30	0.07	10.1
2004-07-13	4.2	92.78	26.21	71.5	0.29	0.63	39.6
2012-08-19	5.2	92.56	26.58	46.8[+]	0.28	0.49	4.6
2013-10-05	3.7	92.90	26.33	41.3[6]	0.26	0.11	10.5
2014-09-13	4.6	92.57	27.51	85.8[6]	0.25	0.54	37.9
2014-09-07	4.0	92.63	26.69	49.5[6]	0.25	-0.05	6.6
2008-04-03	4.3	92.98	26.31	45.6	0.24	0.43	15.2
2012-05-27	4.3	91.10	26.49	34.7	0.23	0.11	-8.6
2013-11-19	3.6	92.83	26.37	53.0[6]	0.22	0.30	20.8
2013-11-21	3.9	93.08	26.75	42.2[6]	0.20	-0.42	-0.5
2021-04-28	4.2	92.51	26.77	35.0	0.19	0.03	-8.5
2005-01-21	3.5	92.66	27.42	52.2	0.19	-0.02	4.9
2013-10-07	4.5	92.78	26.37	42.3[6]	0.18	0.02	9.3
2013-08-21	4.6	92.54	26.71	50.8[6]	0.17	0.08	7.7
2014-09-11	3.7	92.29	26.20	49.9[6]	0.17	0.06	14.9
2016-05-07	4.1	91.79	25.40	37.6	0.17	0.25	2.9
2014-06-14	5.2	92.64	26.91	46.7[6]	0.16	0.15	2.4
2005-01-21	3.7	92.72	27.44	55.9	0.16	0.18	8.2
2002-03-27	4.5	93.04	26.51	43.7	0.16	-0.04	2.0
2019-11-21	4.3	91.14	26.15	48.2	0.14	0.15	10.4
2014-05-29	4.2	92.04	25.25	54.0[6]	0.13	0.05	13.7
2013-07-12	4.1	91.96	26.27	46.3[6]	0.13	0.67	9.2
2007-03-14	3.9	91.33	27.29	58.4	0.12	0.42	13.9
2008-01-29	4.1	92.73	27.53	45.1	0.12	-0.11	-3.1
2005-06-24	4.3	93.14	26.48	54.2	0.12	0.10	12.5
2016-03-13	4.5	92.26	26.25	53.7	0.12	-0.24	18.2
2014-03-06	3.8	93.28	26.56	34.3[6]	0.12	-0.01	-7.7
2013-07-12	4.2	90.73	26.35	36.4[6]	0.09	-0.19	-8.1
2015-06-30	4.0	90.76	26.04	42.3	0.08	0.12	5.2
2014-02-23	5.2	92.51	27.08	55.7[6]	0.07	-0.13	10.7
2014-10-15	3.3	89.87	26.33	35.9[6]	0.07	-0.04	-11.7
2014-07-12	4.5	91.98	26.46	49.4[6]	0.06	-0.08	10.1
2008-05-13	3.5	92.54	27.00	106.1	0.06	0.25	61.2
2014-05-18	4.3	92.91	26.56	43.2[6]	0.06	0.19	1.3
2021-06-17	4.5	92.39	26.68	43.7	0.06	0.09	0.6
2021-04-28	4.4	92.54	26.83	35.0	0.05	-0.20	-8.8
2021-06-18	4.5	92.46	26.74	42.1	0.05	-0.00	-1.3
2020-10-03	4.2	91.31	26.20	44.3	0.03	-0.70	6.4
2014-03-22	3.7	90.43	26.61	32.0[6]	0.02	-0.02	-17.1
2014-08-20	4.1	92.56	27.56	38.3	0.01	-0.30	-9.8
2013-08-21	4.8	92.55	26.68	51.5[6]	0.01	-0.02	8.6
2005-05-29	4.3	92.42	26.93	56.0	0.00	-0.03	11.6
2014-01-11	3.4	90.44	26.59	33.9[6]	-0.01	-0.14	-14.9
2013-11-10	4.0	92.43	26.59	49.7[6]	-0.01	-0.02	7.3
2007-04-11	3.7	92.59	27.52	70.7	-0.02	0.33	22.7
2021-05-06	4.2	92.48	26.59	48.3	-0.03	0.01	5.9
2014-06-27	3.2	90.18	25.72	21.0[6]	-0.04	-0.15	-13.6
2012-10-02	4.5	92.94	26.91	37.8	-0.04	-0.30	-5.9
2013-10-13	4.5	90.29	26.02	31.4[6]	-0.06	-0.33	-6.0
2021-05-18	4.4	92.43	26.67	49.8	-0.06	-0.33	6.8
2021-05-05	4.0	92.10	26.74	47.0	-0.08	-0.22	3.6
2014-05-08	4.2	92.02	25.61	36.4[6]	-0.08	0.17	4.4
2001-04-06	4.4	92.69	26.39	42.7	-0.09	-0.13	8.3
2013-08-10	3.9	92.40	26.62	52.8[6]	-0.10	-0.10	10.1
2008-03-13	4.4	91.94	26.78	38.0	-0.11	-0.19	-5.4
2014-07-16	3.3	91.52	25.85	53.9[6]	-0.12	-0.36	20.4
2009-10-29	4.8	90.02	26.55	30.4	-0.12	-0.16	-19.4
2010-07-06	4.3	92.67	27.68	69.7	-0.13	-0.09	21.1
2015-09-25	4.4	91.69	26.53	48.8	-0.13	-0.04	6.9
2003-03-31	3.9	91.83	26.53	57.7[3]	-0.13	-0.31	15.7
2014-07-20	3.6	91.03	25.62	25.0[6]	-0.14	-0.33	-9.5
2020-09-21	4.4	91.32	26.28	39.6	-0.14	-0.93	0.6
2013-03-08	3.5	90.51	26.32	32.8[6]	-0.15	-0.34	-12.0
2009-08-19	5.2	92.45	26.56	40.0[+]	-0.16	-0.25	-2.2
2014-09-08	3.4	90.85	25.92	41.5[6]	-0.17	-0.39	6.0
2008-11-07	3.9	92.85	25.82	50.8	-0.18	-0.26	18.1
2002-08-20	4.4	92.86	27.29	86.1	-0.19	0.01	39.2
2014-10-09	3.7	90.51	25.78	36.7[6]	-0.20	-0.16	2.1
2013-04-16	3.5	90.89	25.79	46.5[6]	-0.20	-0.13	11.9
2012-08-19	4.0	92.62	26.56	57.0	-0.20	-0.29	15.0
2003-05-30	3.9	92.35	26.80	47.6	-0.21	-0.33	3.9
2013-11-06	5.3	93.74	26.39	35.5[*]	-0.21	-0.23	-6.4
2005-02-27	4.2	91.55	25.37	24.9	-0.22	-0.46	-12.5
2013-12-15	3.5	92.54	26.67	52.4[6]	-0.22	-0.48	9.6
2010-02-24	4.0	93.16	26.06	52.8	-0.23	-0.14	12.3
2013-09-08	4.1	92.05	25.60	24.1[6]	-0.23	-0.48	-8.2
2008-11-14	3.7	92.78	27.75	81.7	-0.23	0.35	32.7
2008-05-10	4.3	92.76	27.62	67.5	-0.24	-0.13	19.0
2013-10-10	3.6	93.24	27.57	44.0[6]	-0.25	-0.51	-4.7
2017-04-18	4.5	91.64	25.06	34.1	-0.25	-0.27	-5.5
2021-04-28	5.0	92.51	26.75	35.0	-0.25	-0.81	-8.4
2021-05-30	4.4	92.33	26.63	52.8	-0.26	-0.41	10.1
2002-07-10	3.8	92.11	26.34	37.4	-0.26	-0.48	0.2
2013-06-03	4.0	89.99	26.19	39.6[6]	-0.28	-0.60	-7.4
2012-03-01	4.6	91.24	27.45	53.6	-0.31	-0.47	6.7
2011-09-18	4.0	91.18	25.76	37.1	-0.31	-0.16	2.6
2015-08-20	3.9	90.26	26.01	43.0	-0.31	-0.82	5.8
2020-02-29	4.2	92.11	26.49	45.4	-0.32	-0.48	6.5
2002-11-14	4.6	92.64	27.55	61.0	-0.33	-0.04	12.8
2014-09-06	3.4	90.41	25.95	30.2[6]	-0.33	-0.23	-6.2
2013-03-02	5.7	92.10	25.25	58.4[6]	-0.33	-0.10	18.2
2013-02-27	4.4	90.75	25.54	24.6[6]	-0.33	-0.71	-9.5
2014-03-13	4.1	92.57	27.48	41.0[6]	-0.35	-0.70	-6.7
2013-07-23	3.2	92.25	26.52	52.7[6]	-0.35	-0.43	10.6
2021-05-31	4.2	92.32	26.76	34.1	-0.35	-0.89	-9.5
2001-06-20	4.3	92.63	26.36	60.5	-0.36	-0.20	26.0
2014-05-29	3.6	90.92	26.00	40.3[6]	-0.37	-0.41	3.7
2004-08-04	4.2	90.26	25.92	61.7	-0.38	-0.14	25.7
2001-08-29	4.3	92.20	27.08	50.1	-0.38	-0.12	5.6
1999-10-09	4.2	91.93	26.40	40.9	-0.38	-0.60	1.9
2014-05-30	4.5	90.35	26.62	31.7[6]	-0.38	-1.22	-17.5
2015-04-16	5.1	92.67	26.84	35.0[+]	-0.39	-0.25	-8.8
2012-05-11	5.4	93.03	26.18	46.1[*]	-0.40	-0.47	5.5
2014-07-17	3.7	90.98	25.77	23.6[6]	-0.42	-0.99	-11.1
2014-12-29	4.0	91.62	26.29	45.0	-0.43	-0.58	6.5
2003-03-25	5.4	89.82	26.92	55.8[*]	-0.44	-0.67	0.9
2013-10-23	4.2	92.94	25.81	32.1[6]	-0.44	-0.57	-0.7
2004-01-12	3.9	91.90	26.36	38.0	-0.45	-0.44	-0.7
2014-07-07	3.5	90.31	25.83	30.1[6]	-0.45	-0.77	-5.1
2021-04-28	4.8	92.48	26.75	38.2	-0.48	-0.86	-5.2
2009-04-25	4.4	91.45	26.11	37.8	-0.49	-0.49	1.7
1999-10-05	5.2	92.02	26.34	38.7[+]	-0.51	-0.63	1.1
2010-07-21	4.5	91.22	27.30	44.5	-0.52	-0.64	0.0
2006-04-11	4.1	92.24	27.27	48.7	-0.52	-0.38	3.8
2013-04-16	5.3	92.13	26.20	36.2[6]	-0.52	-0.61	0.8
2014-09-03	3.7	90.25	25.75	22.3[6]	-0.56	-0.57	-12.4
2005-07-17	4.7	93.39	26.46	31.0[2]	-0.56	-0.79	-10.3
2007-09-18	4.3	91.13	25.24	40.0	-0.56	-0.97	4.1
2014-01-30	3.2	92.15	26.83	33.7[6]	-0.58	-0.84	-10.2
2006-06-19	4.2	90.68	25.53	40.9	-0.60	-0.69	6.9
2021-05-15	4.4	92.47	26.75	43.8	-0.61	-0.82	0.3
2017-09-07	4.1	90.23	25.27	36.7	-0.63	-0.29	2.8
2015-06-28	5.3	90.59	26.38	39.5[*]	-0.63	-0.33	-6.9
2013-05-26	3.6	91.90	26.58	53.7[6]	-0.66	-0.81	11.4
2014-12-04	4.6	92.62	26.89	53.1	-0.67	-1.09	9.0
2014-08-07	3.6	92.10	26.22	41.8[6]	-0.68	-1.02	6.0
2017-02-12	4.4	91.10	25.55	36.9	-0.70	-0.98	2.2
2010-02-16	4.2	92.75	27.60	48.2	-0.71	-1.06	-0.2
2014-07-26	3.2	90.75	25.67	23.0[6]	-0.76	-0.99	-11.2
2013-03-04	4.6	92.42	25.72	41.4[6]	-0.78	-0.84	7.9
2015-07-01	4.5	91.29	27.27	35.5	-0.78	-1.99	-8.2
2003-05-29	4.1	92.77	27.27	76.1	-0.79	-0.39	29.7
2012-10-02	4.9	92.95	26.78	35.5[*]	-0.82	-0.93	-7.5
2017-04-25	4.3	90.88	25.63	31.2	-0.83	-1.00	-3.1
2014-09-12	4.9	90.27	26.04	30.0[6]	-0.83	-1.25	-7.5
2016-05-16	4.3	90.23	25.90	35.1	-0.88	-1.11	-0.7
2013-06-27	3.3	92.57	26.71	51.8[6]	-1.13	-1.47	8.7
2013-10-29	4.3	91.38	27.24	38.2	-1.23	-1.94	-6.5
2014-10-24	5.3	92.93	25.25	49.5[6]	-1.23	-1.26	13.3
2009-11-17	4.7	92.82	27.65	44.4	-1.28	-1.64	-4.6
2008-07-14	4.1	92.02	27.42	61.1	-1.42	-1.50	15.3
2021-04-28	6.0	92.50	26.62	39.8[*]	-1.43	-1.29	-2.8
2006-02-11	4.7	92.14	27.23	49.3	-1.46	-1.43	4.6
2014-09-20	5.1	92.81	25.25	94.6[6]	-1.97	-2.32	58.0

Tangential Waveform

Table SC. Source parameters and waveforms of SET earthquakes, and their ln(Sn/Lg) calculated using RMS and maximum amplitude ratios. Waveforms aligned by P arrival (set to be 60 s here).
Depths listed are from the PDE catalog except where marked with a superscript: 1: Alvizuri and Hetényi, (2019); 2: Craig et al., (2012); 3: Baur, (2007); 4: Parija et al., (2018); 5: Michailos et al., (2021); 6: Diehl et al., (2017); 7: Monsalve et al., (2006); 8: Jiang et al., (2009); 9: Bloch et al., (2021); *: GCMT; +: ISC-GEM.